CARBONATES OF THE YUCATAN PENINSULA

ABIOTIC AND BIOTIC CARBONATES IN KARST FORMATIONS FROM THE YUCATAN PENINSULA; THEIR RECORDS OF PAST AND PRESENT HYDROCHEMISTRY

TEAGAN WARKENTIN, B.A.

A Thesis Submitted to the School of Graduate Studies in Partial Fulfilment of the Requirements for

the Degree Master of Science

McMaster University MASTER OF SCIENCE (2023) Hamilton, Ontario (Earth and Environmental Sciences)

TITLE: Abiotic and biotic carbonate structures in karst formations from the Yucatan peninsula; their records of past and present hydrochemistry. AUTHOR: Teagan Warkentin, B.A. (Ambrose University) SUPERVISOR: Dr. Eduard Reinhardt. NUMBER OF PAGES: 117

This research aims to help our understanding in the role microbialites play in origins of life and biosignatures on exoplanets by looking at element geochemistry and isotopic differences within the structures. This study also examines ability of microbialites to store past and present records of hydrochemistry data.

Abstract

Microbialites are sedimentary structures built by microorganisms through trapping and binding sediment and/or biological-mediated carbonate precipitation. Carbonate structures from four different locations in the Yucatan Peninsula have been documented and analyzed to determine origins and relationships with current and past hydrochemistry. Cenote Fatima had three carbonate structures: two at -13 m depth (CF1A, CF2A) and one at -27 m depth (CF3A) and they were in sheltered light conditions. Two samples were from La Concha (LC1A, LC2A) with a similar depth at -12 m and two more samples were at Hoyo Negro at -18 m (HN1A), and at -45 m (HN2A) which were in dark conditions. Samples from Xul Ha (XH1A and XH2A) next to Laguna Bacalar which has some of the largest freshwater microbialite formations in the world and both these locations were in full light conditions. S/Ca ratios in Xul Ha samples show a hydrogeochemical origin linked to the dissolution of gypsum from underground karst. Xul Ha had the highest recorded S and Sr levels and our results match previous geochemical research on stromatolites and thrombolites. Samples from Cenote Fatima had radiocarbon ages that matched past water levels that have been recorded in Hoyo Negro and Hells Bells showing a drop in $\delta^{13}C$ of ≈3.5‰ between ≈7600 – ≈9000 cal. yr. BP. Cenote Fatima also shows a narrow growth window in the sunlit upper water column (3-4m) indicating a biogenically influenced origin. Hoyo Negro samples were shown to match the geochemistry of Holocene aquifer based on calcite raft core records and were deemed to be more abiotic based on prior research on Hells Bells in Cenote Zapote. Based on radiocarbon ages they thought to have formed during Stage 5e (125,000 yr. BP).

Acknowledgments

I would like to thank my supervisor Dr. Eduard Reinhardt for teaching me new techniques in research and assisting me as I learned a brand-new area of science. I would like to thank him for his patience and understanding regarding my variety of health conditions and allowing me to work at my own pace. I would like to thank Martin Knyf for teaching me about the isotope mass spectrometer and allowing me to have a hands-on experience with stable isotope research. I would like to thank David and Betty Freeman for providing me a place to stay while I started my Master's program. I would like to thank my parents for their support and driving me all the way to Ontario from Alberta, Canada.

Table of Contents

List of Figures

List of Abbreviations

i) HN: Hoyo Negro
ii) XH: Xul Ha
iii) LC: La Concha
iv) CF: Cenote Fatima
v) BIM: Biologically Induced Mineralization
vi) BCM: Biologically Controlled Mineralization
vii) MeWM: Meteoric Water Mass
viii) MaWM: Marine Water Mass
ix) MxWM: Mixing Water Mass
x) 1σ: Standard Deviation

Chapter 1

Geology and Hydrochemistry of Sample Locations

Geology of the Yucatan

Yucatán Peninsula is a karstified carbonate platform composed of limestone, dolostone, and anhydrite dating to the Tertiary to Quaternary periods (Perry et al., 2002; Vázquez-Domínguez & Arita, 2010; Ward et al., 1985). This large platform is 350,000km^2 and goes beyond Mexico's borders into Belize and Guatemala (Ward W.C. et al., 1985). Cretaceous rocks underlie the platform with the Chicxulub impact crater located in the north of the peninsula. The sedimentary rocks are marine in origin (Tertiary limestone and dolostone); and there are no terrigenous clast rocks (Perry et al., 2009). The limestone is heavily karstified with numerous cave systems and cenotes (sinkholes; Ward et al., 1985). This limestone contains the primary aquifer for the peninsula (Perry et al., 2002).

1.1 Hydrogeochemical Regions in the Yucatan.

The Yucatan Peninsula is made up of 6 regions differing in hydrogeochemistry as defined by Perry et al. (2002; Figure 1):

1) Chicxulub Sedimentary Basin. This area is to the north and is where the Cretaceous Chicxulub impact crater is located which was identified by magnetic maps, shocked quartz, and gravity maps data defining the extent of the impact crater (Hildebrand et al., 1991).

2) Cenote Ring. A semicircular ring that separates the Chicxulub Sedimentary Basin from the Holbox Fracture Zone and is outlined in sinkholes that date to the Tertiary (Paleogene to Neogene) and is an area with very high permeability (Steinich & Marín, 1997; Perry et al., 2002). Due to large influx of freshwater coming from inland areas, there is mixing with the underlying

marine water. It is unlikely that the impact created the ring of cenotes as it was most likely caused by tectonic action (Hildebrand et al., 1991; Perry et al., 1995).

3) Pockmarked Terrain. Underlying the Tertiary rock units in the Tical Fault Zone, gypsum anhydride and evaporite rocks have been exposed to karstification (Perry et al., 2002). Many cenotes are present in the limestone caused by dissolution of $CaSO_4$ in the Tertiary evaporites (anhydrites, gypsums; Perry et al., 2002). This area has the highest topography of the Yucatan.

4)Tical Fault Zone. Tertiary rock units are thrust to the south and this zone is made of gypsum, anhydrite, and evaporites and impact breccia (Perry et al., 1995). The fault line transports SO_4 from the area of Lake Chichancanab to the Ring of Cenotes (Perry et al., 2009 and references therein). Poljes or bajos are flat floored basins which are due to underground erosion leading to depressions (Perry et al., 2009).

5) Holbox Fracture Zone-Xel Ha Zone. This area has elongated cenotes linked together making a network that is 100km long called sabanas (Perry et al., 2002). These are common in this region as they run along the fault line which may have formed by tectonic activity in the Eocene. Cenote Fatima, Hoyo Negro, and La Concha are all located in this region (Perry et al., 2002). Intrusions from the coast brings marine water (Marine Water Mass-MaWM) which penetrates landward (Perry et al., 2002).

6) Evaporite Region. This area has low permeability compared to the other geochemical regions so streams and lagoons form as the Meteoritic Water Mass (MeWM) flows in the upper karst (Perry et al., 2002). Very high sulfate values are found here and Perry et al. (2002) found that water moves south and westward from Lake Chichancanab region creating a boundary from the

Evaporite Region and the Holbox Fracture Zone. Rocks are Eocene to Miocene/Pliocene in age (Perry et al., 2002).

1.2 Cave and Cenote Formations

Currently, the Yucatan contains 1700 km of explored underwater passages and 360 km of dry cave passages (QRSS, 2023). These cave systems often run parallel to the ground surface and most are shallow ranging from ≈5 m to ≈25 m in depth but there are also deep cenotes that can be greater than 45 m (QRSS, 2023). Most cave systems explored in the Holbox Fracture Zone between Tulum and Cancun run perpendicular to the coast. The underground cave systems are unlike continental caves, which are more clustered in specific locations (Smart et al., 2006). The cave systems in Quintana Roo appear to be highly interconnected and anastomosing having one or more openings (cenotes) to the surface (Smart et al., 2006). Two types of passages exist in the Yucatan, fissure openings which are usually very narrow almost facture-like in appearance which are most common along the coast, and elliptical tubular passages which are wider than they are tall (Smart et al., 2006). Breakdowns or collapses of the cave ceiling can cause square-shaped passages (Smart et al., 2006). Many passages are a mix between the two and have notches caused by a pH drop from the mixing of the MeWM and MaWM. The position and width of the mixing zone (MxWM) determines the elevation and extent of carbonate dissolution (Smart et al., 2006). Sea level changes can determine can also change the level of the mixing zone/halocline and thus the elevation and dissolution within the limestone. Cenotes are collapsed sink holes filled with water and are openings to the underground cave passages which are a major karst features in the Yucatan (Ward et al., 1985; van Hengstum et al., 2008). These openings can be 30-60 m in diameter and larger cenotes known as hoyas can be 60-100 m in

diameter(Ward et al., 1985 and references therein). Cenotes that are not connected to an underground passageway are referred to as pit cenotes. Precipitation and overland flow, evaporation, and the dissolution $CaCO_3$ by biogenic processes all contribute to the formation of cenotes (Smart et al., 2006).

Warmer climate and high permeability promote karstification (Ward et al., 1985) and carbonate sedimentation, sea level transgression/regression, and collapse attribute to the formation of cave systems (Smart et al., 2006). The influx of organic material also contributes to cave formation as oxidation forms acids and causes dissolution (Smart et al., 2006).

1.3 Aquifer Hydrology

The karst of the Yucatan is highly permeable and allows the MaWM from the ocean to infiltrate as far as 100 km inland (Perry et al., 2002; Figure 2). Rainfall rates in the Yucatan are ≈1500 mm/year where 80% falls between May to September which infiltrates porous limestone creating the MeWM (Ward et al., 1985; Smart et al., 2006; van Hengstum et al., 2010; Gonneea et al., 2014;). Most of the rainfall is penetrates quickly through the high porosity limestone so there are few lakes or rivers in the Yucatan (Ward W.C et al., 1985; Collins, et al., 2015b and references therein).

The MeWM is less dense than the MaWM and is positioned on top (Figure 2). When more or less mixing occurs between the water masses a MxWM (Mixed Water Mass) of variable thickness may form or it could be a sharp transition occurs (halocline). A rise in sea level causes the MaWM to penetrate further inland and causes the MeWM to rise (Beddows, 2004).

Kirkland in 1980 found that bacteria often form structures in the mixing zone or at the halocline (Beddows, 2004 and references therein).

Groundwater flow through the cave systems is 1-10km/day and tidal oscillations are found at a great distance inland (Beddows, 2004; van Hengstum et al., 2008; Coutino et al., 2020). Tidal oscillations, rainfall, and tropical storms all affect the mixing zone leading to changes in salinity in the aquifer (Coutino et al., 2017; Kovacs et al., 2017; 2018).

Groundwater levels during the Holocene have been dictated by sea-level rise. This relationship has been independently determined by dating the presence of aquatic sediments in the cave system (Collins et al., 2015a; Collins et. al., 2015b; Kovacs et.al., 2017; Krywy-Janzen et. al., 2019; Steele et. al., 2023).

Chapter 2

Microbialites

2.1 Microbialites Structures

Microbially induced carbonate precipitation or MICP can cause organosedimentary structures to be formed in bodies of fresh or marine water by benthic microbes, detrital grains and hydrochemistry (Burne & Moore, 1987). Microbialites are often formed by microorganisms usually cyanobacteria; these formations come in three main groups: stromatolites have laminations in their structures, thrombolites have ambiguous branched structures, and leiolites have no internal structures present (Fowler, 2011). Microbialites have been seen in many environments including marine environments such as Shark Bay, Australia (Logan, 1961), hypersaline lakes such as Storr Lake in the Bahamas (Fowler, 2011; Mann & Nelson, 1989 and references therein; Paul et al., 2016), and freshwater bodies such as the microbialites in Pavilion Lake (Omelon et al., 2013; Brady et al., 2014, 2010) and Laguna Bacalar (Gischler et al., 2008; Castro-Contreras et al., 2014).

Stromatolites can be 3.7-billion-years-old formations making them the oldest biosignatures of life on Earth (Nutman et al., 2016) . The layering in stromatolites can either be composed of uneven layers or thin linear deposits that are observed throughout the structure (Fowler, 2011). The distinct layering could be due to wetting and drying in the intertidal zones of costal environments (Aitken, 1967). Stromatolite formation can be caused by either the trapping of sediment or carbonate precipitation or both (Aitken, 1967; Burne & Moore, 1987). EPS (Extracellular Polymeric Substances) acts like a glue or cement holding the grains and particles together; Reid et al. (2000) found that certain microbial mats can capture tunicate spicules on the EPS films. In quieter areas with less waves or current action there is less trapping of

sediment and carbonate precipitation can dominate (Fowler, 2011). Laminations can be linked to biological activity (Reid et al., 2000).

Thrombolites often have fewer straight laminations and are more bulbous and branched out in structure and often have a rough, outer texture (Aitken, 1967; Ferris et al., 1997). Thrombolite formation is not well understood but Fowler, 2011 postulated that the rising of sea level caused a change from stromatolite formation to a more branched opaque thrombolytic structure. Rapid calcification or algae growth could cause these thrombolite formations.

2.2 Early History of Microbialites

Microbialites are often studied as they able to retain their original structure and often original geochemical composition dating back 3.4–3.7 billion years old (Breitbart et al., 2009 and references therein; Dodd et al., 2017; Cavalazzi et al., 2021,). These structures contain information on their biological properties and processes as well as environmental conditions. Some of the earliest microbialites were found in Isua Greenstone Belt, Greenland and date to 3.7Ga (Dodd et al., 2017; Nutman et al., 2016) and microbialites in Pilbara Craton, Australia were dated at 3.5Ga (Johnson et al., 2018 and references therein). Thrombolytic formations became more prevalent late in earth history as preexisting stromatolites and changed to thrombolytic growth possibly due to changes in the environment (Walter and Heys, 1985). Microbes (cyanobacteria) could have played a large role in the oxidation of Earth's atmosphere and evidence to support is found in microbialite formations (Des Marais, 1997 and references therein; Lyons et al., 2014).

2.3 Biota of Microbial Structures

Microbial mats are shown to have a variety of microorganisms such as cyanobacteria, sulfate reducing bacteria, heterotrophs, and even algae (Breitbart et al., 2009 and references therein). Cyanobacteria are very important in the creation of microbialites as they are very common, are primary producers leading to other food chains, and photosynthetic reactions can create changes in pH promoting calcium carbonate precipitation (as reviewed in Dupraz et al., 2009).

In microbial mats, there are often layers (laminations) based on the types of metabolism each microbe exhibits. Oxygenic metabolism is usually the first layer, then the nitrogen fixers, next iron and manganese reduction, then sulfate reduction, and methanogens are on the bottom or the deepest part of the mat. Six most common microbialite metabolite groups are: aerobic photoautotrophs (ex. Cyanobacteria), aerobic heterotrophs (oxidize organic matter), anerobic phototrophs (ex. purple and green bacteria), anerobic heterotrophs (sulfate reducing bacteria), and sulfide oxidizing bacteria (Breitbart et al., 2009 and references therein; Dupraz et al., 2009; Paul et al., 2016).

Ferris et al. 1997 found *Calothrix* and *Fischerella* in stromatolite samples in Kelly Lake. Looking at the differences between thrombolites and stromatolites, thrombolites had the genus (*Gloeocapsa* and *Synechococcu*) as the most common (Ferris et al., 1997). Yanez-Montalvo et al. (2021) found a large abundance in Cenote Azul showing a major difference in phyla that varied with depth (*Brocadiacae*, *Rokubacteria*, *Proteobacteria* and *Planctomycetes*) (Yanez-Montalvo et al., 2021). Paul et al. (2016) studying Storr Lake found sulfur reducing bacteria in the class of

Deltaproteobacteria as all as other taxa including: *Spirochaetes*, *Planctomycetes*, *Alphaproteobacteria*, *Gammaproteobacteria*, *Bacteroidetes*, and *Caldithrix*.

2.4 Biomineralization Processes

Biomineralization is a process in which living organisms (invertebrates, microorganisms, plants, etc.) are able to produce minerals (Joshi & Baskar, 2022). This can happen in three ways: 1) trapping and binding of loose grains, 2) cells providing a nucleation site for minerals to grow, or 3) metabolic activity causing calcification and carbonates to form (Burne & Moore, 1987; Dupraz et al., 2009; Ferris et al., 1997; Schultze-Lam et al., 1996). These minerals are able to be distinguished from abiotic formations through detailed examinations (thin sections, SEM, etc.). BIM (Biologically Induced Mineralization) which often occurs on the EPS as it captures Ca^{2+} on the surface of the cell (Joshi & Baskar, 2022 and references therein). BCM (Biologically Controlled Mineralization) and minerals can be produced in the cell or on the cell in a controlled way and is unlike BIM as BIM uses metabolism to promote biomineralization; BCM is the mechanism that forms bones, shells, teeth, etc. (Joshi & Baskar, 2022). Bacteria induce calcium carbonate precipitation in the environment via passive or active pathways, temperature, pH, nucleation sites and substrate concentration all affect biomineralization (Joshi & Baskar 2022). Calcium carbonate comes in three forms: calcite, aragonite, and vaterite where calcite is the most stable form (Ercole et al., 2001).

Henry's Law determines the solubility of a gas such as CO_2 in water and is temperature/climate dependant (Schmitz, 2017). CO_2 becomes an acid with the equation: $CO_{2(aq)} + H_2O_{(l)} \leftrightarrow H_2CO_3$ (James and Jones, 2016, pg. 16). This is a weak acid and can dissociate into

bicarbonate: $H_2CO_3 \leftrightarrow HCO_3^- + H^+$ (James and Jones, 2016, pg. 16). The bicarbonate ion can further dissociate into $HCO_3^- \leftrightarrow CO_3^{2-} + H^+$ (James and Jones, 2016, pg. 16). The pH is what controls the equilibrium of these reactions and which products or reactants will be more common. The dissolved CO_2 is what controls the pH. The equilibrium constant or what determines which way the reactions will go (dissociation or combination of the ions) is also dependant on temperature (James and Jones, 2016 pg. 17).

In passive carbonate precipitation, the necessary ingredients (bicarbonate ion, carbonate and calcium ion) are created through metabolic pathways (Castanier et al., 1999). Two pathways nitrogen and sulfur can produce carbonate/bicarbonate ions. When pH increases (H^+ decreases) then CO_3^{2-} carbonate is more likely to form and combine with the Ca^{2+} instead of a hydrogen ion which would create a bicarbonate HCO_3^- (Castanier et al., 1999). The most common form when the pH is high is bicarbonate HCO_3^- as CO_2 gets dissolved into the water. Carbonic anhydrase can create CO_2 and OH^- during photosynthesis (Brady et al., 2010). The OH^- causes a higher pH near the cell and carbonate CO_3^{2-} can bind to calcium leading carbonate precipitation (Brady et al., 2010; Castanier et al., 1999). Decreases in partial CO_2 pressure, turbulence of water, increase in temperature or decrease in water pressure can be abiotic mechanisms as to which calcium carbonate can precipitate (Ercole et al., 2001).

Heterotrophs and autotrophs can be influences in calcium precipitation (methanogenesis, oxygenic and anoxygenic photosynthesis, nitrogen fixation, SRB, etc.). Sulfur reducing bacteria are heterotrophs and have been shown to induce calcium carbonate precipitation (Visscher et al., 2000). In degassing of hydrogen sulfide (HS), there is a pH increase

and increase precipitation of calcium carbonate (Castanier et al., 1999). In the nitrogen pathway ammonia can be produced thus increasing the pH (Castanier et al., 1999).

The extracellular polymeric substances (EPS) made by cyanobacteria (autotrophs) can serve as a nucleation site promoting calcium carbonate precipitation. Extracellular polymeric substances have been shown to have chemical gradients allowing Ca^{2+} ions to be attracted to the negative ions (phosphates) preventing calcium carbonate precipitation (as reviewed in by Dupraz et al., 2009). However, degradation of the EPS by enzymes (hydrolases, lyases, glycosidases, etc.) by microbes such as SRB can increase precipitation by releasing all the attached Ca^{2+} (as reviewed by Dupraz et al., 2009, Visscher et al., 2000).

In active process, the cell actively produces the carbonate ion through ionic channels that move Ca^{2+} or Mg^{2+} in and out of the cell (Castanier et al., 1999). Sometimes the calcium carbonate is produced on the cell membrane until it becomes a cocoon or it is produced inside the cell and is excreted out wards; both of theses are examples BCM (Castanier et al., 1999).

Many isolates from speleothem formations have helped biomineralize calcium carbonate. Bacteria isolated from Stiffes Cave in Italy were shown to produce calcite; most were from the Bacillus and Arthrobacter genus (Ercole et al., 2001). Ruszynak et al. (2012) used confocal laser scanning microscopy to determine the presence of Ca^{2+} that were attached to the bacteria cell wall proving that bacteria cells can serve as a nucleation point and this could be due to the mycolic acids, phosphates, or other negatively charged molecules present in the bacterial cell wall. When knocking out a gene called chaA which transports Ca^{2+} and H^{+} in and out of the cell Banks et al. (2010) noticed the microbes did not grow as well as the wild type;

they did not grow on the calcium medium and were unable to clear the mineral leading to the fact that cells are metabolically active during calcification process. It was discovered that using carbon isotopes that the CO_2 in the atmosphere was in fact being incorporated into the minerals that made up the speleothem (Banks et al., 2010).

In Highborne Cay Bahamas, the cyanobacteria used metabolic pathways such as photosynthesis, sulfate reduction, anerobic sulfur oxidation which promoted calcite precipitation and aerobic pathways (aerobic respiration, aerobic sulfur oxidation) promoted calcite dissolution (Visscher et al., 1998). When combined photosynthesis and aerobic respiration did not net in any calcite formed but when combined with sulfur metabolism it create calcite (Visscher et al., 1998).

2.5 Biosignatures

Biosignatures can be fossils of microbial cells, isotopic fractionation, organic compounds made specifically by life processes, and sediment traces such as boring, or depressions (Cady et al., 2003). Biological mechanisms are trapping and binding, EPS, and metabolism. A good way to determine if microbes are responsible for trapping and binding is to either view the microbes encrusted in the material or show that the structures or textures are consistent with a microbe making them (Jones, 2001).

Microbial fossils are difficult to detect on Earth so other biosignatures such as elemental traces or isotopic fractionation must be used as Tice et al., (2017) did when studying microbialites from the Mesoarchean area around 2.98Ga. Carbon has three main isotopes ^{12}C, ^{13}C, and ^{14}C two of which are stable ^{12}C and ^{13}C and the ^{12}C is the most abundant (James and

Jones, 2016 pg. 304). Due to thermodynamic and kinetic effects biological organisms use ^{12}C because it is a lighter isotope (O'Leary, 1988). In the Carbon Cycle the rubisco enzyme will prefer ^{12}C instead of ^{13}C during carbon fixation of CO_2 (O'Leary, 1988). This can leave behind the ^{13}C in the carbonate leading it to become enriched. The biological material has more $\delta^{12}C$ and less $\delta^{13}C$ leading to a negative $\delta^{13}C$ value and the reservoir will have more $\delta^{13}C$ and less $\delta^{12}C$ leading to a more positive $\delta^{13}C$ value (Burne & Moore, 1987). $\delta^{18}O$ is useful in determining the water input/output of a cenote as low output or evaporation the $\delta^{18}O$ will reflect the same as precipitation and groundwater (it will be low) and in high evaporation the $\delta^{18}O$ will vary and be higher(Gilli et al., 2009).

Certain elemental signatures can be determined using ICP-MS or XRF. Tice et al. (2017) used μXRF to determine rock types and biosignatures of the Mesoarchean Nsuze Group which contains 2.98Ga stromatolite formations in South Africa. They found that the XRF was able to determine sedimentary features and layering that is not present visually in the sample. Valdespino-Castillo et al., (2018) looked at microbialites present in Mexico and Cuba using XRF showing that the most dominant microbes showed correlation with trace elements. Using ICP-MS analysis of microbialites from Laguna Bacalar, Castro-Contreras et al. (2014) found that stromatolites had more enriched concentrations (Mg, Fe, Si etc.) and this is thought to be due to cyanobacteria. Differences in elemental geochemistry between thrombolites and stromatolites could be due to cyanobacteria abundance and growth and these differences can be preserved in the microbialites (Castro-Contreras et al., 2014).

In the Yucatan recognizing biosignatures is often difficult because of the environmental setting. Prior research (Kovacs et al., 2017; Collins et al., 2015a, Collins et al., 2015b) shows that

there were large changes in ground water level and aquifer changes in the Holocene which presents challenges with relating current water conditions with geochemical composition of the microbialites. This is especially relevant when it is not known whether the microbialites are currently actively accreting. Cenotes and caves contain an abundance of speleothem formations during Quaternary Sea level changes and the carbonate structures have high preservation potential. As Kovacs et al. (2017) has demonstrated the rises and falls of groundwater during the Holocene is associated with large changes in the aquifer hydrogeochemistry. These site characteristics are unlike previously studied freshwater microbialites in Pavilion Lake in British Columbia, Canada (Brady et al., 2014; 2010; Omelon et al., 2013) which would have had relatively stable/static conditions throughout the Holocene. Here we present isotopic and geochemical evidence from microbialites or potential microbialites in three locations 1) Xul Ha, 2) Cenote Fatima, and 3) Hoyo Negro/La Concha in an attempt to understand their origin with comparisons to paleohydrological data and dating evidence (Kovacs et al., 2017; Schnordorf et. al., n.d.).

Chapter 3

Previous Work Done in the Yucatan

3.1 Laguna Bacalar and Xul Ha Cenote

Gischler et al. (2008) studied the freshwater microbialites of Laguna Bacalar which is regarded as one of the largest freshwater sites where they are actively growing. Microbialites/microbial mats consisting of domal or pillow-shaped growths up to 2 m in diameter and height and the bioherm was found to be 40 km in length (Gischler et al., 2008). Microbial mats are found on top of the outer surface of the structure and are tough and leathery and are orange to green to reddish brown in color and likely represents different bacteria with different seasonal growth periods (Gischler et al., 2011; Gischler et al. 2008). The most abundant mats are formed by cyanobacteria *Calothrix* which create a brownish leathery mat; dark green or blackish dome-shaped mats are caused by *Scytonema*; bright orange-colored mats are caused by *Leptolyngbya* and these are near the surface (Gischler et al., 2011). Carotenoids protect the photosynthetic bacteria which make a blue-green layer underneath the orange layer (Gischler et al., 2011). On the western side of Bacalar, microbialite samples were radiometrically (^{14}C) dated to 8-5 cal. kyr. BP and on the eastern side the microbialites are younger ranging from of 6-3 to 7-0 cal. kyr. BP (Gischler et al., 2008). Carbonate sediment from the bottom of the lagoon is the same age of as the western lagoon microbialites. Shells from two living molluscs found in the western area were dated from 7-8 cal. kyr. BP and 7-3 cal. kyr. BP suggesting a large hardwater offset in the radiocarbon ages, and the microbialites formed in the late Holocene and not early Holocene (Gischler et al., 2008). The ^{14}C deficient carbon suggests the karst aquifer that leads into the lagoon contains a lot of 'dead' carbon. Gastropod and articulated bivalve shells are also abundant in the microbialites which are not common in marine microbialite samples (Gischler et al., 2008).

The Laguna Bacalar microbialites show evidence of active growth and that bacteria were playing an active role in the formation in the organosedimentary structures. Castro-Contreras et al. (2014) reported finding calcified cyanobacteria filaments in Laguna Bacalar. The Bacalar samples support trapping and binding with active carbonate precipitation to form the microbialite structures. There seems to be a higher diversity of bacteria to the north of the lagoon in Laguna Bacalar and higher organic compounds with high amounts of carbon which is in an elemental signature of growth (Águila et al., 2022; Valdespino-Castillo et al., 2018). *Homeothrix* and *Leptolyngbya* cyanobacteria play a role in calcium carbonate precipitation through intake of CO_2 via photosynthesis, the creation of extracellular polymeric substances (EPS), and biofilms that trap ions in freshwater oversaturated with carbonate ions (Gischler et al., 2008). Calcium crystals in the microbialites were 50 micrometers long; and the sediment on the bottom of the lagoon is the same as the sediment found in the microbialites suggesting binding of detrital sediment (Gischler et al., 2008). Valdespino-Castillo et al. (2018) also determined that the presence of K^+, Ca^{2+} and Na^+ ions in the water accounted for the accumulation of the same elements in the microbialites. Microbialites seem to be able to store information of the surrounding aquatic environment.

In Cenote Azul, a 90 m sinkhole 100 m away from Laguna Bacalar has at least 20-30 m of microbial mats but it is unclear if they are actively growing (Águila et al., 2022). Águila et al. (2022) examined the bacteria diversity of the cenote and they found 44 taxa of cyanobacteria and 15 new species, 32 were also found in Laguna Bacalar and 31 were exclusive to Cenote Azul. Johnson et al. (2018) did bacteria diversity in Laguna Bacalar and found that *Proteobacteria* was the dominant genus and some others were the classes *Alphaproteobacteria*,

Gammaproteobacteria, and *Deltaproteobacteria*. Light availability and depth as well geologic location seemed to play a role in the diversity of the cyanobacteria as Laguna Bacalar seemed to have preference for *Nostocales* and in Cenote Azul *Chroococcales* was more dominant (Águila et al., 2022).

3.2 Hells Bells in Cenote El Zapote

The microbialites in Cenote El Zapote are locally referred to as Hells Bells and were studied by López-Martínez et al. (2020); Ritter et al. (2019); Schorndorf et al. (n.d.); and Stinnesbeck et al. (2018). Cenote El Zapote is in close proximity to Cenote Fatima ≈4 km NE. Hells Bells are unusual formations and they are large conical structures up to 2 m long with a trumpet or bell like shape that extends downwards and expands outwards (Stinnesbeck et al., 2018; Ritter et al., 2019). They are located at 29-35 m depth which is slightly above the halocline and in the sulfidic anoxic zone which has minimal light (Stinnesbeck et al., 2018; Ritter et al., 2019). Hells Bells formed in aquatic conditions and are the largest underwater forming "speleothems" found thus far (Ritter et al., 2019). Stinnesbeck et al. (2018) showed that there were more bacteria on the speleothems then in the current water column. The most common bacteria on the formations were *Proteobacteria* (25%), *Nitrospirae* (21%), *Chlorobi* (19%) and *Chloroflexi* (18%) (Stinnesbeck et al., 2018). Autotrophy and denitrification are major factors that contribute to the biomineralization of Hells Bells formations (Stinnesbeck et al., 2018). Sulfide oxidation and other forms of chemolithotrophy caused an increase in alkalinity which promoted calcium carbonate precipitation as there was less hydrogen ions to bind with the carbonate (Ritter et al., 2019). Mg/Ca ratios in Ritter et al. 2019 showed that the Hells Bells likely formed in the redoxcline as the Mg/Ca values found in the Hells Bells carbonate are the

same as the water where the redoxcline is located (36-37m). The redoxcline is oversaturated with calcium and carbonate ions; there is also an abundance of other elements including S and N which could be metabolized by the microbes on the Hells Bells (Ritter et al., 2019). The Hells Bells grow downwards and towards the center due to the cenote topography and start to spread out (in a bell shape) near the end of the redoxcline (Ritter et al., 2019). Ritter et al. 2019 stated a predicted growth rate of 27-146 a^{-1} μm^{-2} which is within the range of Stinnesbeck et al., (2017) which had a growth rate of 12-90 a^{-1} μm^{-2}. Stinnesbeck et al. (2018) and Ritter et al. (2019) determined that the halocline has a large role in the growth of the Hells Bells. Raising the halocline during drought or lowering it during storms or wet periods influences oxygenation of the halocline promoting aerobic sulfide metabolism of bacteria leading to more acidic conditions which prevents growth as the acid causes dissolution of the rocks. Microbial mediation also plays a role in the shape of the formations as autotrophy and denitrification can cause EPS with negatively charged ions attracting positively charged ions Ca^{2+} incorporating the calcium into the structure (Ritter et al., 2019; Stinnesbeck et al., 2018). However, Ritter et al. (2019) argues that inorganic calcite precipitation influences the Hells Bells formation based on euhedral calcite crystals growth which is slower than anhedral crystal growth which is caused by a faster process. Both processes contribute to the growth of the Hells Bells but it is not known how much microbes contribute to calcite growth and the shape of the structures.

Hells Bells could also be formed underwater by CO_2 degassing (López-Martínez et al., 2020). Degassing of CO_2 underwater can provide calcite precipitation for the formation of the Hells Bells (López-Martínez et al., 2020). López-Martínez et al. (2020) proposes that dissolved CO_2 bubbles get trapped in the irregularities of the cenote rock wall leading to CO_2 degassing

and ultimately calcite precipitation on the surface of the bubble. Schorndorf et al. n.d. dated (U-series) the Hells Bells to be forming the past 9600 yrs. BP indicating they have formed underwater based on Holocene sea level.

3.3 Hoyo Negro

Hoyo Negro is a 45 m deep pit connected to the San Actun Cave system and has been studied extensively due to the extinct mega fauna fossils found at the bottom of the pit. (Chatters et al., 2014; Kovacs et al., 2017). The remains of an early Holocene (Pleistocene) human skeleton named Naia was also found with the mega fauna (Chatters et al., 2014). Kovacs et al. (2017) provided paleoenvironmental information on aquifer conditions. Collins et al. (2015a) reconstructed the water level and flooding history of Hoyo Negro using sediment cores and evidence of aquatic sediment deposits. Collins et al. 2015a discovered that there was water at the bottom of the pit at (36-48 m) at 9850 cal. yrs. BP and the cave passages that led to Hoyo Negro (-12 m) were flooded between 6000 and 8100 cal. yrs. BP. Kovacs et al. (2017) studied submerged calcite rafts accumulations at the bottom of Hoyo Negro and Cenote Ich Balam. Calcite rafts form at the air/water interface through CO_2 off gassing and gain in mass which then sink to the bottom forming mounds (Kovacs et al., 2017). Kovacs et al. (2017) used calcite raft records of Cl/Ca, Sr/Ca, $^{87}Sr/^{86}Sr$, $\delta^{13}C$, and $\delta^{18}O$ in the rafts spanning 0-8.3Ka BP to provide changes in aquifer history and relationships between the Holocene climate and hydrogeology. The calcite rafts showed between ≈7.8-8.3 Ka yrs. BP the MeWM was slightly more saline 1.5-2.7 ppt likely because of increased rainfall and flow causing mixing with the MaWM. From ≈0-7 cal. Ka yrs. BP the MeWM became increasing fresher (1.0-1.5 ppt) and less saline with increased aridity. This matched independently derived records of rainfall spanning the Holocene (Kovacs

et. al., 2017). The calcite raft records showed a large drop in $\delta^{13}C$ and Sr/Ca between ≈7.8-8.3 Ka cal. yrs. and ≈0-7 Ka cal. yrs. In 2021 a wall of mound-like precipitates/bioherm 3 m wide thought to be microbialites were found circling the wall at -18 m and slightly above the halocline similar to the formations found in Cenote El Zapote. However, the formations in Hoyo Negro lacked a bell-shaped morphology.

Chapter 4.

Methodology

4.1 Locations

4.1.1 Xul Ha Cenote

Laguna Bacalar is surrounded by Cenozoic limestone (Gischler et al., 2008) and dolomite (Johnson et al., 2018) and contains four cenotes which are Brujas, Esmeralda, Cocolitas and Xul Ha where XH1A and XH2A were sampled (Yanez-Montalvo et al., 2021). Local fisherman claim that Xul Ha is as deep as 90 m (Gischler et al., 2008). Xul Ha has a temperature of 25.2 °C, pH of 6.3, conductivity of 2.24 mS/cm and a salinity of 1.15 ppt. To the north of the cenote is a that is 15 m canal that links the cenote to Laguna Bacalar (Gischler et al., 2008). Along the canal is a small embankment where large microbialite structures are found (Figure 3). The alcove opens into a mangrove area and the depth is about 6 m and is where XH2 was sampled. The temperature is 26.3 °C, the pH is 6.2, conductivity is 2.85 mS/cm, and salinity is 1.16 ppt. Laguna Bacalar has high concentrations of sulfate, strontium, and calcium (Gischer et al., 2008; Castro-Contreras et al., 2014; Johnson et al., 2018).

4.1.2 Cenote Fatima

Cenote Fatima is located near Puerto Morelos Quintana Roo and is 22 km away from the coast (Figure 3) and is ≈4 km SW of Cenote El Zapote. The cenote has not been completely mapped, so overall characteristics are based on diver collected data and observations. Cenote Fatima is a pit cenote with a typical hourglass morphology and a surficial diameter of 25 m (Figure 4). As yet, it is not known if cave passages connect with the cenote. There is a large break down pile in the center of the cenote which has many dead trees and branches which also contains abundant organic-rich sediment (Figure 4). Samples CF1A and CF2A were collected

on an alcove on the cenote wall at -13 m (Figure 4). The cobble-sized samples were laying in muddy sediment with growth lobes oriented towards the light and the microbialites were not attached to the bottom. CF3A was collected at the base of the cenote wall at -27 m above the halocline which is a depth of -35 m (Figure 4). CF3A was bush-like in shape and attached to the bottom and the branches pointed upwards and one branch was removed for analysis.

4.1.3 Hoyo Negro

Hoyo Negro is a large deep underwater pit ≈45 m deep and is bell shaped with a diameter of 32 m at the top and 60 m near the bottom (Chatters et al., 2014). There are three nearby cenotes (Ich Balam, La Concha, and Oasis) with passages that connect to Hoyo Negro (Collins, et al., 2015a). Hoyo Negro is 7km inland (Figure 5) and the halocline is ≈-18 m (Kovacs et al., 2017). Samples were collected by divers with hammer and chisel and HN1A was collected at -18 m on the pit wall very close to the current halocline (Figure 5). A ring of carbonates that form a ≈3 m wide ring were found along the circumference of the pit from -17 m to -20 m. HN2A was a speleothem that formed on the breakdown pile at the bottom of the pit and was a subsample at the top of a stalagmite (-45 m).

4.2 Water Profiles

Water mass profiles were measured with two types of sondes. Hoyo Negro used a Hydrolab MS5 mini-sonde and Cenote Fatima used YSI-EXO1 multi-parameter sonde. The sondes were slowly lowered through the water column using divers measuring temperature (°C), depth (m), salinity (psu), dissolved oxygen (DO; % concentration), and pH. Laguna Bacalar had water data recorded previous studies (Gischler et al., 2008; Castro-Contreras et al., 2014)

4.3.1 Sample Preparation

Samples were air dried and sectioned with a lapidary saw. Samples were rinsed with di-ionized water and were briefly washed in an ultrasonic bath (50T AquaSonic) to remove any contamination from the sawing process. Samples were cut into multiple rectangular pieces (3cm×1cm) that were oriented perpendicular to apparent growth and these sections were used for drilling for geochemistry and thin sections.

4.3.2 Thin Sections and XRD

Thin sections were performed by Vancouver Petrographic (Vancouver, British Columbia). Approximately, 2-3 mg was drilled for XRD which was conducted at McMaster University at the Analytical X-Ray Diffraction Facility (Max).

4.4 Geochemistry

4.4.1 ITRAX/XRF Analysis

The rectangular cut sections from XH1, CF1, CF2, and HN1 were used for analysis using the ITRAX Core Scanner (Core Analytical Systems; X-Ray Fluorescence; McMaster University Coring Facility) using the Cr X-ray source (10mA exp. time 15s step size 200µm) which were similar parameters used by Kovacs et al. (2017) for analysis of the calcite rafts. These rectangular sections were labelled: A, B C, etc. Samples A were used for analysis. Samples LC1A, LC2A, XH2A, CF3A and HN2A were not cut into rectangular sections and were analyzed with the core scanner as the samples were too small, delicate, or contained large holes or pits which hindered analysis.

4.4.2 Isotope analysis

High-resolution sampling (every mm) of the sectioned samples used a diamond tipped Foredom hand drill and followed any visible growth lines if present. Approximately, 1-9 mg was drilled for isotope analysis. Analysis was conducted at McMaster University by the Stable Isotope Research Lab Research Group for Stable Isoprologues - MSRI, and 0.1 mg of sample material was reacted with phosphoric acid and ^{13}C and ^{18}O were measured with a Thermo Finnigan DELTAplus XP continuous-flow isotope ratio mass spectrometer. All values were reported as $\delta^{13}C$ and $\delta^{18}O$ relative to the Vienna PeeDee Belemnite Standard for carbonates and Vienna Standard Mean Ocean Water for water samples. For XH2A 5 (3 repeats) the deviation was 0.12‰ for $\delta^{13}C$ and 0.03‰ for $\delta^{18}O$; XH2A 10 (3 repeats) the deviation was 0.18‰ for $\delta^{13}C$ and 0.002‰ for $\delta^{18}O$; and CF2A 2.1 (3 repeats) the deviation for $\delta^{13}C$ and $\delta^{18}O$ was 0.43‰. Uncertainty is 0.05‰ for $\delta^{13}C$ and 0.09‰ for $\delta^{18}O$ for all other samples.

4.4.3 ICP-OES Analysis

Approximately, 250 mg was used for ICP-OES (Inductively Coupled Plasma-Optical Emission Spectrometry) was used for samples CF3A and HN2A and all other samples used ≈2-3 mg for ICP-OES. Sodium infusion was used for calcium concentrations. Analysis was conducted by Activation Laboratories in Ancaster Ontario. The elements analyzed were Ca, Al, Fe, S, Sr, K, Ti, and Mg in % concentration while Mn and Sr were in ppm. Uncertainty for each element is: Mn 5ppm, Sr 1ppm, Al 0.01%, Ca 0.01%, Fe 0.01%, Mg 0.01%, S 0.01%, Ti 0.01%, K 0.01%.

4.4.4 Strontium Isotope Geochemistry

The samples (10 mg) were digested with acid and strontium was isolated using a cation exchange column. The $^{87}Sr/^{86}Sr$ ratios were analyzed with a Thermo-Finnegan Triton thermal ionization mass spectrometer (TIMS) using a 1-2 zone Re filament. One in five samples is repeated and 200 discrete measurements are made and variability of measured $^{87}Sr/^{86}Sr$ is ±0.000015 2σ. NIST-SRM-987 ($^{87}Sr/^{86}Sr$ = 0.710245 $2\sigma_{\bar{x}}$ ±0.000015) was used as a standard normalization and to correct for Rb interference.

4.4.5 Radiocarbon Analysis

The outer 0.5 cm was sampled for radiocarbon analysis in CF2A, CF3A, and HN1A. Radiocarbon dating was performed at Direct AMS Radiocarbon Dating in Seattle, Washington, USA. Calibration for radiocarbon dating used OxCal 4.4 Interface version 168C (July 7 2023). Atmospheric data was gathered from Reimer et al., 2020 and the curve was calibrated by Bronk Ramsey (2021).

Chapter 5

Results

5.1 Water Mass Characteristics

5.1.1 Xul Ha Cenote

Where XH1A was sampled, there was a temperature of 25.2 °C, pH = 6.3, conductivity of 2.24 mS/cm and a salinity of 1.15 ppt. Where XH2A was sampled, the temperature was 26.3 °C, pH = 6.2, conductivity = 2.85 mS/cm, and salinity of 1.16ppt.

5.1.2 Cenote Water Profile

In Cenote Fatima, the MeWM is from 0 to -36 m in depth, the halocline is at -36 m, the MxWM is from -36 m to -43 m (Figure 6). From 0 to -10 m the temperature decreases from 26.8 °C to 24.5 °C and from -10 m to -43 m the temperature remains constant at ≈24 °C but slightly increases in Mx/MaWM (Figure 6). Salinity is constant in the MeWM, increases quickly to 35psu in the MxWM and remains relatively constant in the MaWM (Figure 6). The pH is ≈7.5 at the surface then drops to 7 at approximately -7 m and remains constant until the halocline where the pH increases to 7.5 in the Mx/MaWM (Figure 6). Oxygen saturation is high at 100% close to the surface then decreases to 0% at -13 m and from -26 m to -36 m the oxygen saturation increases to 50% and then returns to 0% in the MaWM (Figure 6).

5.1.3 Hoyo Negro Water Profile

The water mass characteristics in Hoyo Negro were collected by Kovacs et al. (2017) from a depth of 0 m to 45 m and are less variable (temperature, pH) than Cenote Fatima because the water is not exposed to sunlight except by a small opening in the ceiling of Ich Balam. Temperature is constant (25.2 °C) in the MeWM and increases in the MxWM to 25.3°C

and then is 25.5°C in the MaWM (Figure 7). Salinity in the MeWM is < 1ppt then it increases to 35ppt at -18 m in the MaWM with a relatively sharp transition at the halocline (Figure 7). The pH was 6.8 and decreases in the MeWM to 6.6 with increasing depth and is 7.2 in the MaWM (Figure 7). Oxygen saturation is 20% in the MeWM and it increases to ≈35% in the MaWM (Figure 7). La Concha is in close proximity to Hoyo Negro, so water mass characteristics are similar.

5.2 Morphological Characteristics and Minerology

XH1A, from Xul Ha, has a slight dark green outer coating that extends ≈0.5 cm into the top layer (Figure 8). XH1A was collected on a branch that was sitting on a rock shelf in shallow water ≈1-5 cm in depth with wave action. Bivalve shells were also found on the outer layer of the sample and are most likely Dreissena a mylitiod bivalve (Castro-Contreras et al., 2014; Gischler et al., 2008). The growth starts out thrombolytic at the outer edge but becomes more stromatolitic with distinct regular layers/lines (black, dark brown, green, etc.) towards the center (Figure 8). The sample grew on a large branch and it is crescent moon shaped with inner layers matching the curvature of the branch. The inner most part of the sample is dark brown from the branch which provided a substrate for growth. XH1A is 11 cm in width and 4 cm in length and XRD indicates the minerology contained calcite (Supplementary Figure 12).

XH2A, from Xul Ha, also has a dark green outer edge but is fainter than XH1A. XH2A is ≈9 cm long and ≈8 cm wide (Figure 9). XH2A was collected along the shoreline on top of the sand at ≈30 cm in depth. The sample is thrombolytic in structure with no distinct layering and is light grey similar to XH1A (Figure 9). The sample has the same bivalve shells as XH1A and the sample

is very porous and micritic with large voids (≈0.3 cm). XRD indicates that carbonate is calcite (Supplementary Figure 12).

CF1A, from Cenote Fatima, has a distinct white central core with a tan outer layer that has elongated irregular growth lobes that point towards the light CF1A is oval in shape and is 12 cm in width and 6 cm in length; Figure 9). The white central core is composed of a dolomite/calcite mixture according to XRD results and the tan outer layer is calcite that is micritic texture. (Supplementary Figure 13). There are growth rings present in the cross sections, but they are not well defined throughout the sample. CF1A was collected underwater at -13 m in depth.

CF2A, from Cenote Fatima, was also collected underwater at -13 m in depth. It is more circular in shape (≈10 cm in length and ≈8.5 cm wide) than CF1A, but also has a white central core and a tan outer layer with growth lobes radiating outwards which are oriented like CF1A (Figure 9). XRD indicates that the white central core is also a mixture of dolomite/calcite and the tan outer layer is calcite (Supplementary Figure 13).

CF3A, from Cenote Fatima, has a light tan outer edge and a white-light grey interior and is 11 cm long and 6.5 cm wide. CF3A was along the cenote wall submerged at -27 m. It is composed of long branches and is very porous and is micritic (Figure 9). Branches radiate towards the top of the sample and there are no visible growth rings in the cross section (Figure 9). XRD indicates calcite mineralogy and a small peak for calcium sulfate, but this unlikely due to the small sulfur values in the ICP-OES data (Supplementary Figure 5, 14).

HN1A, from Hoyo Negro, is largely circular (5 cm wide × 7 cm long) and is light tan in color and the exterior has a "cauliflower-like" texture (Figure 8). The outer portion of the sample appears to be slightly dissolved as the growth lobes are roundish and in the cross section, they are shown to be arranged in branches that radiate outwards. The thin section shows an interior crystalline structure (sparry; Figure 8) and no growth lines were observed. The minerology is calcite as determined by XRD (Supplementary Figure 10). HN1A was sampled on the pit wall at -18 m depth.

HN2A, from Hoyo Negro, is a sub-sample (6.5 cm × 3.5 cm) from a larger speleothem (Figure 8). The outer edge is dark brown and alternates with chalky white layers (Figure 8). The dark brown layers have visible accretion lines, whereas the white layers are micritic and lack structure. XRD shows that both the dark brown and white layers are calcite (Supplementary Figure 11). HN2A was collected at -45 m at the bottom of the pit.

LC1A, from La Concha, is a stalactite collected from the cave ceiling and is 10 cm long and 2 cm wide (Figure 8). It was originally a soda straw which then had secondary growth on top of the stalactite. The outer layer has small irregular and elongated lobes that are perpendicular to the original soda straw (Figure 8). XRD indicates that LC1A was composed of anhydrite and calcium sulfate however the ICP-OES data shows low sulfur concentrations so the XRD may not be correct and needs further replication of results (Supplementary Figure 8, 14).

LC2A, from La Concha, is small and elongated measuring 5.6 cm in width and 2.1 cm in height. It has as an irregular shape with a rough outer texture (Figure 8). Distinct concentric layers were observed in the cross section of the sample (Figure 8). The XRD results indicate the

sample was composed of calcite and calcium sulfate but this may not be correct as discussed by LC1A (Supplementary Figure 9, 14). Both LC1A and LC2A were submerged at -12 m depth.

5.3 ICP-OES Data

5.3.1 Sr/Ca

Xul Ha has high Sr/Ca values compared to the other samples that range from ≈0.01 to ≈0.016, however, the values are also variable between the two locations in Xul Ha (XH1A and XH2A).

Cenote Fatima samples CF1A and CF2A have lower average Sr/Ca values (0.0015) than the deeper sample of CF3A which had an average value of 0.0020 (samples taken from the inner limestone core in CF1A and CF2A were excluded).

In La Concha, LC1A had less Sr then LC2A as the average Sr/Ca value for LC1A is 0.00087, and LC2A had an average value of 0.00146. HN1A had an average Sr/Ca of 0.0011 and HN2A was at 0.00088.

5.3.2 Mg/Ca

Cenote Fatima, Hoyo Negro and La Concha show strong correlation between Mg and Sr. Cenote Fatima samples from -13 m depth (CF1A and CF2A) to -27 m(CF3A) shows an increasing trend with an r^2 value of 0.82 with CF1 and CF2 having less Mg and Sr than CF3 (Figure 12). Hoyo Negro has an increasing trend (HN1A and HN2A) but HN1A has more Mg and Sr than HN2A but the r^2 value is only 0.51 (Figure 12). La Concha samples follow a similar increasing trend as Cenote Fatima and has an r^2 value of 0.92 (Figure 12).

5.3.3 S/Ca

Xul Ha Cenote has the highest average S/Ca values out of all the locations at 0.019 for both XH1A and XH2A and the S/Ca values are highly variable between the two locations. There is a strong correlation with Sr and S with an r^2 value of 0.99 for XH samples (Figure 13).

Cenote Fatima S/Ca samples show slightly higher values than Hoyo Negro and La Concha. There are no trends for Sr/Ca and S/Ca for Cenote Fatima (CF1A, CF2A and CF3A) which exclude the inner core samples (CF1A and CF2A).

Hoyo Negro has an inverse trend with depth as there is more S/Ca in HN1A than HN2A. There were no trends between S/Ca and Sr/Ca in La Concha or Hoyo Negro samples (Figure 13).

5.4 Itrax Elemental Data

Sr/Ca has very good correlation between ICP-OES and XRF (average values over a sampling period) with an r^2 of 0.98 (Figure 14). However, ICP-OES and XRF values cannot be directly compared because of analytical differences. Likewise, the S/Ca values have a good correlation with an r^2 of 0.96 (Figure 15). Sr/Ca and S/Ca showed good correlation between the ICP-OES and XRF data because these were relatively abundant elements as discussed in Gabriel et al. (2022).

XH1A and XH1B both have a decreasing trend from outer to inner layer (Sr/Ca values ranging from ≈0.0075-≈0.0045) with two small increases in the same position as shown by the arrows in Figure 16. CF1A and CF1B also show a decreasing trend with Sr/Ca values ranging from ≈0.0011 to ≈0.0009 for CF1A and ≈0.0003 to ≈0.0001 for CF1B. CF2A, CF2B, and CF2C also

show a decreasing trend with Sr/Ca values going from ≈0.0003 to ≈0.0001 and a similar dip with the division between the outer layer and inner core (Figure 16).

For S counts there is less consistency within and between samples. Within the sample for XH1B the S counts are consistent with Sr/Ca and are decreasing from outer to inner layers but overall, there are no strong trends in any of the samples (Figure 16).

5.5 Isotope Geochemistry

XH1A had an average $\delta^{13}C$ value of - 3.33‰ and the $\delta^{18}O$ is -6.20‰. XH2A has broadly similar values with the average $\delta^{13}C$ of -2.52‰ which is slightly higher than XH1A and the $\delta^{18}O$ value is similar to XH1A at -6.05‰. In XH1A, the $\delta^{13}C$ and $\delta^{18}O$ values are more variable ranging from -2.5‰ to -4.5‰ and -5.9‰ to -6.4‰ respectively (Supplementary Figure 1). For XH2A the $\delta^{13}C$ values at the outer edge are slightly higher at -1.5‰ then the values decrease slightly towards the center and $\delta^{18}O$ shows an inverse trend as the values increase towards the center from -6.2‰ to -5.9‰ (Supplementary Figure 2).

Crossplots of the Cenote Fatima samples have a strong increasing trend with $\delta^{13}C$ and $\delta^{18}O$ (r^2 ≈1.0) which include the inner core values of CF1A and CF2A (Figure 11). CF1A and CF2A have average $\delta^{13}C$ values (not including the inner core) of -9.62‰, and -10.24‰; and the average $\delta^{18}O$ values are very similar at -5.69‰, and -5.67‰. However, CF3A is more enriched by ≈3‰ as the average $\delta^{13}C$ value is -7.65‰ and the average $\delta^{18}O$ is -3.95‰. Within CF1A there is an overall decrease from exterior to interior (≈5‰) in both isotopes marking the transition between the outer and inner layers. For CF2A the $\delta^{13}C$ and $\delta^{18}O$ values are consistent within the outer layer and there is a sharp increase of ≈4‰ at 1.9 cm marking the transition between the

inner and outer layers (Supplementary Figure 4). In CF3A the $\delta^{13}C$ are relatively consistent (-7.5‰ to -7.6‰). The $\delta^{18}O$ shows a small decreasing trend (0.3‰) from 1 to 4.5 cm (Supplementary Figure 5).

In Hoyo Negro, the average $\delta^{13}C$ for HN1A is -6.08‰ and the $\delta^{18}O$ is -6.62‰; while in HN2A the $\delta^{18}O$ is -3.79‰ and $\delta^{13}C$ is -8.23‰. There is an increase in the average $\delta^{18}O$ of ≈ 3‰ from HN1A to HN2A while there is a ≈2‰ decrease in the $\delta^{13}C$ (Figure 11). In HN1A, there is a slight enrichment trend in $\delta^{13}C$ from the outside edge to the interior while the $\delta^{18}O$ remains quite constant (Supplementary Figure 6). In HN2A there is a decreasing trend (less enriched) for both $\delta^{13}C$ and $\delta^{18}O$ (Supplementary Figure 7). There is a small peak in $\delta^{13}C$ at 1 cm of ≈2‰ as it transitions from the brownish outside edge to the whitish inner layer.

For the La Concha samples, LC1A shows a sharp decline (≈-5.5 to -9‰) from outer edge to the interior in both $\delta^{13}C$ and $\delta^{18}O$ values which is also the case for LC2A (≈-0.8‰ to ≈-1.4‰; Supplementary Figure 8, 9). La Concha samples follows a strong increasing trend between $\delta^{13}C$ and $\delta^{18}O$ (r^2 = 0.98; Figure 11). The average $\delta^{13}C$ value for LC1A is -8.52‰ and the $\delta^{18}O$ is -6.61‰ while LC2A is more enriched as the average $\delta^{13}C$ value is -0.83‰ and the $\delta^{18}O$ is -2.77‰.

5.6 $^{87}Sr/^{86}Sr$ Geochemistry

For Xul Ha (XH1A), the outer layer had an $^{87}Sr/^{86}Sr$ value of 0.70768 and the interior was similar at 0.70763 (Supplementary Figure 1).

In Cenote Fatima, CF3A had a with a value of 0.70886 and is slightly more marine than CF1A/CF2A ($^{87}Sr/^{86}Sr$ of modern sea water is 0.709175; Kovacs et al. 2017; Supplementary

Figure 5). CF2A had a value at 0.70845 in the brown outer layer and the dolomite/calcite core was more marine at 0.70898 (Supplementary Figure 4).

In Hoyo Negro, HN2A had an $^{87}Sr/^{86}Sr$ value that is more marine than HN1A. HN1A 0.70868 and 0.70867 (Supplementary Figure 6). HN2A had similar to modern sea water at 0.70914 in the dark brown layer, the middle was 0.70916 and the white layer was 0.70920 (Supplementary Figure 7). In La Concha, LC1A had 0.70621 at the outer edge (growth lobes) and near the interior it was 0.70866. LC2A also had more marine values at 0.70904 on the outer edge and the interior was 0.70908.

There are no trends with $^{87}Sr/^{86}Sr$ and Sr/Ca for HN or LC. For CF2A and CF3A there is a good trend between $^{87}Sr/^{86}Sr$ and Sr/Ca with an r^2 value of 0.82 (Figure 17).

5.7 Radiocarbon dating

Samples from CF2A (depth -13 m) and CF3A (depth -27 m) were dated at 8112 ± 35σ cal. yr. BP, and 9224 ± 43σ cal. yr. BP respectively (Figure 10). HN1A had no radiocarbon and was dated to be greater than 45,000 cal. yr. BP (Supplementary Table 1). Using 1267 cal. yr. BP as hardwater correction from Kovacs et al., (2017) the calibrated ages for CF2A was 7591 cal. yr. BP and 8890 to 8646 BP for CF3A.

Chapter 6

Discussion

Determining a biogenic origin for microbialite formation is often difficult and not always clear. Morphology and layering can provide evidence as to a biological origin(Burne & Moore, 1987 and references therein), however, in a cave environment there are abiotic formations that share broadly similar structures and could be geochemically similar. Here, we discuss how known microbialites and unknown carbonate structures in Xul Ha, Cenote Fatima, and Hoyo Negro relate structurally and geochemically with current hydrogeochemistry to determine their origins.

Abiotic cave formations can be categorized in two groups: dripstones which form from dripping meteoric water such as stalagmites, stalactites; and flowstones which accrete on the walls and floors caves (Fairchild & Baker, 2012). Most speleothem morphologies (curtains, soda straws, stalactites, and stalagmites etc.) form from dripping or flowing water resulting in degassing of carbon dioxide and carbonate precipitation (Fairchild & Baker, 2012). Cave popcorn (bulbous) and helictites form with evaporation in splash zones from dripping water (Fairchild & Baker, 2012). Flowstones that are botryoidal and mamillary in morphology form under flowing water on cave floors or walls (Fairchild & Baker, 2012; Wróblewski et al., 2017). Hells Bells are subaqueous speleothem formations and are thought to be formed by changing levels of the redox zone with the help of microorganisms (underwater speleothems; Stinnesbeck et al., 2018; Ritter et al., 2019).

The presence of layers within carbonate buildups have been used to indicate a biogenic origin (Burne & Moore, 1987 and references therein). If the metabolism is photolytic and aerobic then the layers will be more definitive near the top and disappear near the bottom, if it is anerobic it will typically be layered throughout the entire structure (Tice et al., 2017). Changes

in isotopes and elements within the accreting layers within the microbialite could reflect changes in sedimentation, microbial processes, or changes in water conditions. It is often difficult to determine which changes are biogenic or not. Detailed elemental analysis using Mesoscale XRF Tice et al., (2017) determined laminated and cross laminated textures were present but were not were not visible even in the thin sections. Isotopic signatures (ex. $\delta^{13}C$ enrichment) and elemental signatures (Sr, S, Mg) may provide evidence to determine the microbialite origins and determine if they are abiotic (speleothem) or biotic. For fractionation, original DIC values are needed and some formations are thousands of years old. DIC values were not collected in Xul Ha which are thought to be accreting recently (See 6.1.1). The $^{87}Sr/^{86}Sr$ values may also determine whether a structure formed above or below water as the value relates to the source of water and the geologic age of the limestone. So, the aquifer which resides within deeper and older limestone will have a different$^{87}Sr/^{86}Sr$ ratio than drip water from younger overlying limestone. So, in our sites Hoyo Negro and La Concha the overlying Pleistocene limestone will have an $^{87}Sr/^{86}Sr$ ratio close to modern seawater at 0.709175 while the aquifer that is within older Miocene limestone t has a ratio of 0.70860 (Kovacs et al., 2017). Radiocarbon dating of microbialites can also determine whether they are actively growing or not and provides ages to compare with independent aquifer water chemistry (such as calcite rafts from Kovacs et al. 2017). Although these techniques/evidence may not be wholly diagnostic and are often combined with other techniques (ex. SEM, biomarkers, etc.) they may be useful when other techniques are not available (extra-terrestrial investigations).

6.1 Xul Ha Cenote and Laguna Bacalar

6.1.1 Radiocarbon Dating

We do not have radiocarbon dates for XH1A and XH2A but they are both likely recent formations. XH1A grew on a branch in shallow water (≈15cm in diameter) and XH2A was a small knob along the shoreline (9cm in diameter). However, Gischler et al., 2008 dated the Bacalar samples to ≈8-5 cal. kyr. BP with the ones on the eastern side were younger with an average of 6-3 to 7-0 cal. kyr. BP (Gischler et al., 2008). These ages are likely not correct since they did not use a hardwater age correction so the ages could be quite a bit younger.

6.1.2 Morphological Characteristics and Minerology Origins

XH1A had light greenish layers inside and a darker greenish tinged outer surface indicating chlorophyll and active growth suggesting a modern age. XH1A was stromatolitic and had visible layers in the cross section and with the thin sections (Figure 9 and 10). XH2A is thrombolytic and had no visible layers (Figure 10). Both of these samples were growing in full light which also suggests the presence of chlorophyll on both of the outer surface of the samples. Reid et al. (2000) demonstrated the role that microbes play in accretion and laminations.

The exterior of XH2A looks very similar to the Dichtrix knobs found in Storr Lake, Bahamas by Fowler, (2011) which were shown to have a biogenic origin. These microbialites also had trapped bivalve shells. Fowler, (2011) found that microbialites along the shorelines of Storr Lake seem to trap and bind sediment and also trap bivalve shells. Both XH1A and XH2A were found in shallow shoreline areas and in full light conditions and it is also possible that sediment from the bottom of the lagoon was trapped and bound with the bivalve shells.

However, in Xul Ha, the bivalve shells were articulated indicating they were likely living in the outer layers of the structure.

The microbialites described by Gischler et al., (2008) in Laguna Bacalar were also very similar in appearance to XH1A and XH2A having the same bivalve shells embedded in the structure and the same greyish appearance. Some layering was observed in their samples but most of their samples were thrombolytic in appearance; Gischler et al. (2008) also reported aragonite with micritic texture whereas our XRD shows calcite for our samples (XH1A and XH2A) (Figure 10). Micrite can form from inorganic precipitation or breakdown (abiotically) or microbial dissolution or reprecipitation from biological organisms) (Lucia, 2017). *Homeothrix* and *Leptolyngbya* are cyanobacteria that are largely responsible for the calcium carbonate precipitation as they uptake CO_2 during photosynthesis and can lower the pH through biochemical reactions (Gischler et al., 2008)**.** Gischler et al. (2008) found cyanobacterial filaments within the sediment and found nanoscale Mg calcite crystals on the filaments (with SEM).

Castro-Contreras et al. (2014) suggested two different mechanisms for the formations of the microbialites in Laguan Bacalar. In microbialites that were more stromatolitic it was suggested that the formation was made purely out of $CaCO_3$ precipitation from high concentrations of Ca^{2+} and HCO_3^- present in the water. SEM images from Castro-Contreras et al. (2014) showed that micrite precipitates on the filaments that were created by cyanobacteria and creates a mold in which more precipitation and bacteria growth can occur. Laminations occur as the cyanobacteria migrate upwards to be exposed to more light as the micrite builds up (Castro-Contreras et al., 2014). Castro-Contreras et al. (2014) found a lack of detrital grains

(from the bottom of the lagoon) in the stromatolitic microbialites showing that there was no trapping and binding. For thrombolytic microbialites, however, trapping and binding did occur as Castro-Contreras et al. (2014) found peloids and bioclasts present and the same grains were seen in the collected sediment at the bottom of Laguna Bacalar. As the microbialites grow they have more surface area and trap more suspended sediment leading to a thrombolytic morphology as cyanobacteria constantly move upwards leading to internal clotting and no laminations structure (Castro-Contreras et al., 2014). Gischler et al. (2008) also acknowledged that there is likely a combination of pure calcite precipitation and trapping and binding. XH1A and XH2A seem to follow this trend as XH1A was exposed to less sediment as it grew on a branch on a rock shelf with little suspended sediment whereas XH2A was sitting in sandy substrate with suspended sediment. The microbialites seem to follow the same trend presented in Castro-Contreras et al. (2014) for microbial mat formation in Laguna Bacalar.

6.1.3 Elemental Trends

Xul Ha samples (XH1A and XH2A) had high the S, Sr, and Mg values relative to Hoyo Negro, La Concha, and Cenote Fatima samples (Figures 12, 13). In Cenote Azul which is only a few 100 meters away from Laguna Bacalar; Sr and S in the water had a strong direct relationship (r^2 = 0.98; Perry et al., 2002). There is also a strong correlation between our S/Ca and Sr/Ca values for XH1A and XH2A (r^2 = 0.99; Figure 13). The evaporite region has higher strontium and sulfur then in any other region in the Yucatan (Perry et al., 2002). The high concentration of Sr and S is likely from gypsum and anhydrite dissolution in the underground karst system of the evaporite region (Ward et al., 1985; Perry et al., 2002, 2009). The Sr/Ca ratio values, are a little higher in Laguna Bacalar (0.0240; average from Castro-Contreras et al. 2014: Figure 23) than Xul

Ha (XH1A average value of 0.0113 (1σ: 0.00072) and XH2A average value of 0.0110 (1σ: 0.0034)). The Sr, Mg, and S values largely reflect regional and recent water chemistry and are (≈10×) higher than the other studied locations from Holbox Fracture/Xel Ha Zone (Hoyo Negro, La Concha, and Cenote Fatima).

From outer to inner edge for XH1A there is variation between Sr and S in both ICP-OES and XRF data as well as in XH2A however because we have no dating it is difficult to determine the cause of these variations.

6.1.4 Isotope Geochemistry

In Xul Ha, XH1A showed little variation with an average $\delta^{13}C$ value of - 3.33‰ (1σ = 0.54) and the $\delta^{18}O$ at -6.20‰ (1σ = 0.12; Figure 22). XH2A has similar values with the average $\delta^{13}C$ of -2.52‰ (1σ = 0.82;) which is slightly higher than XH1A but the $\delta^{18}O$ value is similar at -6.05‰ (1σ = 0.12; Figure 22). There is little variation between the $\delta^{18}O$ which is expected as they formed in the same body of water but the slight difference in the $\delta^{13}C$ is of interest as XH2A is slightly more enriched. There are no visible layers in XH2A and it grew in slightly deeper and more turbid waters than XH1A. The values are lower than Pavilion Lake (average = +2.3‰ (1σ = 0.48; Figure 22; Brady et al., 2010). Brady et al., (2014) found that the $\delta^{13}C$ values decreased with depth and with incident light.

Castro-Contreras et al., (2014) studied the microbialites in Laguna Bacular which had $\delta^{13}C$ average values of -0.82‰ (1σ = 0.43) which are much higher than our XH samples (Figure 22). The $\delta^{18}O$ value is also higher at -5.21‰. The sediment had average $\delta^{13}C$ values of -1.53‰ (1σ: 0.075) and the $\delta^{18}O$ -5.10‰ (1σ: 0.21) and the $\delta^{13}C$ from the bivalve shells were at -4.71‰

(1σ: 0.77) and the $\delta^{18}O$ was around -4.56‰ (1σ: 0.50) (Castro-Contreras et al., 2014). XH1A and XH2A $\delta^{18}O$ are closer to the sediment average value of the all the microbialites collected in Castro-Contreras et al. (2014). The average $\delta^{13}C$ value from XH1A is within the range of the bivalve's shells meaning XH1A could have calcite precipitated from the water like the shell. XH2A is ≈-2‰ and is closer to the sediment value than XH1A meaning it could have trapped sediment as well as precipitated. It is likely that XH1A and XH2A have a mixture of both sediment and bioprecipitates.

6.1.5 Xul Ha Cenote and Laguna Bacalar $^{87}Sr/^{86}Sr$ Geochemistry

The outer layer of XH1A had an $^{87}Sr/^{86}Sr$ value of 0.70768 and the interior was 0.70763 (Supplementary Figure 1). The interior matches closely with the water values from Cenote Azul that has a ratio of 0.70764 which is ≈100 m away from Xul Ha. The outer layer in XH1A is slightly more marine (sea water= 0.709175) and matches more closely with the Laguna Bacalar value of 0.70767 (Paytan et al. n.d.). We only have two values from XH1A, so these results need to be corroborated with further study, but the change could be due to changes in water to Xul Ha.

6.2 Cenote Fatima

6.2.1 Radiocarbon Dating and Groundwater Levels

The radiocarbon dates for CF2A were 7591 cal. yr. BP at -13 m and CF3A was 8990 cal. yr. BP at -27 m (Figures 18, 25, Supplementary Table 1). These dates were corrected with hardwater using 1267 cal. yr. BP calculated by Kovacs et al. (2017) by radiocarbon dating of paired terrestrial seeds and calcite raft cores in Hoyo Negro and Ich Balam. Using Kovacs et al. (2017; Krywy-Janzen et al., (2019) Collins et al. (2015a) and Holocene sea level data, the water

levels at 7600 cal. yr. BP were at ≈-10 m and ≈-25 m at 9000 cal. yr. BP (Figure 25). This indicates that the microbialites formed at 2-3 m of water depth in each period and thus were within the upper photic zone where the water may have been oxygenated based on the modern water profiles (Figure 6; 25). The shallow growth window and well-oxygenated conditions is predictable for cyanobacteria growth.

6.2.2 Morphological Characteristics and Minerology Origins

CF1A and CF2A have elongated growth lobes that pointed towards the light during growth and CF3A also had a more elongate less dense structure and was almost coral-like in shape (Figure 9). The microbialites in Storrs Lake have similar elongated knobs like those found in CF1A and CF2A. Faint growth lines are seen in both CF1A and CF2A while CF3A has no visible growth lines. CF1A and CF2A had outer layers that were dense as the thin sections show but CF3A was more porous (Figure 9, 10). Cenote Fatima samples likely grew from active calcite precipitation from cyanobacteria because there is a lack of suspended micritic sediment compared to Laguna Bacalar and Xul Ha. The color of Cenote Fatima is more reddish brown and not light gray like the Xul Ha samples which may be due to runoff and input of oxides from the limestone weathering, and/or phytoplankton and other fine particulate organics. Both Cenote Fatima and Xul Ha samples have micritic textures.

In Storrs Lake Paul et al., (2016) found that some microbialites seemed to have a darker granule structure that helped the microbialite attach to the bottom, but our microbialites (CF1 and CF2) were not attached and gently sat on the sediment and there was an outer layer of growth on the bottom of CF1A and CF2A surrounding the inner core (Figure 9). Perhaps the

bottom layer grew first then tipped over with changes in weight distribution resulting in a continuous outer core. There could also be other microorganisms present that do not need light such as nitrification or sulfate reducing bacteria that created the outer layers as found in Hells Bells (Stinnesbeck et. al., 2018; Ritter et al., 2019). More radiocarbon dating of the samples may show signs of accretion.

The difference in morphology between CF1A/CF2A and CF3A could be the amount of incident light. Although both microbialites grew at a similar water depth based on radiocarbon ages the amount of incident light may have differed because of karst topography. CF1A/CF2A are closer to the upper edge of the sinkhole while CF3A is at the deeper base of the cenote. Gregory et al., (2017) found an increase in primary productivity in the water column as the sea level rose in Little Salt Spring sinkhole in Florida as a result in change in incident sunlight. For CF3A there would less light due to the high angle needed to reach the bottom of the cenote. However, in the case of CF1A and CF2A which have less surface area and are more compact there was more incident light as they were located closer to the upper edge of the cenote. This change in light conditions due to the depth within the cenote may explain the morphological changes between CF1A/CF2A and CF3A. In the same way trapped and suspended sediment caused more thrombolytic structures with less laminations in Xul Ha (XH2A), the lack of incident light led to a less layered and more thrombolytic structure in CF3A.

6.2.3 Elemental Trends

The Sr/Ca average value (ICP-OES) for CF1A and CF2A are similar at 0.0015 and 0.0016 (1σ: 0.00000815; Figure 23) (neglecting the outer edge and inner core) and they both show an

increasing trend from outer to inner layers. CF3A has more Sr than CF1A/CF2A as the average Sr/Ca (ICP-OES) is 0.0024 (1σ: 0.00017; Figure 23) and shows an opposite trend of decreasing from outer to inner layers. Calcite raft cores from Hoyo Negro at 8300 cal. yr. BP and Ich Balam at 7600 cal. yr. BP show similar changes in the water chemistry. At 8300 cal. yr. BP the Sr/Ca (XRF) average was 0.049 (1σ: 0.02; Figure 23) and at 7600 cal. yr. BP the (XRF) value decreased to 0.0054 (1σ: 0.0098; Figure 23). The overall Sr/Ca trends (XRF) and reproducibility in CF1A and CF2A show that uniform growth occurred but perhaps at different rates (Figure 16).

S/Ca (ICP-OES) also shows a similar pattern as the Sr/Ca. The S/Ca (ICP-OES) average values for CF1A and CF2A are the same at 0.0016 and 0.0016 (1σ: 0.00000335). CF3A also has more S (S/Ca is 0.0019 1σ: 0.00012). S/Ca (ICP-OES) for CF1A shows an increasing trend from inner to outer layers. For CF3A there is an increasing trend (inner to outer layers) for S/Ca which is opposite of that for Sr/Ca. There were no significant trends between S and Sr as sulfur likely comes from a different source versus Xul Ha where the S was directly correlated with strontium and likely came from dissolution of gypsum. Particulate material incorporated into CF1A and CF2A could also be responsible for the variable S values.

Mg/Ca (ICP-OES) has an increasing trend with depth for CF1A and CF2A having less Mg then CF3 excluding inner core values. There was a strong trend between Mg/Ca and Sr/Ca (r^2 is 0.82; Figure 17). Sr and Mg are high in seawater versus freshwater suggesting a change in salinity between the growth periods of CF2A and CF3A. A similar change occurred in the Sr/Ca calcite raft cores from 7500 cal. yr. BP and 9000 cal. yr. BP and was ascribed to be changes in rainfall and mixing between the MeWM and MaWM (Kovacs et al., 2017).

6.2.4 Isotope Geochemistry

For hidden layering, $\delta^{13}C$ and $\delta^{18}O$ values show consistency for both CF1A and CF2A as they grew both side by side and likely at the same time. CF1A and CF2A $\delta^{13}C$ averages for the outer layer were respectively, -9.61‰ (1σ = 0.55; Figure 22) and -10.24‰ (1σ = 0.11; Figure 22) which is slightly different and suggests different periods of growth. CF3A had an average $\delta^{13}C$ value of 7.58‰ (1σ = 0.059; Figure 22)

Schorndorf et al. (n.d.) from Hells Bells reported a $\delta^{13}C$ value at ≈-8‰ from ≈9000-9600 yr. BP and at 2500- 7700 yr. BP the $\delta^{13}C$ was ≈-13‰ so there was a decrease of ≈4-5‰. We see the same decrease in the Cenote Fatima and Hoyo Negro samples. CF3A at ≈9000BP was -7.58‰ and CF2A at ≈7600BP was -10.24‰ with a change in about ≈3‰ (Figure 25). Hoyo Negro calcite rafts were dated at 8300 cal. yr.BP with an average $\delta^{13}C$ -6.44‰ and at ≈7600BP the $\delta^{13}C$ was -10.65‰ which also shows a ≈4‰ change suggesting there was an aquifer wide change that Kovacs et al. (2017) attributed to mixing between the MeWM and MaWM during the Holocene (Figure 25).

The average $\delta^{18}O$ SMOW for the MeWM in Cenote Fatima modern water was -4.42‰ and is close to the fresh water end member value (in the Yucatan) of -5.61‰ (Stoessell et al., 1989). The $\delta^{18}O$ for CF1A and CF2A respectively was -5.69‰ (1σ = 0.57) and -5.67‰ (1σ = 0.12; Figure 22). This matches the range of Hells Bells $\delta^{18}O$ of -6.36‰ to -4.34‰ from 9600 yrs. BP to present (Schorndorf et al., n.d.). However, at ≈9000 cal. yr. BP (CF3A) the $\delta^{18}O$ was -3.93‰ (1σ = 0.1) showing an increase of ≈2‰ that is not seen in the Hells Bells or Hoyo Negro calcite raft cores. In Hells Bells at 9600 yr. BP the $\delta^{18}O$ was closer to ≈-6‰. However, the $\delta^{13}C$ and $\delta^{18}O$ do

suggest some salinity change or changes in mixing between the MeWM and MaWM that could due to changes in climate i.e. increased rainfall leading to more flow in the groundwater and more turbulence or mixing (Kovacs et al., 2017). As discussed, there is a strong trend with the r^2 0.99 in cross plot of $\delta^{13}C$ and $\delta^{18}O$ (Figure 11).

6.2.5 $^{87}Sr/^{86}Sr$ Geochemistry

Cenote Fatima CF2A at ≈7600 cal. yr. BP had an $^{87}Sr/^{86}Sr$ value of 0.70845 in the outer layer and the inner core was 0.70898; and CF3A at ≈9000 cal. yr. BP had an $^{87}Sr/^{86}Sr$ ratio of 0.70866 (Supplementary Figures 4, 5). There is also a strong trend with Sr/Ca and $^{87}Sr/^{86}Sr$ r^2 = 0.87 which supports more mixing of the MeWM and MaWM.

For Hoyo Negro the $^{87}Sr/^{86}Sr$ value of the calcite raft cores at 8300 cal. yr. BP was 0.70846 (1σ = 0.00000340) and at 7600BP it was lower at 0.70832 (1σ = 0.00000387) showing a similar freshening like Cenote Fatima (Figure 25). This change is documented in two different regions (Hoyo Negro and Cenote Fatima) and likely indicates that the entire aquifer changed to fresher conditions at 7600 cal. yr. BP possibly due to increased drying conditions in the Holocene (Chappell, 2009; Kovacs et al., 2017).

6.3 Hoyo Negro and La Concha

6.3.1 Radiocarbon Dating/Past Sea level

HN1A was radiocarbon dated with an age >45,000 cal. yr. BP so the precise age is not known (Supplementary Table 1). However, if HN1A formed at or below water level the most recent periods that are possible based on Quaternary Sea level data: 1) 99,000 to 101,000 cal.

yr. BP; 2) 135,000 cal. yr. BP or 3) 117,000 to 125,000 cal. yr. BP (Chappell, 2009). Sea level was at ≈-18 m from 99,000-101,000 cal. yrs. BP and ≈-10 m at 135,000 cal. yr. BP and for 117,000 to 125,000 cal. yr. BP the sea level was at ≈+5 m above current sea level. It is most likely that HN1A formed around 117,000 to 125,000 cal. yr. BP as the sea level was at present levels for a long period of time but we can't be definitive without further dating. van Hengstem et al., (2009) found evidence in the Aktun Ha cave system of foraminifera that likely date to Stage 5e (125,000 years) and this is higher than present sea level. Current MeWM salinity in Aktun Ha is 1-1.5 psu while the Foraminifera would require brackish or marine conditions. This suggests a higher sea level with the sample located in the MxWM or MaWM. Further U-Th dating is needed to confirm exact age.

6.3.2 Morphological Characteristics and Minerology Origins

HN1A had a similar appearance to XH2A as it was globular in appearance but it was light brown in color and a cauliflower-like shape. The interior was different from the thrombolytic and micritic nature of XH2, with HN1A having no growth layering, and pronounced sparry crystalline branches (Figure 8). HN2A is a top portion of a larger stalagmite located on the bottom of Hoyo Negro and the chalky layers were thought to be microbial while the brown layers were speleothem. XRD shows calcite for both HN1A and HN2A (and no other mineral) and thin sections do not show any evidence of diagenesis.

Thin sections of HN1A show definitive euhedral crystals with no layering (Figure 10). Ritter et al. (2019) found dogtooth crystal shapes in the calcite of Hells Bells much like the Hoyo Negro samples and this seems to show slow inorganic growth of calcite but in underwater

conditions. López-Martínez et al. (2020) proposed underwater precipitation of Hells Bells where dissolved CO_2 bubbles provide a point of growth for calcite crystals on the surface of the bubbles. The crystals point outwards to the top where it is exposed to water. However, tetrahedral or pentagonal crystalline faces were observed when and it is difficult to prove that microbes are responsible for crystal orientation or precipitation (Castanier et al., 1999). A microbe can interfere with the intercrystallite boundaries making a wider gap causing a blocky topography (Jones, 2001) but this does not appear to be the case with HN1A. However, it is possible that HN1A had an original micritic texture that may have been diagenetically altered to sparry calcite.

LC1A seemed to have short elongated lobes or branches growing perpendicular from the stalactite that perhaps looked biogenic (Figure 8). LC2A was similar to a cave pearl which have also been attributed to biogenic activity as some have laminations that circle the core (Figure 8; Jones, 2001). Both LC1A and LC2A had visible accretion or growth layers.

6.3.3 Elemental Trends

Sr/Ca (XRF) in HN1A showed no consistent trend within HN1A but S/Ca (XRF) showed a slight decrease from outer to inner layers, however the ICP-OES shows an increase in both Sr and S (Supplementary Figure 6). This inconsistency between the measurements could be due to the detection limits of the XRF as the variability.

HN1A had an average Sr/Ca value (ICP-OES; neglecting outer layer) of 0.0011 (1σ = 0.00000653; Figure 23), S/Ca = 0.00029 (1σ:0.00011) and Mg/Ca = 0.014 (1σ = 0.00058). Average values for HN2A (ICP-OES) (neglecting outer layer) are Sr/Ca: 0.00088 (1σ = 0.00026;

Figure 23), S/Ca: 0.00063 (1σ = 0.00067) and Mg/Ca: 0.00065 (1σ = 0.00000273). HN1A and HN2A Sr/Ca match closely. From Ritter et al., 2018 the Hells Bells value for Sr/Ca was 0.000386 (1σ = 0.000059; Figure 23) which is closer to the stalagmite value of HN2A. LC1A has a higher outer Sr/Ca (ICP-OES; outer sample: 0.0009 and inner sample: 0.0008 possibly indicating splash-water formation of the lobes as the soda straw matches HN2A (average value = 0.0008; 1σ = 0.0002; Supplementary Figure 8). LC2A also has Sr/Ca values closer to HN1A suggesting that it could have formed in a pool of water (Supplementary Figure 9). However, Sr/Ca are often variable and hard to rely on to be diagnostic.

6.3.4 Isotope Geochemistry

HN1A had an average $\delta^{13}C$ value of -6.08‰ (1σ = 0.73) and $\delta^{18}O$ -6.62‰ (1σ = 0.65), and HN2A had a $\delta^{13}C$ value of -8.23‰ (1σ = 1.14) and an $\delta^{18}O$ of-3.80‰ (1σ = 0.64; Figure 22).

Kovacs et al. (2017) reported the calcite raft core from Ich Balam had an average $\delta^{13}C$ of -10.65‰ (1σ = 0.12) and an average $\delta^{18}O$ of -6.51‰ (1σ = 0.16) and the Hoyo Negro calcite raft core had a $\delta^{13}C$ value more enriched at -6.44‰ (1σ = 0.63) and the average $\delta^{18}O$ value was -6.51‰ (1σ = 0.18; Figure 22). The $\delta^{13}C$ and $\delta^{18}O$ in HN1A are nearly identical to the Hoyo Negro calcite raft core values suggesting an aquatic versus a drip water formation. HN2A formed in a dry cavern from overhead drip water and had values that were very different from the Hoyo Negro and Ich Balam calcite raft cores. HN2A has $\delta^{18}O$ values similar to a stalagmite in a costal sinkhole in the Yucatan which are from -3.5‰ to -7‰ from 2950 BP to 1550 BP (Medina-Elizalde et al., 2016). LC1A had average $\delta^{13}C$ and $\delta^{18}O$ values of -9.25‰ (1σ: 0.32) and -7.12‰ (1σ = 0.24; Figure 22) respectively and are closer to the calcite rafts in Ich Balam in Kovacs et al.

(2017) and could have formed in splashing water from the MeWM. LC2A had higher average $\delta^{13}C$ and $\delta^{18}O$ values of -0.82‰ (1σ = 0.60) and -2.90‰ (1σ = 0.38) respectively suggesting it formed in a separate and possibly evaporitic water source such as a shallow pool of water at the bottom of the cave passage (Figure 22).

6.3.5 $^{87}Sr/^{86}Sr$ Geochemistry

HN1A $^{87}Sr/^{86}Sr$ were 0.70868 and 0.70867 which are close to that of the calcite rafts in Hoyo Negro which have an average of 0.70846 (Kovacs et al., 2017; Figure 24, Supplementary Figure 6). The HN1A values are slightly more marine and may have formed closer to the halocline as the calcite rafts reflect the upper MeWM which may have been fresher. The close match between $\delta^{13}C$, $\delta^{18}O$, Sr/Ca and $^{87}Sr/^{86}Sr$ with the calcite rafts suggest that HN1A formed in the MeWM and perhaps closer to the MxWM sometime >45,000 cal. yr. BP. In HN2A, the stalagmite values are closer to modern sea water ranging from 0.70914 to 0.70920 indicating a drip water source of Sr from the upper Pleistocene limestone ceiling (Supplementary Figure 7).

The stalactite LC1A had an outer and inner $^{87}Sr/^{86}Sr$ values of 0.70862 and 0.70866 which is close to the calcite rafts possibly indicating a splash/drip water formation (Supplementary Figure 8). LC2A had higher $^{87}Sr/^{86}Sr$ values at 0.70904 and 0.70908 which is closer to the marine value of 0.709175 (Figure 24; Supplementary Figure 9). This likely indicates a mixed water source from both drip water source of strontium which would have a Pleistocene ratio and groundwater. The high, $\delta^{18}O$ value of 2.90‰ suggesting evaporation in a stagnant pool which may have dried up during parts of the year.

Chapter 7

Conclusion

1) Xul Ha had enriched $\delta^{13}C$ compared to the other locations sampled, and was growing in full light. XH1A had a stromatolite appearance whereas XH2A had a thrombolytic appearance. The thrombolytic appearance of XH2A likely formed because of more suspended sediment than XH1A which was stromatolitic. S and Sr were correlated (similar to other studies) indicating a Tertiary gypsum source of groundwater. $^{87}Sr/^{86}Sr$ also matched previous geochemistry (Perry et al., 2009;2002).

2) Using previous sea level and groundwater level data Cenote Fatima microbialites were both shown to grow in a shallow water depth of 2-3 m of water depth and in the photic zone. CF2A was dated at 7580 cal. yr. BP (-13 m) and CF3A was dated at 8990 cal. yr. BP (-27 m) and are not currently growing. CF1A and CF2A had growth lines and CF3A was more thrombolytic but al samples are likely biogenic formations. Incident light based on karst topography (cenote shape) caused the morphological changes documented between CF1A/CF2A and CF3A. The microbialites also show a ≈3‰ decrease in $\delta^{13}C$ which is also seen Hoyo Negro and Hells Bells (Cenote Zapote) (Kovacs et al., 2017; Schorndorf et al., n.d.). Decreasing trends in Sr/Ca and $^{87}Sr/^{86}Sr$ were observed and comparable to the calcite raft core records in Hoyo Negro reported in Kovacs et al. (2017).

3) HN1A (-18 m) in Hoyo Negro was dated to an age >45,000 cal. yr. BP and likely formed in Stage 5e where the ground water level was much higher than present. The geochemistry of HN1A matched closely with the Holocene calcite raft core from Kovacs et al., (2017) suggesting that it formed in the MeWM. HN1A was shown to have distinct crystals of calcite the branches radiate outwards towards the center and HN1A is likely abiotic/biotic like Hells Bells but more research is needed. HN2A was a piece of stalagmite that has no biogenic origin according to its

$^{87}Sr/^{86}Sr$ ratio (close to Pleistocene values) as it formed in dry conditions. LC1A (stalactite) and LC2A (cave pearl) were both collected at -12 m and are likely drip/splash water and shallow pool formations.

Bibliography

Águila, B., Yanez-Montalvo, A., Mercado-Juárez, R. A., Montejano, G. A., Becerra-Absalón, I., & Falcón, L. I. (2022). Microbialites show a distinct cyanobacterial phylogenetic structure and functional redundancy in Bacalar lagoon and Cenote Azul sinkhole, Yucatan Peninsula, Mexico. *FEMS Microbiology Ecology*, *98*(5), https://doi.org/10.1093/femsec/fiac039

Aitken, J. D. (1967). Classification and environmental significance of cryptalgal limestones and dolomites with illustrations from the Cambrian and Ordovician of Southwestern Alberta. *Journal of Sedimentary Petrology, 37*(4), 1163–1178 http://pubs.geoscienceworld.org/sepm/jsedres/article-pdf/37/4/1163/2804845/1163.pdf?casa_token=H0FfBu-XdeEAAAAA:tB9dqMvSYD_ahH5T_k-iRY_rafteh_Eik7XJgSfqU98Rne7K8zMrB3BtT7hIBGhWsOTcyEA

Banks, E.D, Taylor, N.M, Gulley, J, Lubbers, B.R, Giarizzo, J.G, Bullen, H, Hoehler, T. M, Barton, H. A, (2010) "Bacterial calcium carbonate precipitation in cave environments: A Function of Calcium Homeostasis." *Geomicrobiology Journal, 27*(5*),* 444–454., https://doi.org/10.1080/01490450903485136.

Beddows, P. A. (2004). *Groundwater Hydrology of a Coastal Conduit Carbonate Aquifer: Caribbean Coast of the Yucatán Peninsula, México*.(2309)[Ph.D Thesis, University of South Florida]. Kip Articles. https://digitalcommons.usf.edu/kip_articles/2309

Brady, A. L., Laval, B., Lim, D. S. S., & Slater, G. F. (2014). Autotrophic and heterotrophic associated biosignatures in modern freshwater microbialites over seasonal and spatial gradients. *Organic Geochemistry*, *67*, 8–18. https://doi.org/10.1016/j.orggeochem.2013.11.013

Brady, Allyson. L., Slater, Gregory. F., Omelon, Christopher. R., Southam, Gordon., Druschel, Gregory., Andersen, Dale. T., Hawes, Ian., Laval, Bernard., & Lim, Darlene. S. S. (2010). Photosynthetic isotope biosignatures in laminated micro-stromatolitic and non-laminated nodules associated with modern, freshwater microbialites in Pavilion Lake, B.C. *Chemical Geology*, *274*(1–2), 56–67. https://doi.org/10.1016/j.chemgeo.2010.03.016

Breitbart, M., Hoare, A., Nitti, A., Siefert, J., Haynes, M., Din1σale, E., Edwards, R., Souza, V., Rohwer, F., & Hollander, D. (2009). Metagenomic and stable isotopic analyses of modern freshwater microbialites in Cuatro Ciénegas, Mexico. *Environmental Microbiology*, *11*(1), 16–34. https://doi.org/10.1111/j.1462-2920.2008.01725.x

Burne, R. V, & Moore, L. S. (1987). Microbialites: Organosedimentary deposits of benthic microbial communities. In *Source: PALAIOS. 2*(3) 41-254. doi:10.2307/3514674

Cady, S.L, Farmer, J. D., Grotzinger, J.P., William Schopf, J and Steele, A. (2003) Morphological biosignatures and the search for life on Mars. *Astrobiology*, *3*(2), 351–368. http://doi.org/10.1089/153110703769016442

Castanier, S., Le Métayer-Levrel, G., & Perthuisot, J.-P. (1999). Ca-carbonates precipitation and limestone genesis-the microbiogeologist point of view. *Sedimentary Geology, 126*, 9–23.

Castro-Contreras, S. I., Gingras, M. K., Pecoits, E., Aubet, N. R., Petrash, D., Castro-Contreras, S. M., Dick, G., Planavsky, N., & Konhauser, K. O. (2014). Textural and geochemical features of freshwater microbialites from Laguna Bacalar, Quintana Roo, Mexico. *Palaios*, *29*(5), 192–209. https://doi.org/10.2110/palo.2013.063

Cavalazzi, B., Lemelle, L., Simionovici, A., Cady, S. L., Russell, M. J., Bailo, E., Canteri, R., Enrico, E., Manceau, A., Maris, A., Salomé, M., Thomassot, E., Bouden, N., Tucoulou, R., & Hofmann, A. (2021). Cellular remains in a ~3.42-billion-year-old subseafloor hydrothermal environment. *Science Advances*, *7*(29). https://doi.org/10.1126/sciadv.abf3963

Chatters, J. C., Kennett, D. J., Asmerom, Y., Kemp, B. M., Polyak, V., Nava Blank, A., Beddows, P. A., Reinhardt, E., Arroyo-Cabrales, J., Bolnick, D. A., Malhi, R. S., Culleton, B. J., Erreguerena, P. L., Rissolo, D., Morell-Hart, S., & Stafford, T. W. (2014). Late Pleistocene Human skeleton and mtDNA link Paleoamericans and Modern Native Americans. *New Series*, *344*(6185), 750–754. https://doi.org/10.1126/science

Chappell, J.M. (2009). Sea Level Change, Quaternary. In: Gornitz, V. (eds) Encyclopedia of Paleoclimatology and Ancient Environments. Encyclopedia of Earth Sciences Series. Springer, Dordrecht. (pp. 893–899). https://doi.org/10.1007/978-1-4020-4411-3_208

Collins, S. V., Reinhardt, E. G., Rissolo, D., Chatters, J. C., Nava Blank, A., & Luna Erreguerena, P. (2015). Reconstructing water level in Hoyo Negro, Quintana Roo, Mexico, implications for early Paleoamerican and faunal access. *Quaternary Science Reviews*, *124*, 68–83. https://doi.org/10.1016/j.quascirev.2015.06.024

Collins, S. V., Reinhardt, E. G., Werner, C. L., Le Maillot, C., Devos, F., & Meacham, S. S. (2015). Regional response of the coastal aquifer to Hurricane Ingrid and sedimentation flux in the Yax Chen cave system (Ox Bel Ha) Yucatan, Mexico. *Palaeogeography, Palaeoclimatology, Palaeoecology*, *438*, 226–238. https://doi.org/10.1016/j.palaeo.2015.07.030

Coutino, A., Stastna, M., & Reinhardt, E. G. (2020). Interaction of mangrove surface coverage and groundwater inputs on the temperature and water level near Tulum, Quintana Roo, Mexico: Observations and modelling. *Journal of Hydrology*, *583*(3). https://doi.org/10.1016/j.jhydrol.2020.124566

Des Maries, D.J. (1997). Isotopic evolution of the biogeochemical carbon cycle during the Proterozoic eon. *Organic Geochemistry, 27*(5–6), 185–193 https://doi.org/10.1016/S0146-6380(97)00061-2

Dodd, M. S., Papineau, D., Grenne, T., Slack, J. F., Rittner, M., Pirajno, F., O'Neil, J., & Little, C. T. S. (2017). Evidence for early life in Earth's oldest hydrothermal vent precipitates. *Nature*, *543*(7643), 60–64. https://doi.org/10.1038/nature21377

Donahue, J. (1969). Genesis of Oolite and Pisolite Grains: An Energy Index. *Journal of Sedimentary Petrology*, *39*(4), 1399–1411.

Dupraz, C., Reid, R. P., Braissant, O., Decho, A. W., Norman, R. S., & Visscher, P. T. (2009). Processes of carbonate precipitation in modern microbial mats. In *Earth-Science Reviews* 9(3), 141–162. https://doi.org/10.1016/j.earscirev.2008.10.005

Ercole, C., Cacchio, P., Cappuccio, G., & Lepidi, A. (2001). Deposition of calcium carbonate in karst caves: Role of bacteria in Stiffes Cave. *International Journal of Speleology 30*(1–4), 69–79 doi:10.5038/1827-806X.30.1.6

Fairchild, I. J., & Baker, A. (2012). Introduction to Speleothems and Systems. In Ray Bradley's (Eds) *Speleothem Science From Process to Past Environments.* John Wiley & Sons Ltd. (pp. 1–27). https://doi.org/10.1002/9781444361094.ch1

Fairchild, I. J., & Baker, A. (2012). Introduction to Speleothems and Systems. In Ray Bradley's (Eds) *Speleothem Science From Process to Past Environments.* John Wiley & Sons Ltd. (pp. 205–244).

Ferris, F. G., Thompson, J. B., & Beveridge, T. J. (1997). Modern freshwater microbialites from Kelly Lake, British Columbia, Canada [Article]. *Palaios*, *12*(3), 213–219. https://doi.org/10.2307/3515423

Fowler, Alexandre J., (2011) "*Stromatolitic Knobs in Storrs Lake, San Salvador, Bahamas: Insights into Organomineralization*" (180) [Master's Thesis, University of Connecticut]. Digital Commons@UConn. https://opencommons.uconn.edu/gs_theses/180

Gabriel, J. J., Reinhardt, E. G., Chang, X., & Bhattacharya, J. P. (2022). Application of µXRF analysis on the Upper Cretaceous Mancos Shale: A comparison with ICP-OES/MS. *Marine and Petroleum Geology*, *140*. https://doi.org/10.1016/j.marpetgeo.2022.105662

Gabriel, J. J., Reinhardt, E. G., van Hengstum, P. J., Beddows, P. A., Peros, M. C., & Davidson, D. E. (2009). Paleoenvironmental evolution of cenote Aktun Ha (Carwash) on the Yucatan Peninsula, Mexico and its response to Holocene sea-level rise. *Journal of Paleolimnology*, *42*(2), 199–213. https://doi.org/10.1007/s10933-008-9271-x

Gilli, A., Hodell, D. A., Kamenov, G. D., & Brenner, M. (2009). Geological and archaeological implications of strontium isotope analysis of exposed bedrock in the Chicxulub crater basin, northwestern Yucatán, Mexico [Article]. *Geology (Boulder)*, *37*(8), 723–726. https://doi.org/10.1130/G30098A.1

Gischler, E., Golubic, S., Gibson, M. A., Oschmann, W., & Hudson, J. H. (2011). Microbial Mats and Microbialites in the Freshwater Laguna Bacalar, Yucatan Peninsula, Mexico. *Advances in Stromatolite Geobiology*,*131*, 187–205. https://doi.org/10.1007/978-3-642-10415-2_13

Gischler, E., Gibson, M. A., & Oschmann, W. (2008). Giant Holocene freshwater microbialites, Laguna Bacalar, Quintana Roo, Mexico. *Sedimentology*, *55*(5), 1293–1309. https://doi.org/10.1111/j.1365-3091.2007.00946.x

Gonneea, M. E., Charette, M. A., Liu, Q., Herrera-Silveira, J. A., & Morales-Ojeda, S. M. (2014). Trace element geochemistry of groundwater in a karst subterranean estuary (Yucatan Peninsula, Mexico). *Geochimica et Cosmochimica Acta*, *132*, 31–49. https://doi.org/10.1016/j.gca.2014.01.037

Gregory, B. R. B., Reinhardt, E. G., & Gifford, J. A. (2017). The Influence of morphology on sinkhole sedimentation at Little Salt Spring, Florida. *Journal of Coastal Research*, *33*(2), 359–371. https://doi.org/10.2112/JCOASTRES-D-15-00169.1

Hildebrand, A. R., Penfield, G. T., Kring, D. A., Pilkington, M., Jacobsen, S. B., & Boynton, W. V. (1991). Chicxulub Crater: A possible Cretaceous/Tertiary boundary impact crater on the Yucatan Peninsula, Mexico. *Geology 19*(9), 867–871. doi:10.1130/0091-7613(1991)019<0867:CCAPCT>2.3.CO;2

James, N.P, Jones, B. (2016). *Origins of Carbonate Sedimentary Rocks*. Wiley.

Johnson, D. B., Beddows, P. A., Flynn, T. M., & Osburn, M. R. (2018). Microbial diversity and biomarker analysis of modern freshwater microbialites from Laguna Bacalar, Mexico. *Geobiology*, *16*(3), 319–337. https://doi.org/10.1111/gbi.12283

Jones, B. (2001). Microbial activity in caves - A geological perspective. *Geomicrobiology Journal*, *18*(3), 345–357. https://doi.org/10.1080/01490450152467831

Joshi, S. R., and Baskar, S. (2022) "Factors Affecting Biomineralization." *Microbiology Monographs,36,* 283–314., https://doi.org/10.1007/978-3-030-80807-5_8.

Kovacs, S. E., Reinhardt, E. G., Werner, C., Kim, S. T., Devos, F., & Le Maillot, C. (2018). Seasonal trends in calcite-raft precipitation from cenotes Rainbow, Feno and Monkey Dust, Quintana Roo, Mexico: Implications for paleoenvironmental studies. *Palaeogeography, Palaeoclimatology, Palaeoecology*, *497*, 57–167. https://doi.org/10.1016/j.palaeo.2018.02.014

Kovacs, S. E., Reinhardt, E. G., Chatters, J. C., Rissolo, D., Schwarcz, H. P., Collins, S. V., Kim, S. T., Nava Blank, A., & Luna Erreguerena, P. (2017). Calcite raft geochemistry as a hydrological proxy for Holocene aquifer conditions in Hoyo Negro and Ich Balam (Sac Actun Cave System), Quintana Roo, Mexico. *Quaternary Science Reviews*, *175*, 97–111. https://doi.org/10.1016/j.quascirev.2017.09.006

Kroopnick, P. M. (1984). The distribution ^{13}C of ΣCO_2 in the world oceans. In *Deep-Sea Research 32*, (1), 57–84. https://doi.org/10.1016/0198-0149(85)90017-2

Krywy-Janzen, A., Reinhardt, E., McNeill-Jewer, C., Coutino, A., Waltham, B., Stastna, M., Rissolo, D., Meacham, S., & van Hengstum, P. (2019). Water-level change recorded in Lake Pac Chen

Quintana Roo, Mexico infers connection with the aquifer and response to Holocene sea-level rise and Classic Maya droughts. *Journal of Paleolimnology*, *62*(4), 373–388. https://doi.org/10.1007/s10933-019-00094-0

Logan, B. W. (1961). Cryptozoon and Associate Stromatolites from the Recent, Shark Bay, Western Australia. *The Journal of Geology, 69*(5). https://doi.org/10.1086/626769

López-Martínez, R., Gázquez, F., Calaforra, J., Audra, P., Bigot, J., Pi Puig, T., Alcántara-Hernández, R., Navarro, Á., Crochet, P., Corona Martínez, L., & Daza Brunet, R. (2020). Bubble trail and folia in cenote Zapote, Mexico: petrographic evidence for abiotic precipitation driven by CO2 degassing below the water table. *International Journal of Speleology*, *49*(3), 173–186. https://doi.org/10.5038/1827-806X.49.3.2344

Lucia, J.F, (2017). Observations on the origin of micrite crystals. *Marine and Petroleum Geology, 86*, 823 – 833. https://doi.org/10.1016/j.marpetgeo.2017.06.039

Lyons, T. W., Reinhard, C. T., & Planavsky, N. J. (2014). The rise of oxygen in Earth's early ocean and atmosphere. *Nature, 506* (7488), 307–315. https://doi.org/10.1038/nature13068

Mann, C. J., & Nelson, W. M. (1989). Microbialitic Structures in Storr's Lake, San Salvador Island, Bahama Islands, PALAIOS, 4(3), 287–293. https://doi.org/10.2307/3514777

McNeill-Jewer, C. A., Reinhardt, E. G., Collins, S., Kovacs, S., Chan, W. M., Devos, F., & LeMaillot, C. (2019). The effect of seasonal rainfall on nutrient input and biological productivity in the Yax Chen cave system (Ox Bel Ha), Mexico, and implications for µXRF core studies of paleohydrology. *Palaeogeography, Palaeoclimatology, Palaeoecology*, *534*(4). https://doi.org/10.1016/j.palaeo.2019.109289

Medina-Elizalde, M, Burns, Polanco-Martínez, J.M, Beach T, Lases-Hernández, Shen, C, Wang, H (2016) High-resolution speleothem record of precipitation from the Yucatan Peninsula spanning the Maya Preclassic Period. *Global and Planetary Change*, *138*, 93-102

Mushet, Graham., (2014) "Determining the influence of paleo water tables on speleothem formation, Ich Balam, Mexico" [Bachelor's thesis, McMaster University].

Nutman, A. P., Bennett, V. C., Friend, C. R. L., Van Kranendonk, M. J., & Chivas, A. R. (2016). Rapid emergence of life shown by discovery of 3,700-million-year-old microbial structures. *Nature*, *537*(7621), 535–538. https://doi.org/10.1038/nature19355

O'Leary, M. H. (1988). Carbon Isotopes in Photosynthesis *BioScience*,*38*(5), 328–336. https://doi.org/10.2307/1310735.

Omelon, C. R., Brady, A. L., Slater, G. F., Laval, B., Lim, D. S. S., & Southam, G. (2013). Microstructure variability in freshwater microbialites, Pavilion Lake, Canada. *Palaeogeography, Palaeoclimatology, Palaeoecology*, *392*, 62–70. https://doi.org/10.1016/j.palaeo.2013.08.017

Paul, V. G., Wronkiewicz, D. J., Mormile, M. R., & Foster, J. S. (2016). Mineralogy and microbial diversity of the microbialites in the Hypersaline Storr's Lake, the Bahamas. *Astrobiology*, *16*(4), 282–300. https://doi.org/10.1089/ast.2015.1326

Paytan, A., Velazquez-Oliman, G., Perry, E., 2004. Unpublished strontium isotope analyses.

Perry, E., Marín, L. E., McClain, J., & Velázquez, G. (1995). Ring of cenotes (sinkholes), Northwest Yucatan, Mexico; its hydrogeologic characteristics and possible association with the Chicxulub impact crater. *Geology (Boulder)*, *23*(1), 17–20. https://doi.org/10.1130/0091-7613(1995)023<0017:ROCSNY>2.3.CO;2

Perry, E., Paytan, A., Pedersen, B., & Velazquez-Oliman, G. (2009). Groundwater geochemistry of the Yucatan Peninsula, Mexico: Constraints on stratigraphy and hydrogeology. *Journal of Hydrology*, *367*(1–2), 27–40. https://doi.org/10.1016/j.jhydrol.2008.12.026

Perry, E., Velazquez-Oliman, G., & Marin, L. (2002). The hydrogeochemistry of the karst aquifer system of the northern Yucatan peninsula, Mexico. *International Geology Review*, *44*(3), 191–221. https://doi.org/10.2747/0020-6814.44.3.191

Quintana Roo Speleological Society (QRSS) (1 August 2023) List of long underwater caves in Quintana Roo, Mexico [Online]. Available: http://www.caves.org/project/qrss/qrlong.htm [Accessed online 1 Aug 2023]

Reid, R. P., Visscher, P. T., Decho, A. W., Stolz, J. F., Beboutk, B. M., Dupraz, C., Macintyre, I. G., Paerl, H. W., Pinckney, J. L., Prufert-Beboutk, L., Steppe, T. F., & Desmaraisk, D. J. (2000). The role of microbes in accretion, lamination and early lithification of modern marine stromatolites. *Nature 406*(6799), 989–992. doi:10.1038/35023158

Ritter, S. M., Isenbeck-Schröter, M., Scholz, C., Keppler, F., Gescher, J., Klose, L., Schorndorf, N., Avilés Olguín, J., González-González, A., & Stinnesbeck, W. (2019). Subaqueous speleothems (Hells Bells) formed by the interplay of pelagic redoxcline biogeochemistry and specific hydraulic conditions in the El Zapote sinkhole, Yucatán Peninsula, Mexico. *Biogeosciences*, *16*(11), 2285–2305. https://doi.org/10.5194/bg-16-2285-2019

Rusznyák, Anna, et al. Calcite Biomineralization by Bacterial Isolates from the Recently Discovered Pristine Karstic Herrenberg Cave. *Applied and Environmental Microbiology,78*(4), 1157–1167. https://doi.org/10.1128/aem.06568-11.

Schmitz, K.S. (2017). Thermodynamics of the liquid state. In Physical Chemistry. Elsevier Inc. (pp. 203–260). https://doi.org/10.1002/9781444361094.ch1

Schorndorf, N., Frank, N., Ritter, S. M., Warken, S. F., Keppler, F., Scholz, D., Weber, M., Aviles Olguin, J., & Stinnesbeck, W. (n.d.). Holocene sea-level rise evidenced in Hells Bells U/ 238 U ratio and geochemical composition.

Schultze-Lam, S., Fortin, D., Davis, B. S., & Beveridge, T. J. (1996). Mineralization of bacterial surfaces. *Chemical Geology*,*132*(1–4), 171 –181. *https://doi.org/10.1016/S0009-2541(96)00053-*

Smart, P. L., Beddows, P. A., Coke, J., Doerr, S., Smith, S., & Whitaker, F. F. (2006). Cave development on the Caribbean coast of the Yucatan Peninsula, Quintana Roo, Mexico. *Special Paper of the Geological Society of America*, *404*, 105–128. https://doi.org/10.1130/2006.2404(10)

Steele, R. E., Reinhardt, E. G., Devos, F., Meacham, S., LeMaillot, C., Gabriel, J. J., Rissolo, D., Vera, C. A., Peros, M. C., Kim, S. T., Marshall, M., & Zhu, J. (2023). Evidence of recent sea-level rise and the formation of a classic Maya canal system inferred from Boca Paila cave sediments, Sian Ka'an biosphere, Mexico. *Quaternary Science Reviews*, *310*. https://doi.org/10.1016/j.quascirev.2023.108117

Steinich, B., & Marín, L. E. (1997). Determination of flow characteristics in the aquifer of the Northwestern Peninsula of Yucatan, Mexico. *Journal of Hydrology (Amsterdam)*, *191*(1), 315–331. https://doi.org/10.1016/S0022-1694(96)03038-7

Stinnesbeck, W., Frey, E., Zell, P., Avilés, J., Hering, F., Frank, N., Arps, J., Geenen, A., Gescher, J., Isenbeck-Schröter, M., Ritter, S., Stinnesbeck, S., Núñez, E. A., Dahne, V. F., González, A. G., & Deininger, M. (2018). Hells Bells – unique speleothems from the Yucatán Peninsula, Mexico, generated under highly specific subaquatic conditions. *Palaeogeography, Palaeoclimatology, Palaeoecology*, *489*, 209–229. https://doi.org/10.1016/j.palaeo.2017.10.012

Stoessell, R. K., Ward, W. C., Ford, B. H., & Schuffert, J. D. (1989). Water chemistry and CaCO3 dissolution in the saline part of an open-flow mixing zone, coastal Yucatan Peninsula, Mexico. *Geological Society of America Bulletin*, *101*(2), 159–169. https://doi.org/10.1130/0016-7606(1989)101<0159:WCACDI>2.3.CO;2

Taylor, M. P., Dry1σale, R. N., & Carthew, K. D. (2004). The formation and environmental significance of calcite rafts in tropical tufa-depositing rivers of northern Australia. *Sedimentology*, *51*(5), 1089–1101. https://doi.org/10.1111/j.1365-3091.2004.00661.x

Tice, M. M., Quezergue, K., & Pope, M. C. (2017). Microbialite Biosignature Analysis by Mesoscale X-ray Fluorescence (μXRF) Mapping. *Astrobiology*, *17*(11), 1161–1172. https://doi.org/10.1089/ast.2016.1494

Valdespino-Castillo, P. M., Hu, P., Merino-Ibarra, M., López-Gómez, L. M., Cerqueda-García, D., González-De Zayas, R., Pi-Puig, T., Lestayo, J. A., Holman, H.-Y., & Falcón, L. I. (2018). Exploring Biogeochemistry and Microbial Diversity of Extant Microbialites in Mexico and Cuba. *Frontiers in Microbiology*, *9*, 510–510. https://doi.org/10.3389/fmicb.2018.00510

van Hengstum, P. J., Reinhardt, E. G., Beddows, P. A., & Gabriel, J. J. (2010). Linkages between Holocene paleoclimate and paleohydrogeology preserved in a Yucatan underwater cave. *Quaternary Science Reviews*, *29*(19–20), 2788–2798. https://doi.org/10.1016/j.quascirev.2010.06.034

Van Hengstum Peter J., Reinhardt Eduard G., Beddows, P. A., Schwarcz, H. P., & Gabriel, J. J. (2009). Foraminifera and testate amoebae (thecamoebians) in an anchialine cave: Surface distributions from Aktun Ha (Carwash) cave system, Mexico. *Limnology Oceanography*, *54*(1), 391–396. doi:10.4319/lo.2009.54.1.0391

Van Hengstum, P. J., Reinhardt, E. G., Beddows, P. A., Huang, R. J., & Gabriel, J. J. (2008). The Camoebians (Testate Amobeobae) and Foraminifera from three Anchialine Cenotes in Mexico: Low Salinity (1.5-4.5 psu) Faunal Transitions. *Journal of Foraminferal Research*, *38*(4), 305–317. doi:10.2113/gsjfr.38.4.305

Vázquez-Domínguez, E., & Arita, H. T. (2010). Yucatan peninsula: biogeographical history 65 million years in the making [Article]. *Ecography (Copenhagen)*, *33*(2), 212–219. https://doi.org/10.1111/j.1600-0587.2009.06293.x

Visscher, P. T, Reid, P, Bebout, B.M. (2000) Microscale observations of sulfate reduction: Correlation of microbial activity with lithified micritic laminae in modern marine stromatolites. *Geology, 28* (10): 919–922. https://doi.org/10.1130/0091-7613(2000)28<919:MOOSRC>2.0.CO;2

Visscher, P. T., Reid, R. P., Bebout, B. M., Hoeft, S. E., Macintyre, I. G., & Thompson, J. A. (1998). Formation of lithified micritic laminae in modern marine stromatolites (Bahamas): The role of sulfur cycling. *American Mineralogist, 83*(11–12), 1482–1493 http://pubs.geoscienceworld.org/msa/ammin/article-pdf/83/11-12_Part_2/1482/3613574/1482.pdf

Walter, M. R., & Heys, G. R. (1985). Between the Rise of the Metazoa and the decline of Stromatolites. *Precambrian Research, 29* (1–3), 149–174. doi 10.1016/0301-9268(85)90066-X

Ward W.C., Weidie A.E., & Back W. (1985). *Geology and Hydrogeology of the Yucatan and Quaternary Geology of the Northeastern Yucatan Peninsula*. New Orleans Geological Society.

Wróblewski, W., Gradziński, M., Motyka, J., & Stankovič, J. (2017). Recently growing subaqueous flowstones: Occurrence, petrography, and growth conditions. *Quaternary International*, *437*, 84–97. https://doi.org/10.1016/j.quaint.2016.10.006

Yanez-Montalvo, A., Águila, B., Gómez-Acata, S., Mass-Vargas, M., Cabanillas-Terán, N., Vega-Zepeda, A., Bahena, H., Hernández-Arana, H., & Falcón, L. I. (2021). Depth related structure and microbial composition of microbialites in a karst sinkhole, Cenote Azul, Mexico. *Geomicrobiology Journal*, *38*(3), 237–251. https://doi.org/10.1080/01490451.2020.1836086

Yanez-Montalvo, A., Gómez-Acata, S., Águila, B., Hernández-Arana, H., & Falcón, L. I. (2020). The microbiome of modern microbialites in Bacalar Lagoon, Mexico. *PloS One*, *15*(3) https://doi.org/10.1371/journal.pone.0230071

List of Figures.

Figure 5. Cross section of Hoyo Negro and Ich Balam from Kovacs et al., (2017). Calcite raft core locations are also shown along with samples HN1A and HN2A.

Figure 6. Water profiles of Cenote Fatima. Green arrows show sample locations for CF1A, CF2A, and CF3A.

Figure 7. Water profiles for Hoyo Negro. Blue arrows represent where samples HN1A and HN2A were taken.

Figure 8. Images showing exterior and interior section of each sample. White rectangles show where the samples were drilled. For a more detail on the sampling see Supplementary Figures 1-9. T is the top of the sample with respect to how it was found; G is assumed growth direction. A) HN1A interior showing crystal branches. B) HN1A image showing smooth lobes. C)HN2A a cross section of a stalagmite. D) Cross section of LC1A showing the central soda straw formation and small branches radiating outwards. E) LC1A showing elongated lobes branching outwards. F) LC2A cross section showing distinct layering. G) LC2A showing a bulbous surface. H) XH1A cross section showing a distinct layering curvature is from growing alongside a log. I) XH1A showing greenish tinge and globular appearance. J) XH2A cross section showing a thrombolytic structure. K) XH2A showing green tinge to outer layers.

Figure 9. Images showing exterior and interior section of sample. White rectangles are where the samples were drilled. For a more detail on sampling see Supplementary Figures 1-9. T is the top of the sample with respect to how it was found; G is assumed growth direction. A) CF2A cross section white inner core is composed of a mixture of calcite and dolomite. B) CF2A showing elongated lobes. C)CF1A cross section white inner core is composed of calcite and

dolomite D) CF1A showing elongated lobes. E) CF3A cross section showing no growth lines present F) CF3A showing branched lobes.

Figure 10. Thin sections. White boxes show where growth lines are found. A) PPL (Plane Polarized Light) image of HN1A showing crystalline structure. B) XPL (Cross Polarized Light) image of HN1A showing crystalline structure. C) PPL image of CF1A; large gaps show porous structure. D) XPL image of CF1A showing porous structure; growth rings can be observed near the top. E) PPL image of CF2A. F) XPL image of CF2A; in both PPL and XPL large gaps are where drilling occurred. Growth rings can be seen near the top of the section in XPL. G) PPL image for XH1A. H) XPL image of XH1A; large gaps are where drilling occurred for both PPL and XPL. Growth rings can be seen near the top of the section in XPL. I) PPL image of XH2A. J) XPL image of XH2A; large gaps show the porous structure in both XPL and PPL.

Figure 11. Crossplot of $\delta^{13}C$ and $\delta^{18}O$ for all locations. Trendlines are shown for Cenote Fatima samples and La Concha. Dolomite/calcite samples CF1A and CF2A are included.

Figure 12. Crossplot of Mg/Ca with Sr/Ca for all Yucatan locations. Trendlines are shown for Cenote Fatima, La Concha and Hoyo Negro samples. Inner dolomtie/calcite samples were not included for CF1A and CF2A.

Figure 13. Crossplot of S/Ca verus Sr/Ca for all locations. Trendline is shown for Xul Ha Cenote samples. Inner dolotmite/calcite samples were not included for CF1A and CF2A.

Figure 14. Sr/Ca Crossplot of ICP-OES verus XRF for HN1A, CF1A, CF2A and XH1A.

Figure 15. S/Ca Crossplot of ICP-OES verus XRF for HN1A, CF1A, CF2A, and XH1A.

Figure 16. Sr/Ca and S/Ca XRF total counts for samples HN1, CF1, CF2, and XH1. Scale in cm is shown above the top graph. Dashed lines shows a trend where applicable. Arrows show the transition of the outer layer to the core for CF samples. For XH samples, arrows show peaks in the data.

Figure 17. Crossplot of $^{87}Sr/^{86}Sr$ and Sr/Ca for CF2A, XH1A; and all samples from Hoyo Negro, and La Concha. Inner core samples for CF1A and CF2A were not included.

Figure 18. A) Oxcal calibrated curve for CF2A and B) Oxcal calibrated curve for CF3A Bronk Ramsey (2021). Atmospheric data from Reimer et al., 2020.

Figure 19. Crossplot of Mg/Ca ICP-OES and $\delta^{13}C$ for all locations. Trendline with Cenote Fatima samples and Hoyo Negro samples is shown. Dolomite/calcite values for CF1A and CF2A were not included.

Figure 20. Crossplot of S/Ca ICP-OES and $\delta^{13}C$ with Cenote Fatima trend. Dolomite/calcite values for CF1A and CF2A were not included.

Figure 21. Crossplot Sr/Ca ICP-OES and $\delta^{13}C$. Cenote Fatima trend is shown and dolomite/calcite values for CF1A and CF2A were not included.

Figure 22. Crossplot of average $\delta^{13}C$ and $\delta^{18}O$ values for all samples exluding dolomite/calcite samples from CF1A and CF2A and values from outer edge for all samples were also excluded. Average values from published results are also shown (Ritter et al., 2019, Kovacs et al., 2017, Castro-Contreras et al., 2014, Brady et al., 2014; 2010, Mushet, 2014 and Schorndorf et al., n.d).

Figure 23. Sr/Ca verus δ ^{13}C average values for all locations and compared with calcite raft cores (Kovacs et al., 2017), Laguan Bacalar (Castro-Contreras et al., 2014), and Hells Bells (Ritter et al., 2019) are also included.

Figure 24. $^{87}Sr/^{86}Sr$ with $\delta^{13}C$. $^{87}Sr/^{86}Sr$ values for seawater are from Kovacs et al., (2017). $\delta^{13}C$ for surface seawater 2.0‰ from Kroopnick, (1984). $^{87}Sr/^{86}Sr$ and $\delta^{13}C$ values for calcite raft cores are from Kovacs et al., (2017) Speleothem $^{87}Sr/^{86}Sr$ and $\delta^{13}C$ values were from Mushet, (2014).

Figure 25. Water level changes for Cenote Fatima. WL is Water Level. A) Comparison of present and ≈7600 cal. yr. BP water level for Cenote Fatima using Kovacs et al., (2017) sea level curve and cave specific water level data for estimating water depth at ≈7600 cal. yr. BP. B) Comparison of present and ≈9000 cal. yr. BP water level using Kovacs et al., (2017). A table shows with calcite raft core values from Kovacs et al., (2017) of calcite raft cores from Ich Balam, Hoyo Negro along with CF2A (exluding interior) and CF3A showing comparison between $\delta^{13}C$, . $\delta^{18}O$, Sr/Ca, and $^{87}Sr/^{86}Sr$.

Supplementary Table 1. Radiocarbon data. Calibrated data is from Kovacs et al., (2017)-1267 cal yr. hardwater reseverior correction.

Supplementary Figure 1. XH1A -Geochemical Data. Drilled section was 3-5 mm in length. δ ^{13}C and $\delta^{18}O$ values are in per mil ‰.

Supplementary Figure 2. XH2A – Geochemical Data. Drilled section was 5-10 mm in length. $\delta^{13}C$ and $\delta^{18}O$ values are in per mil ‰.

Supplementary Figure 3. CF1A-Geochemical Data. Drilled sections were 1-3 mm in length. $\delta^{13}C$ and $\delta^{18}O$ values are in per mil ‰.

Supplementary Figure 4. CF2A-Geochemical Data. Drilled sections were 1-3 mm in length. $\delta^{13}C$ and $\delta^{18}O$ values are in per mil ‰.

Supplementary Figure 5. CF3A – Geochemcial Data. Drilled sections were 8-10 mm in length. $\delta^{13}C$ and $\delta^{18}O$ values are in per mil ‰.

Supplementary Figure 6. HN1A-Geochemical Data. Drilled sections were 1-3 mm in length and $\delta^{13}C$ and $\delta^{18}O$.

Supplementary Figure 7. HN2A-Geochemical Data. Drilled sections were 3-5 mm in length. $\delta^{13}C$ and $\delta^{18}O$ values are in per mil ‰.

Supplementary Figure 8. LC1A – Geochemical Data. Drilled section was 1-3 mm in length. $\delta^{13}C$ and $\delta^{18}O$ values in per mil ‰.

Supplementary Figure 9. LC2A – Geochemical Data. Drilled section was 1-3 mm in length. $\delta^{13}C$ and $\delta^{18}O$ values in per mil ‰.

Supplementary Table 1. Geochemical Data. Values were rounded to two decimal places.

Supplementary Figure 10. XRD phase identificiation for HN1A.

Supplementary Figure 11. XRD phase identification for HN2A.

Supplementary Figure 12. XRD phase identification for XH1A and XH2A.

Supplementary Figure 13. XRD phase identification for CF1A and CF2A.

Supplementary Figure 14. XRD phase identification for CF3A, LC1A and LC2A.

Figure 1.

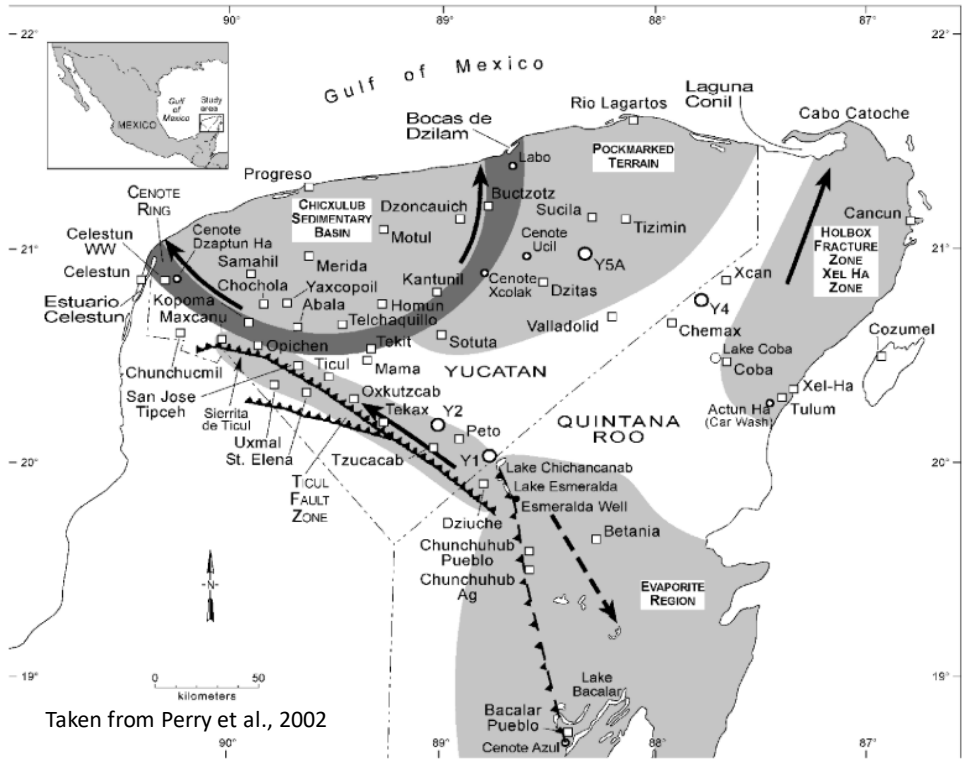

Taken from Perry et al., 2002

Figure 2.

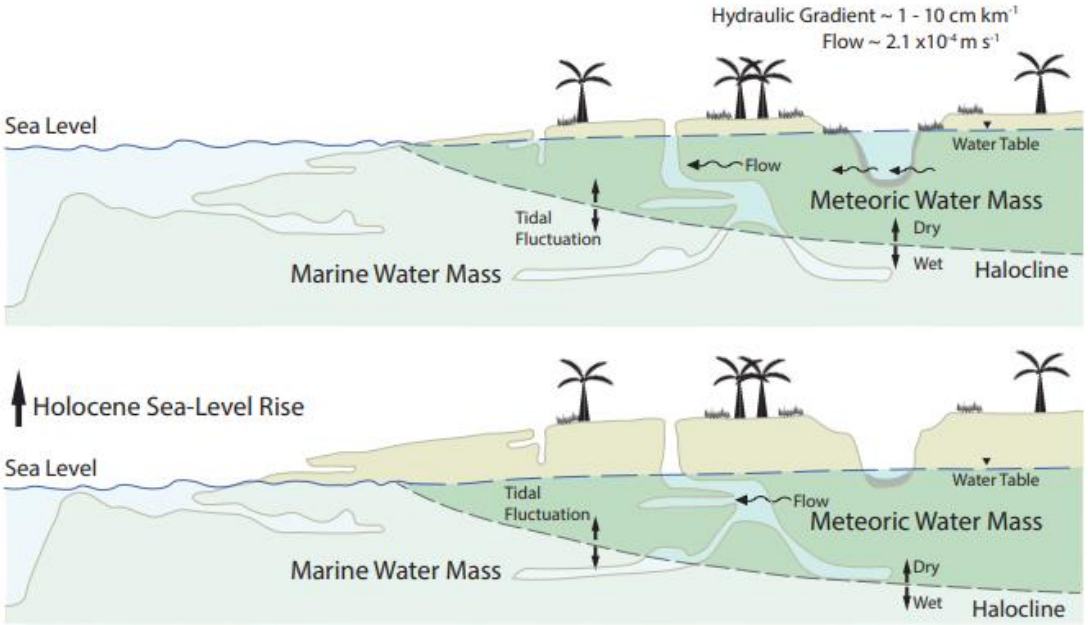

Figure 3.

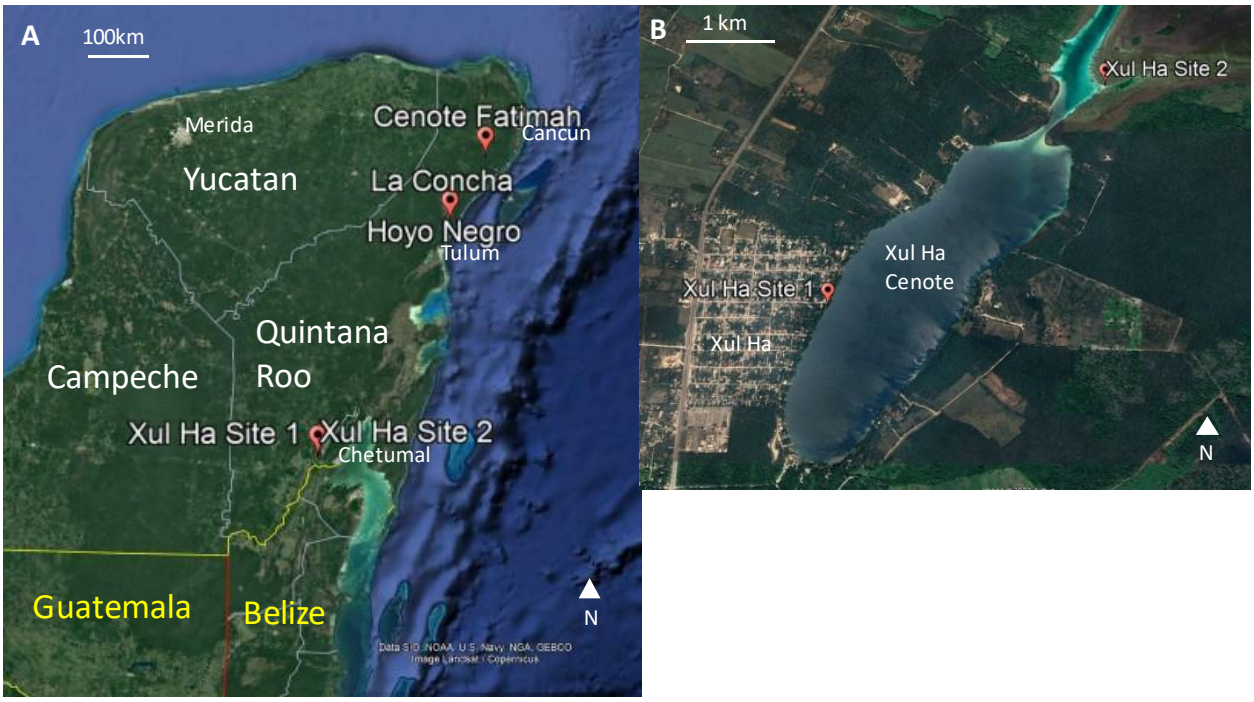
A
100km
Merida
Cenote Fatimah
Cancun
Yucatan
La Concha
Hoyo Negro
Tulum
Quintana
Roo
Campeche
Xul Ha Site 1
Xul Ha Site 2
Chetumal
Guatemala
Belize
N
B
1 km
Xul Ha Site 2
Xul Ha
Cenote
Xul Ha Site 1
Xul Ha
N

Figure 4.

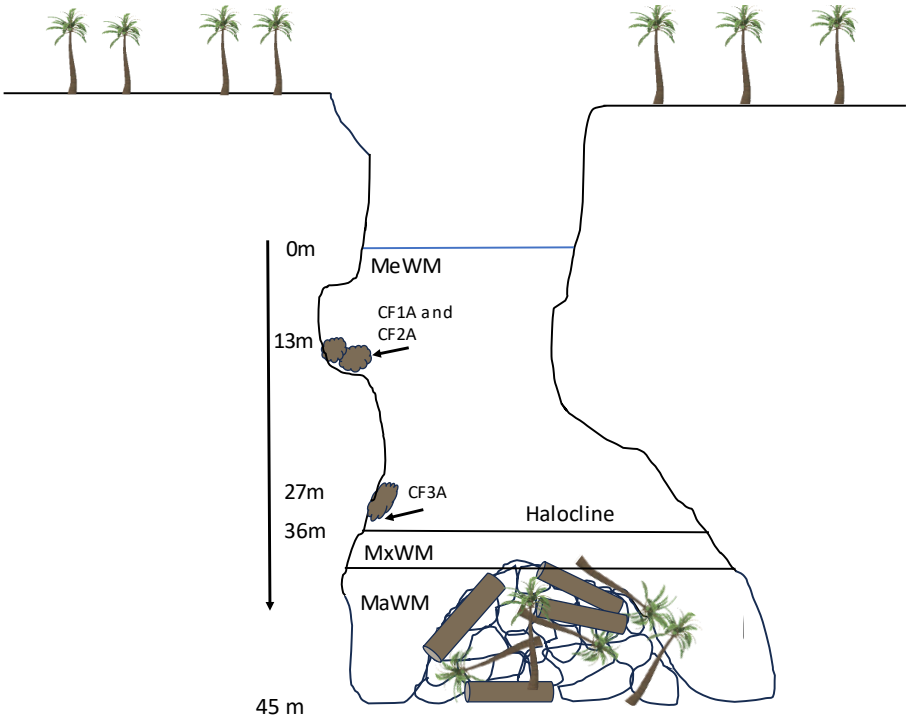

Figure 5.

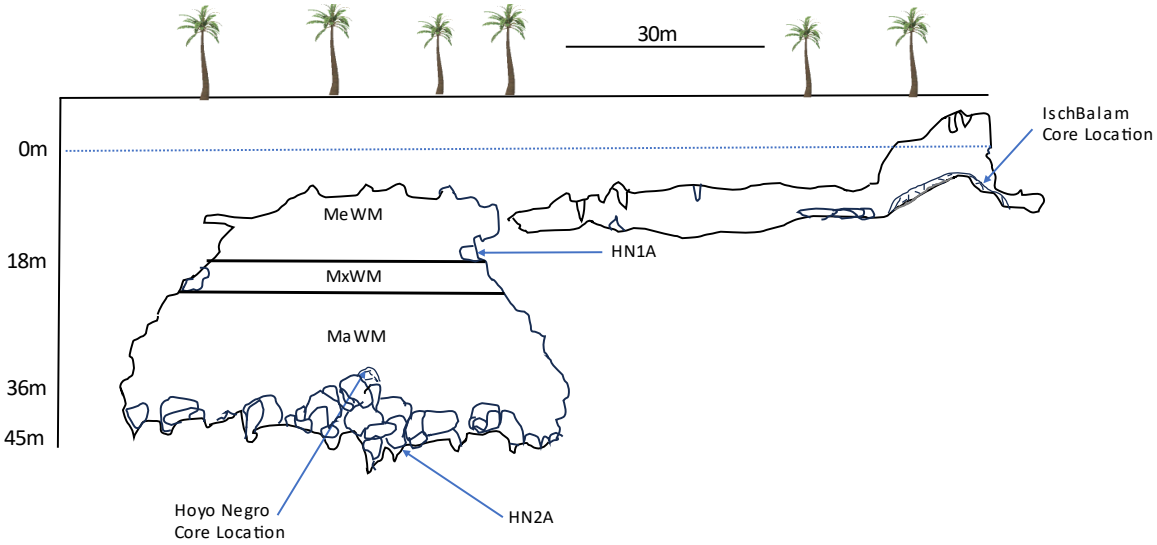

Figure 6.

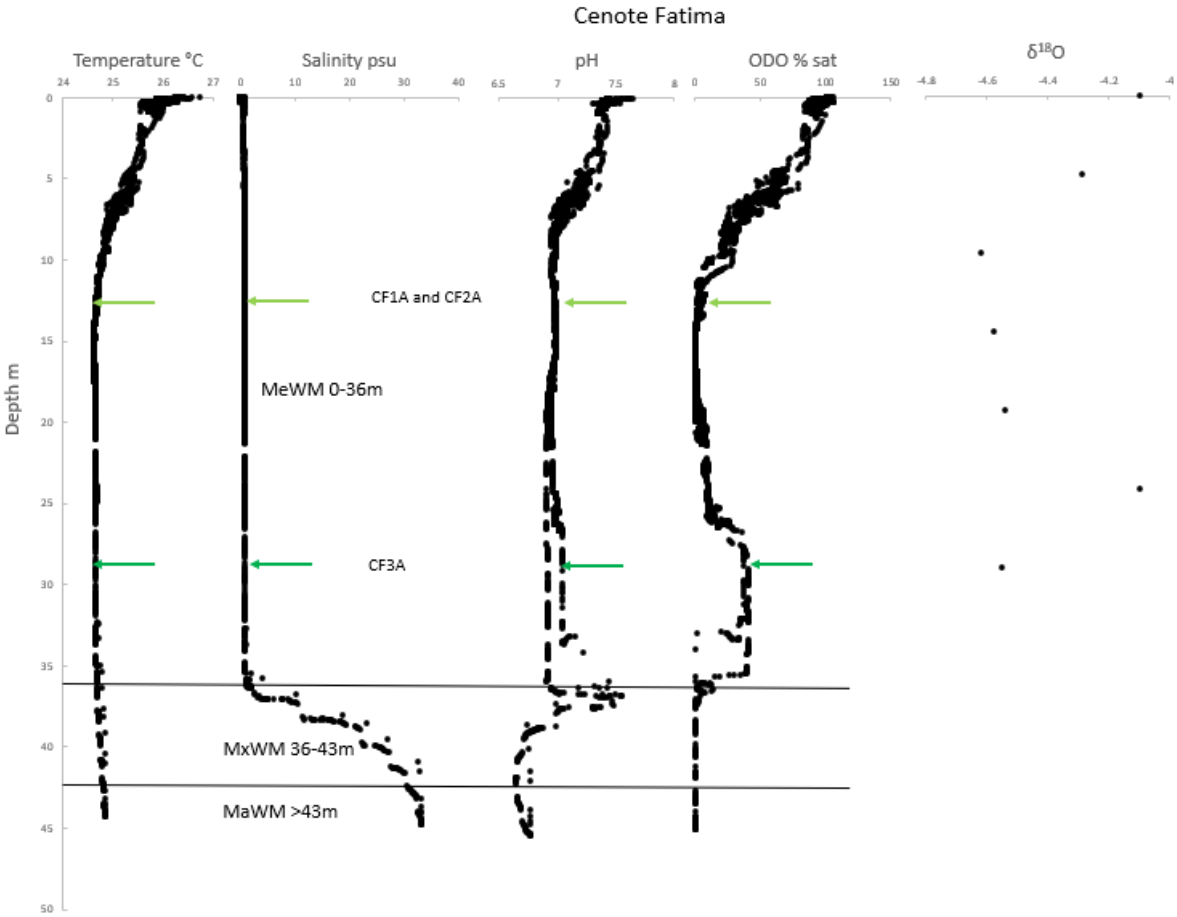
Cenote Fatima
Temperature °C
Salinity psu
pH
ODO % sat
δ18O
Depth m
CF1A and CF2A
MeWM 0-36m
CF3A
MxWM 36-43m
MaWM >43m

Figure 7.

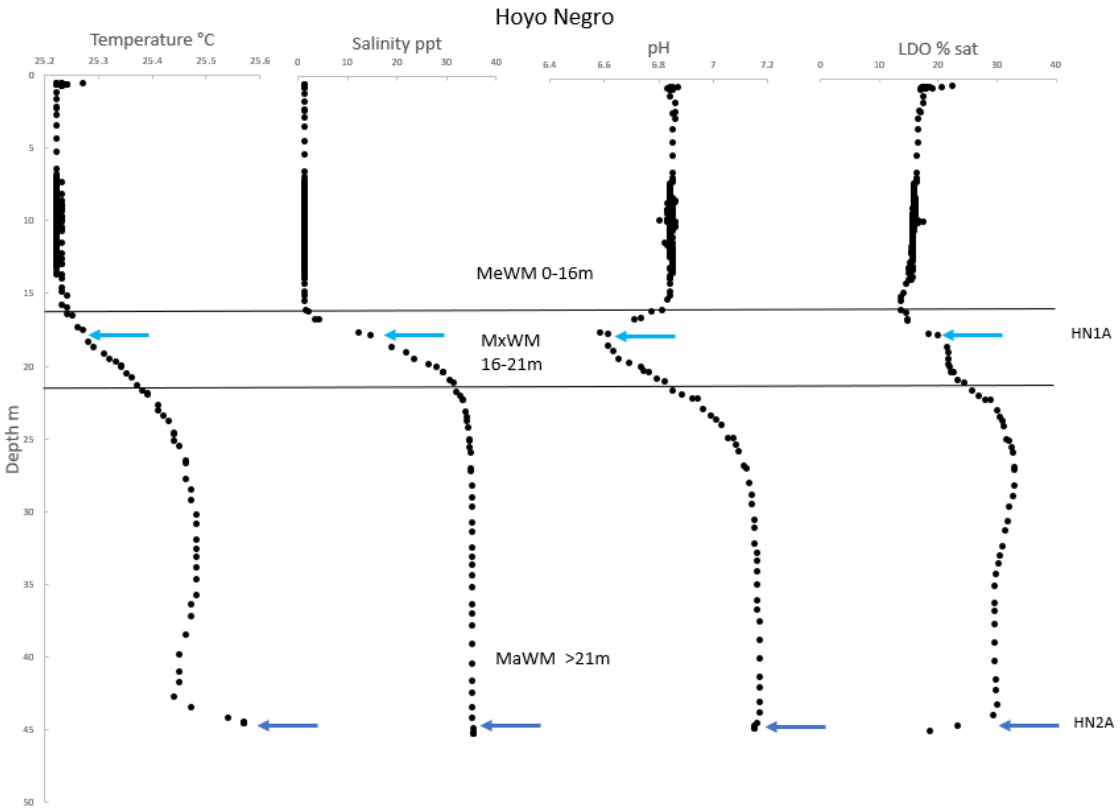
Hoyo Negro
Temperature °C
Salinity ppt
pH
LDO % sat
Depth m
MeWM 0-16m
MxWM
16-21m
MaWM >21m
HN1A
HN2A

Figure 8.

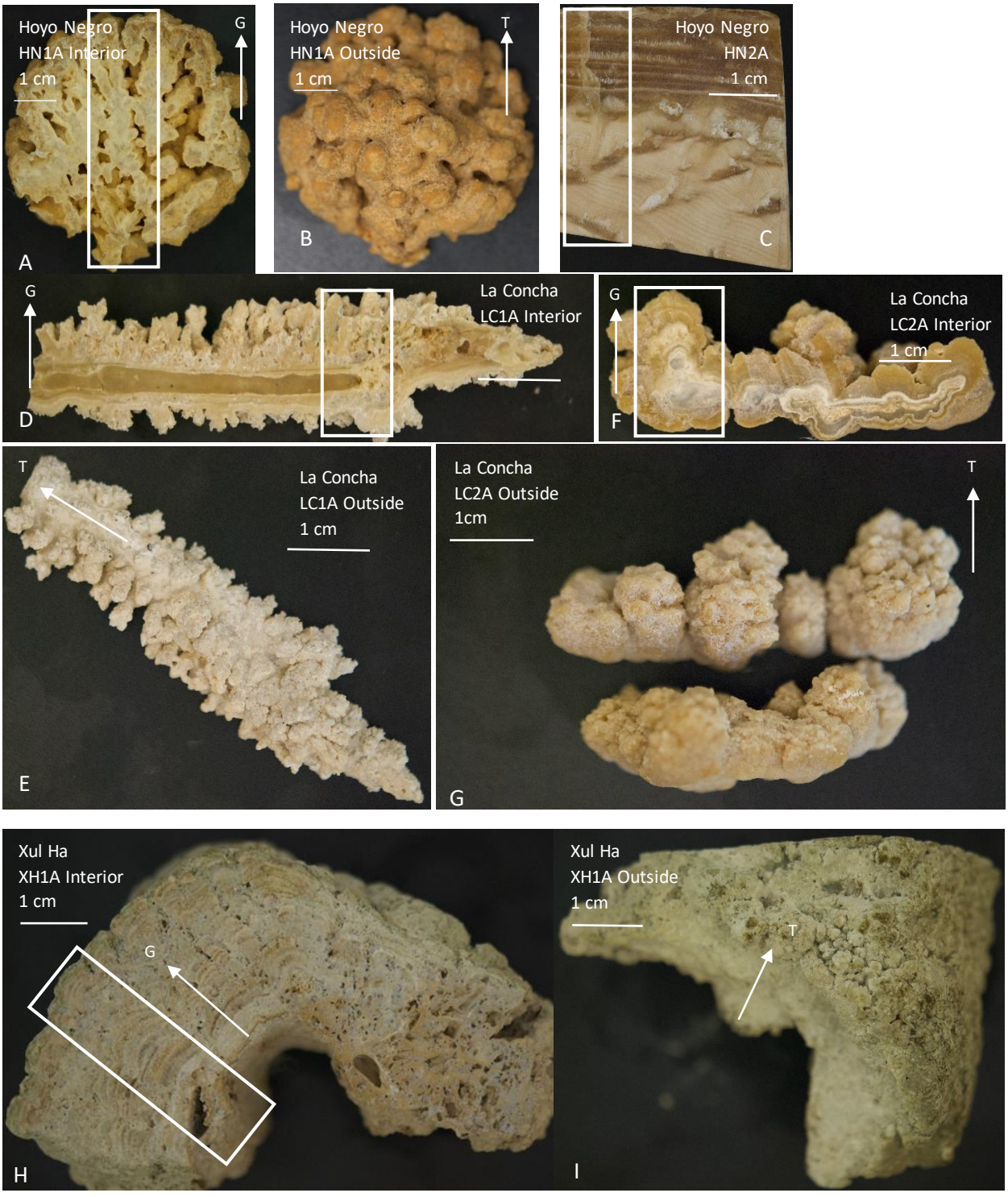
Hoyo Negro
HN1A Interior
1 cm
G
A
Hoyo Negro
HN1A Outside
1 cm
T
B
Hoyo Negro
HN2A
1 cm
C
G
La Concha
LC1A Interior
D
G
La Concha
LC2A Interior
1 cm
F
T
La Concha
LC1A Outside
1 cm
E
La Concha
LC2A Outside
1cm
T
G
Xul Ha
XH1A Interior
1 cm
G
H
Xul Ha
XH1A Outside
1 cm
T
I

Figure 9

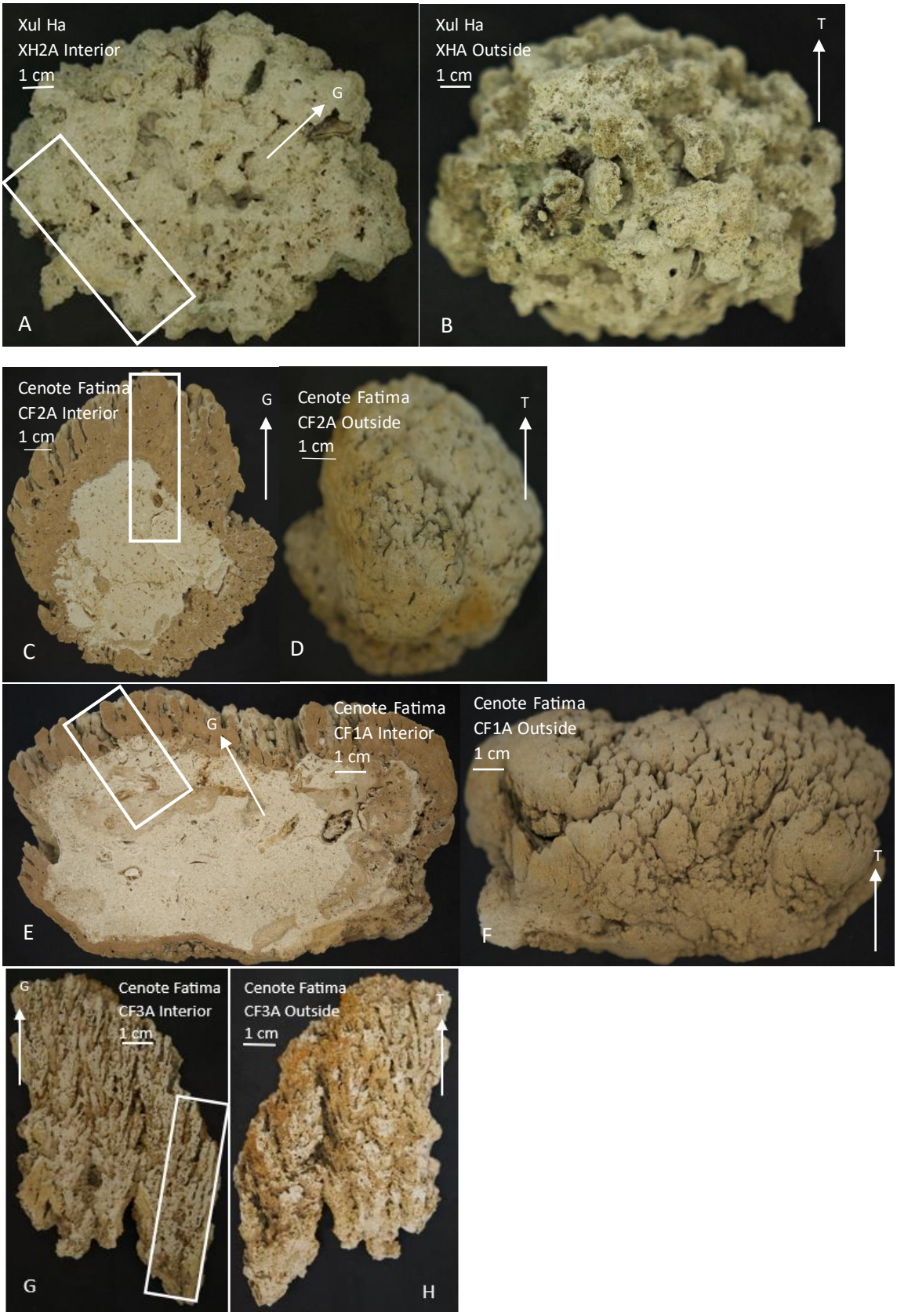
Xul Ha
XH2A Interior
1 cm
G
A
Xul Ha
XHA Outside
1 cm
T
B
Cenote Fatima
CF2A Interior
1 cm
G
C
Cenote Fatima
CF2A Outside
1 cm
T
D
G
Cenote Fatima
CF1A Interior
1 cm
E
Cenote Fatima
CF1A Outside
1 cm
T
F
G
Cenote Fatima
CF3A Interior
1 cm
G
Cenote Fatima
CF3A Outside
1 cm
T
H

Figure 10.

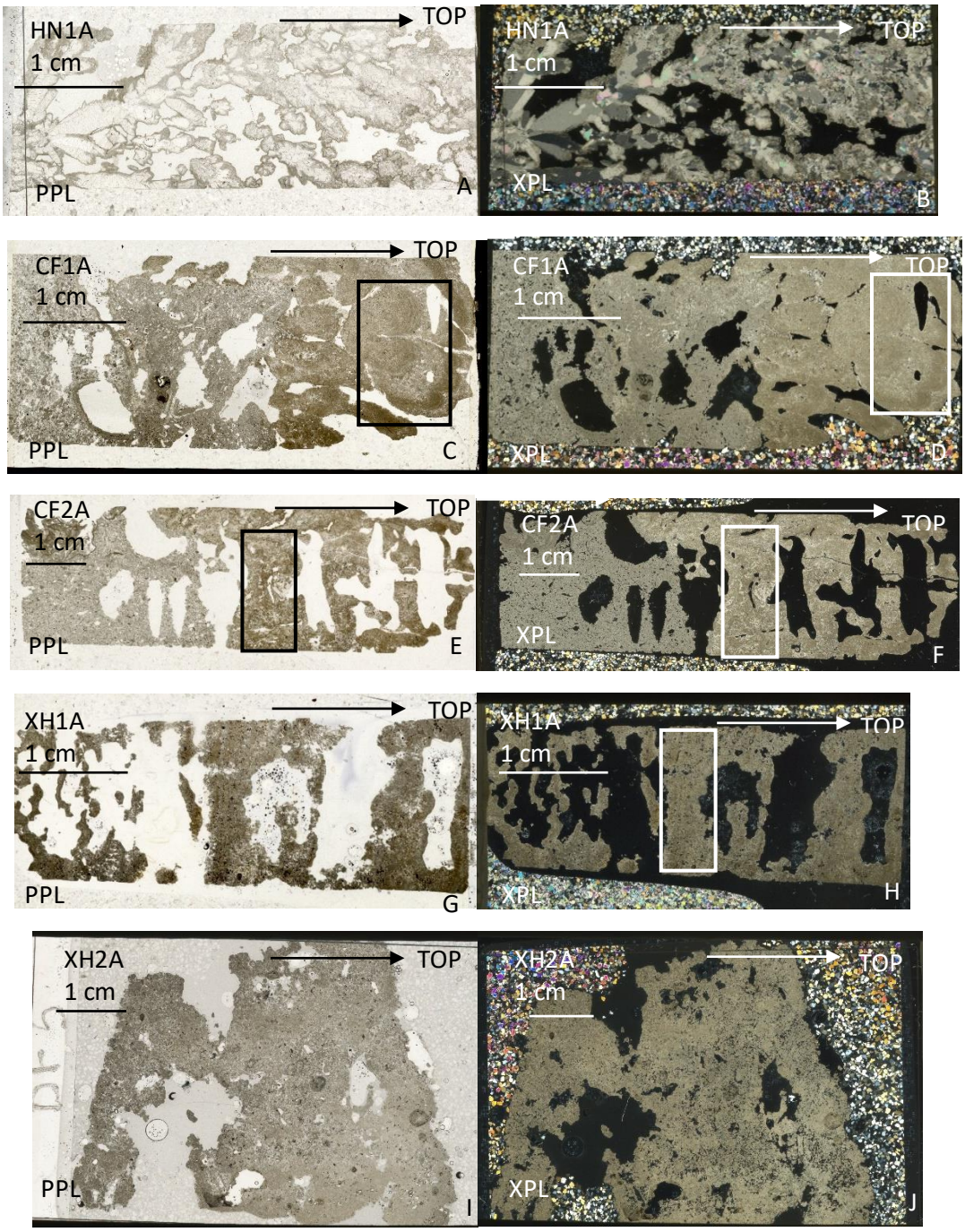
HN1A
1 cm
TOP
PPL
A
HN1A
1 cm
TOP
XPL
B
CF1A
1 cm
TOP
PPL
C
CF1A
1 cm
TOP
XPL
D
CF2A
1 cm
TOP
PPL
E
CF2A
1 cm
TOP
XPL
F
XH1A
1 cm
TOP
PPL
G
XH1A
1 cm
TOP
XPL
H
XH2A
1 cm
TOP
PPL
I
XH2A
1 cm
TOP
XPL
J

Figure 11.

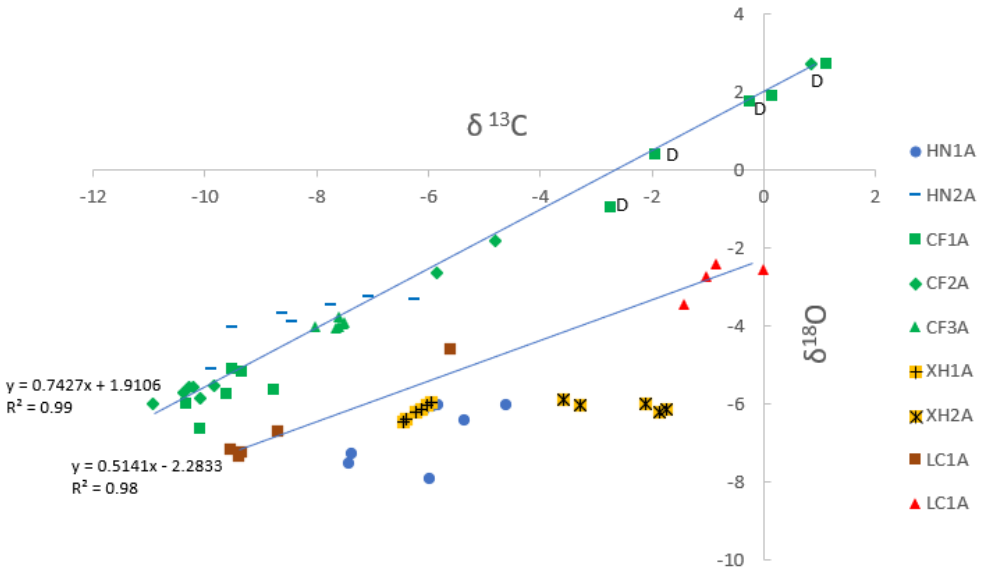
δ 13C
δ18O
y = 0.7427x + 1.9106
R² = 0.99
y = 0.5141x - 2.2833
R² = 0.98
D
HN1A
HN2A
CF1A
CF2A
CF3A
XH1A
XH2A
LC1A
LC1A

Figure 12.

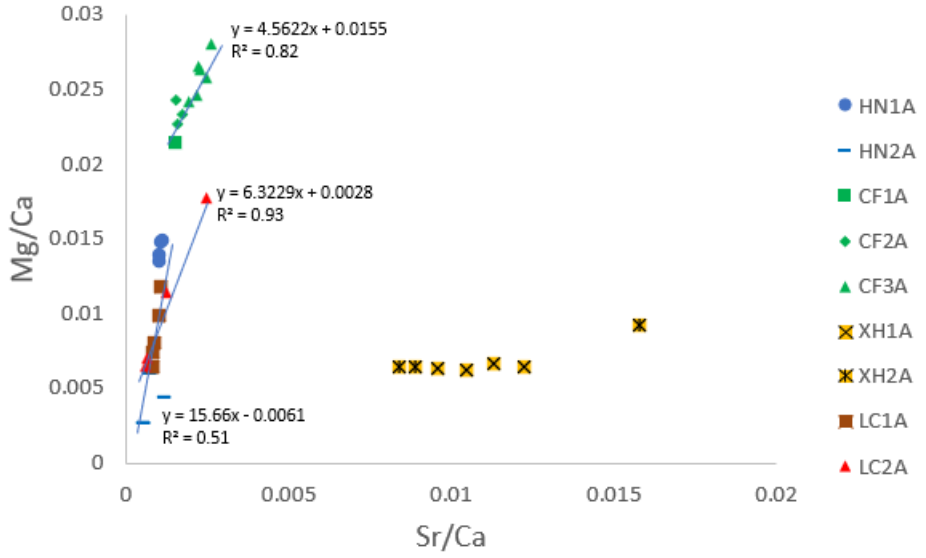

Figure 13.

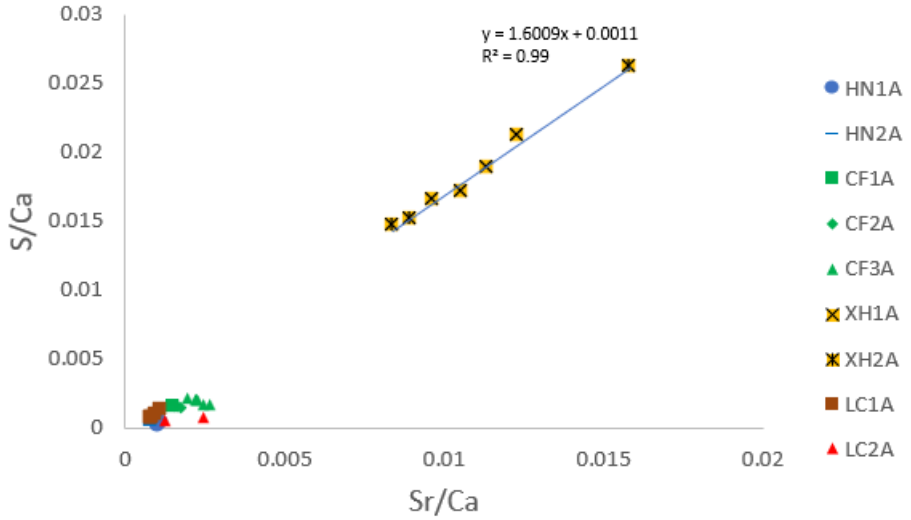

Figure 14.

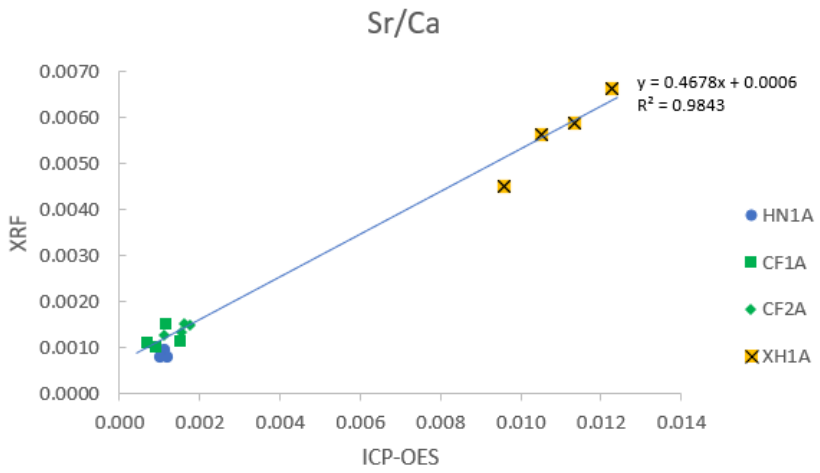

Figure 15.

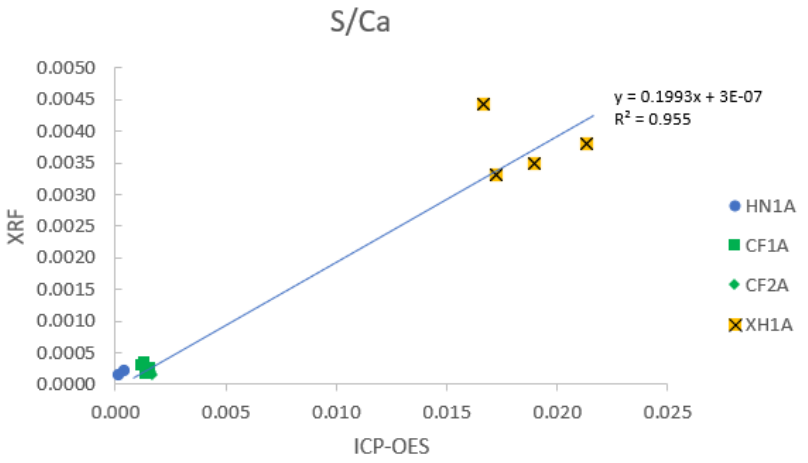

Figure 16.

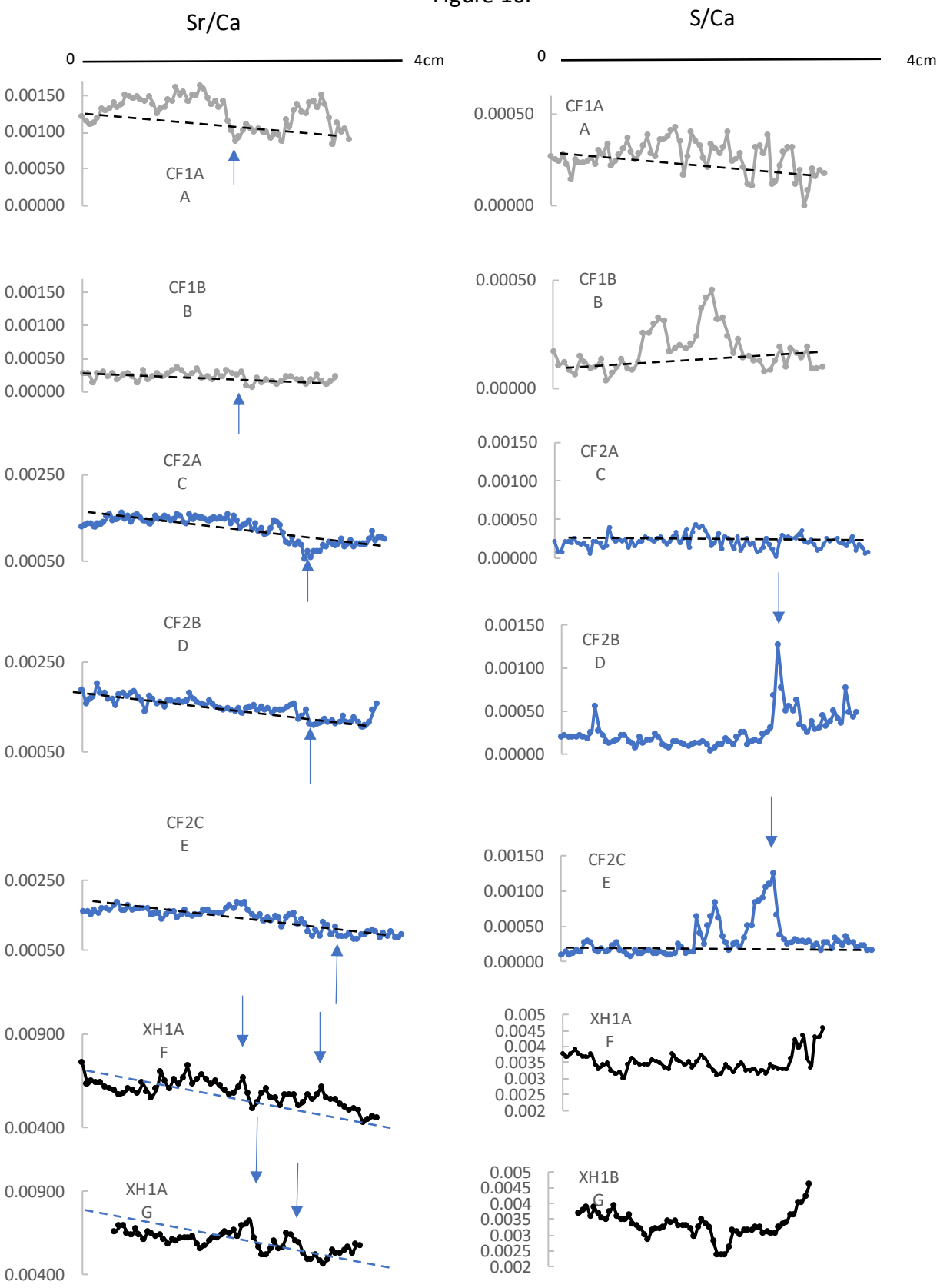
Sr/Ca
S/Ca
0
4cm
CF1A
A
CF1B
B
CF2A
C
CF2B
D
CF2C
E
XH1A
F
XH1A
G
XH1B
G

Figure 17.

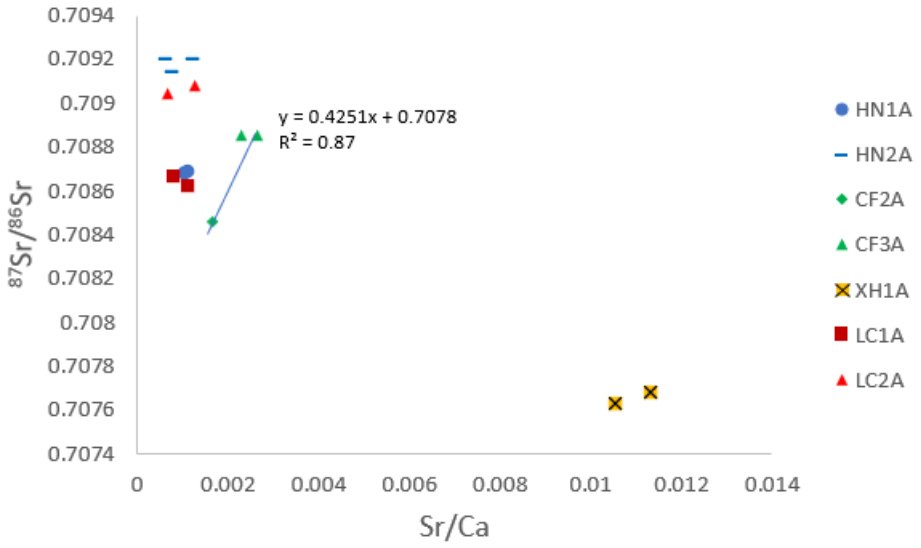
0.7094
0.7092
0.709
0.7088
0.7086
0.7084
0.7082
0.708
0.7078
0.7076
0.7074
$^{87}Sr/^{86}Sr$
y = 0.4251x + 0.7078
R^2 = 0.87
0
0.002
0.004
0.006
0.008
0.01
0.012
0.014
Sr/Ca
HN1A
HN2A
CF2A
CF3A
XH1A
LC1A
LC2A

Figure 18.

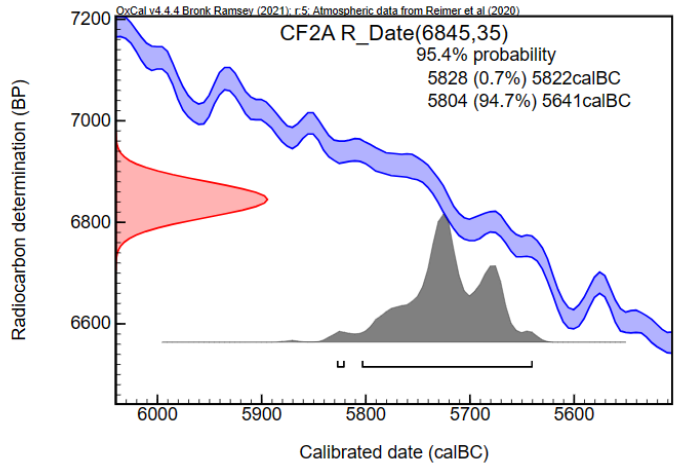
OxCal v4.4.4 Bronk Ramsey (2021); r:5; Atmospheric data from Reimer et al (2020)
CF2A R_Date(6845,35)
95.4% probability
5828 (0.7%) 5822calBC
5804 (94.7%) 5641calBC
Radiocarbon determination (BP)
7200
7000
6800
6600
6000
5900
5800
5700
5600
Calibrated date (calBC)

A

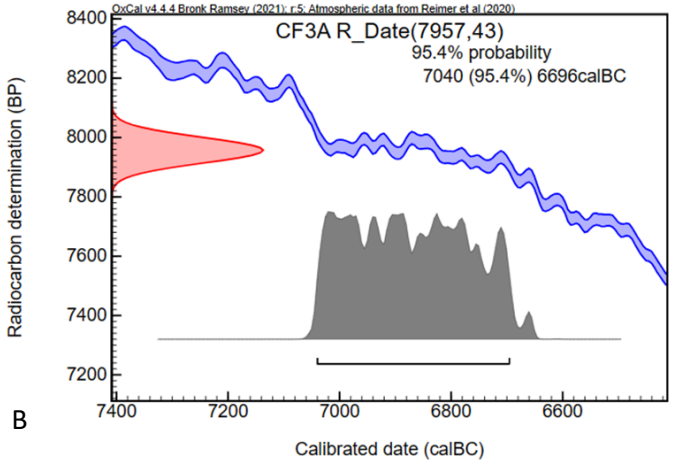
OxCal v4.4.4 Bronk Ramsey (2021); r:5; Atmospheric data from Reimer et al (2020)
CF3A R_Date(7957,43)
95.4% probability
7040 (95.4%) 6696calBC
Radiocarbon determination (BP)
8400
8200
8000
7800
7600
7400
7200
7400
7200
7000
6800
6600
Calibrated date (calBC)

B

Figure 19.

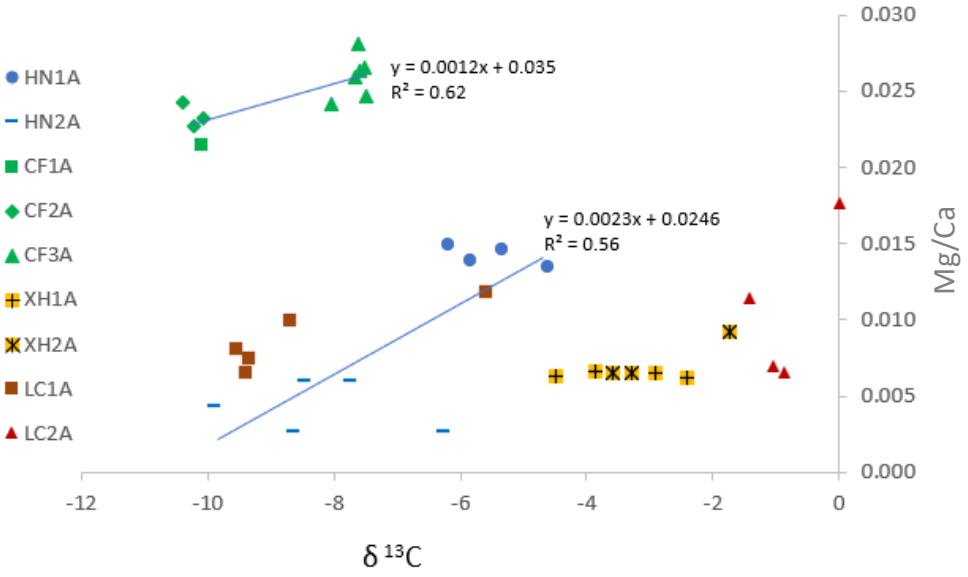

Figure 20.

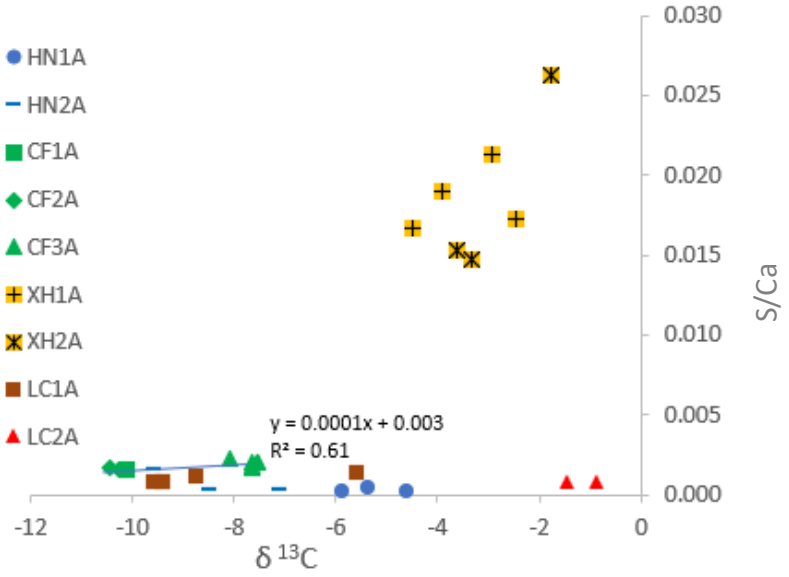

Figure 21.

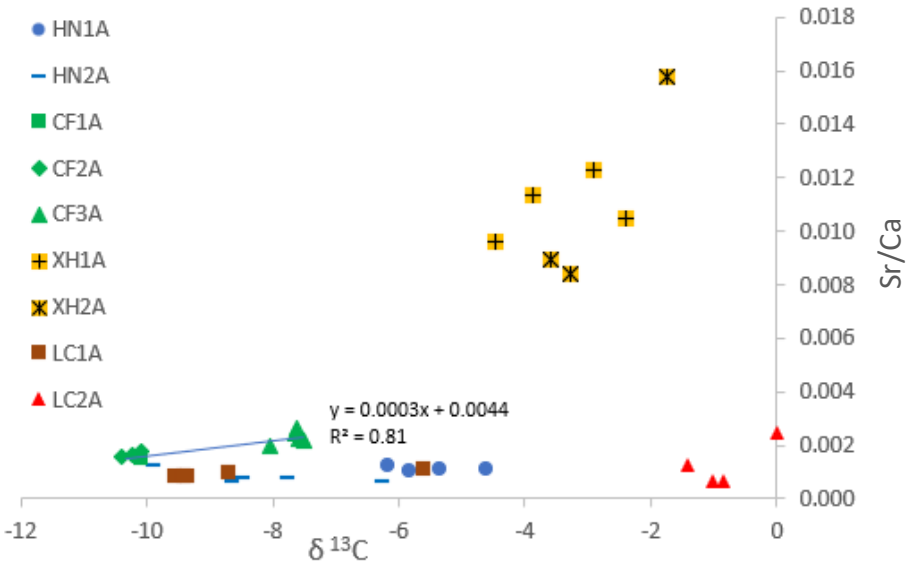

Figure 22.

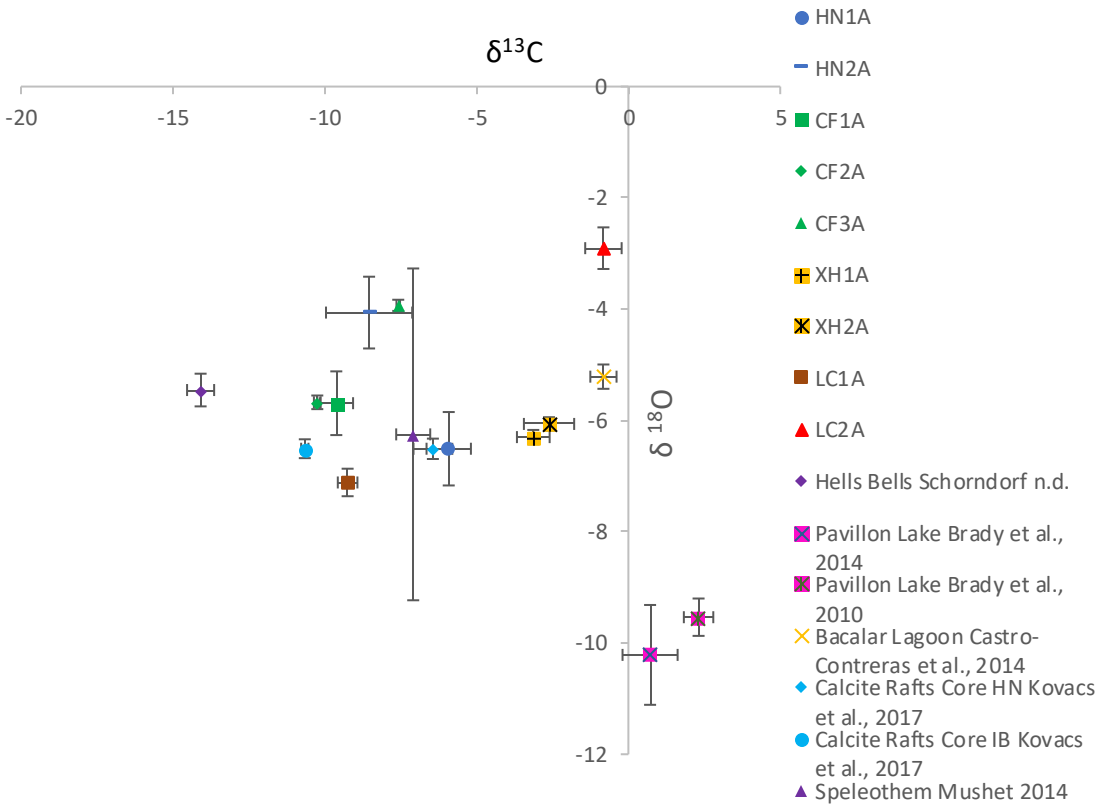

Figure 23.

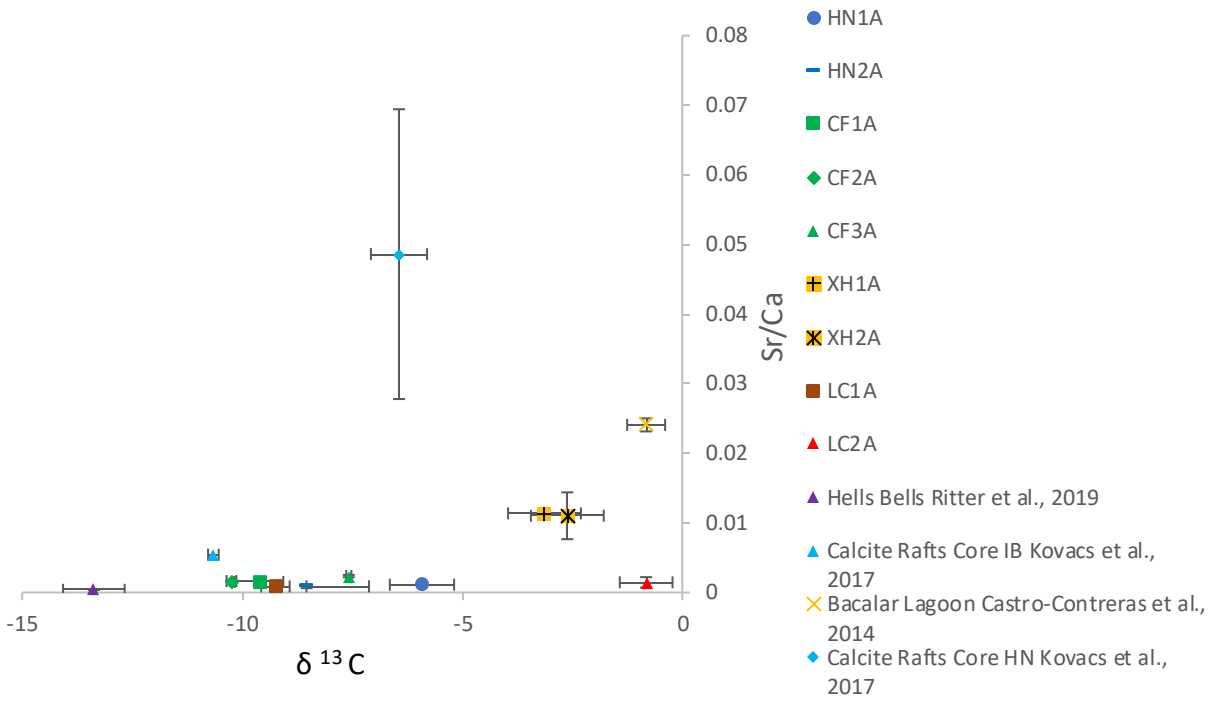
0.08
0.07
0.06
0.05
0.04
0.03
0.02
0.01
0
Sr/Ca
-15
-10
-5
0
δ 13 C
HN1A
HN2A
CF1A
CF2A
CF3A
XH1A
XH2A
LC1A
LC2A
Hells Bells Ritter et al., 2019
Calcite Rafts Core IB Kovacs et al., 2017
Bacalar Lagoon Castro-Contreras et al., 2014
Calcite Rafts Core HN Kovacs et al., 2017

Figure 24.

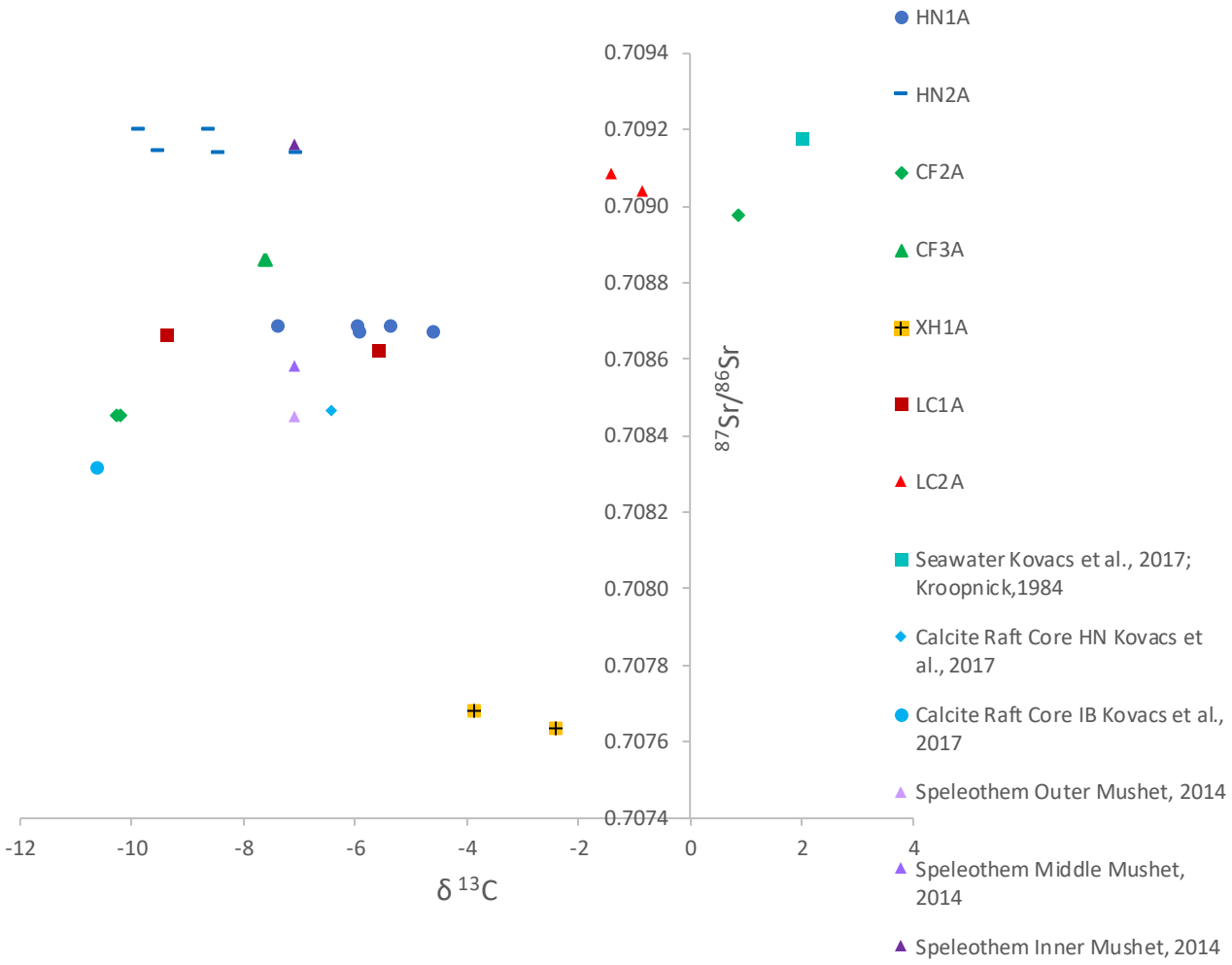
0.7094
0.7092
0.7090
0.7088
0.7086
0.7084
0.7082
0.7080
0.7078
0.7076
0.7074
87Sr/86Sr
-12
-10
-8
-6
-4
-2
0
2
4
δ 13C
HN1A
HN2A
CF2A
CF3A
XH1A
LC1A
LC2A
Seawater Kovacs et al., 2017; Kroopnick,1984
Calcite Raft Core HN Kovacs et al., 2017
Calcite Raft Core IB Kovacs et al., 2017
Speleothem Outer Mushet, 2014
Speleothem Middle Mushet, 2014
Speleothem Inner Mushet, 2014

Figure 25.

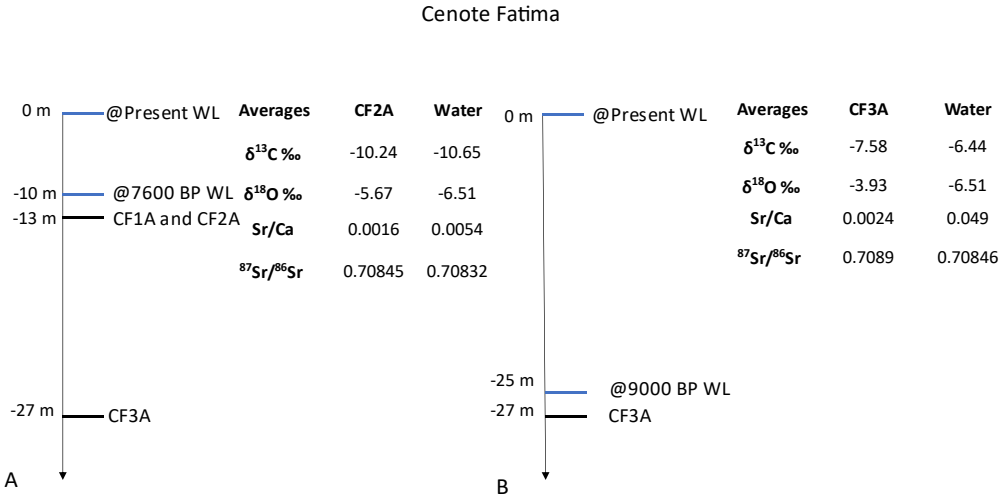

Supplementary Table 1.

Sample	Depth	Description	D-AMS #	^{14}C Age (yBP ±1σ)	Reservoir Corrected	Age Cal yBP (2σ)
Yucatan Peninsula						
HN1A	18m	Outer Growth 0.5cm	052230	NDFB >45,000	-	-
CF2A	13m	Outer Growth 0.5cm	052228	8112 ±35σ	6845 ±35σ	7591
CF3A	27m	Outer Growth 0.5cm	052229	9224 ±43σ	7957 ± 43σ	8990

Site: Xul Ha Cenote
Sample Number: XH1A
Water depth: 21cm
Salinity: 1.15 ppt
Light: Full
Lat: 18.551200°
Long: -88.459840°

Supplementary Figure 1.

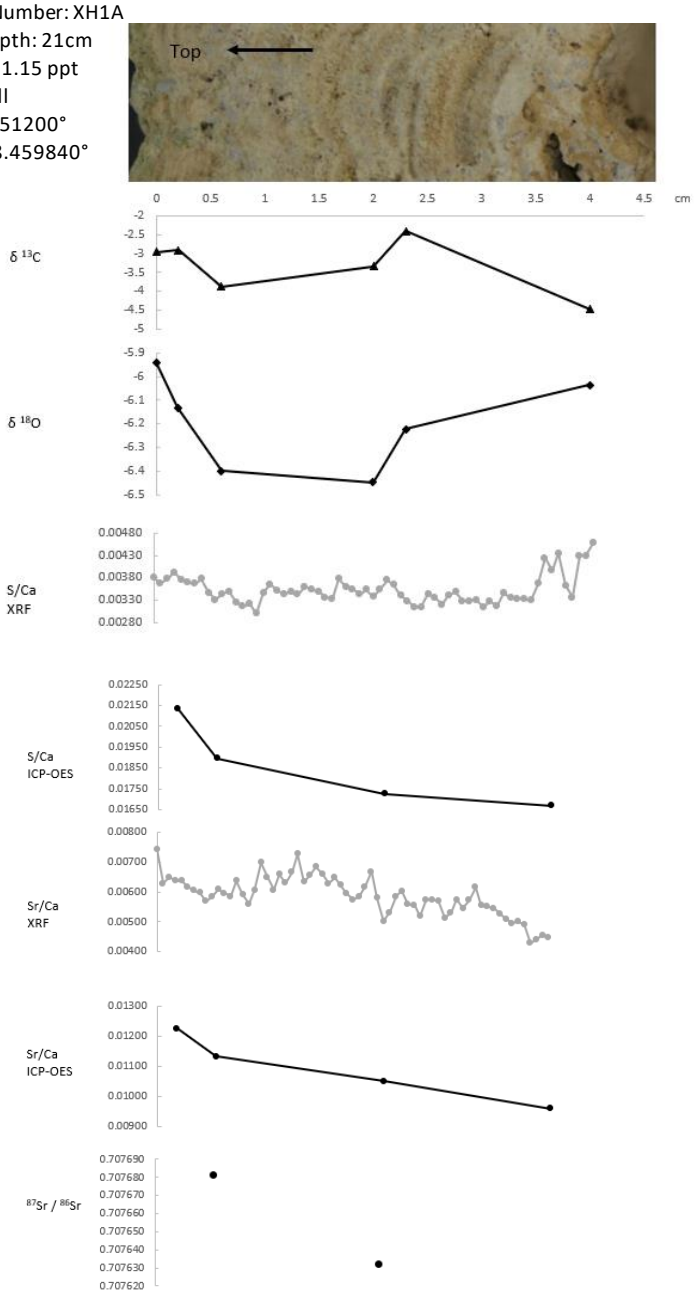

Supplementary Figure 2.

Site: Xul Ha Cenote
Sample Number: XH2A
Water depth: 21cm
Salinity: 1.1-1.2 ppt
Light: Full
Lat: 18.564095°
Long: -88.444150°

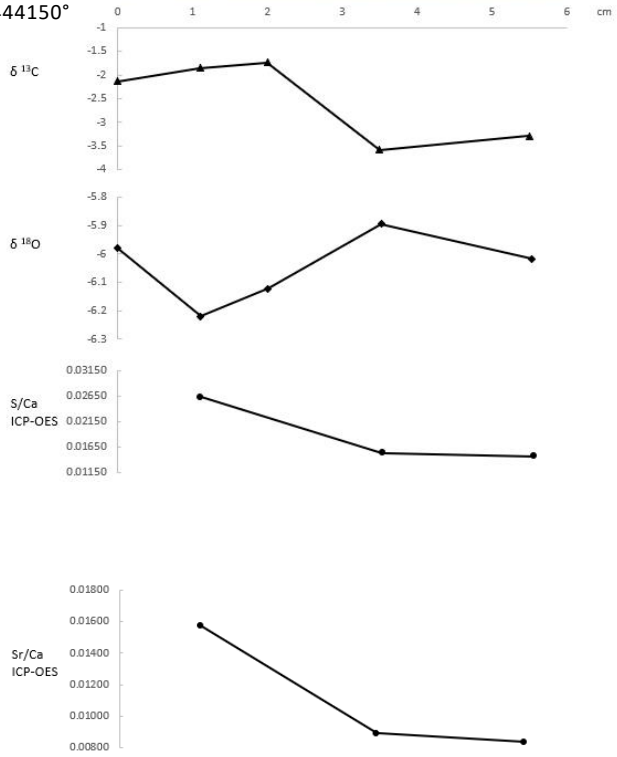

Supplementary Figure 3.

Site: Cenote Fatima
Sample Number: CF1A
Water depth: 13 m
Salinity: 0.7313 psu
Light: Sheltered
Lat: 20.844140°
Long: -87.177712°

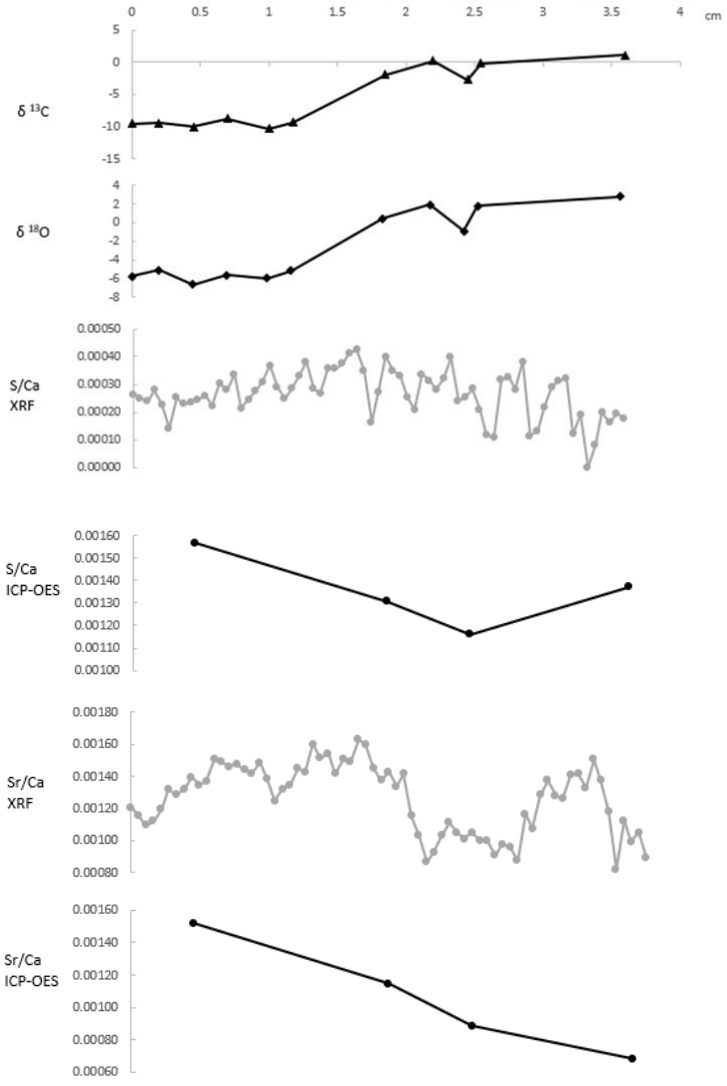

Supplementary Figure 4.

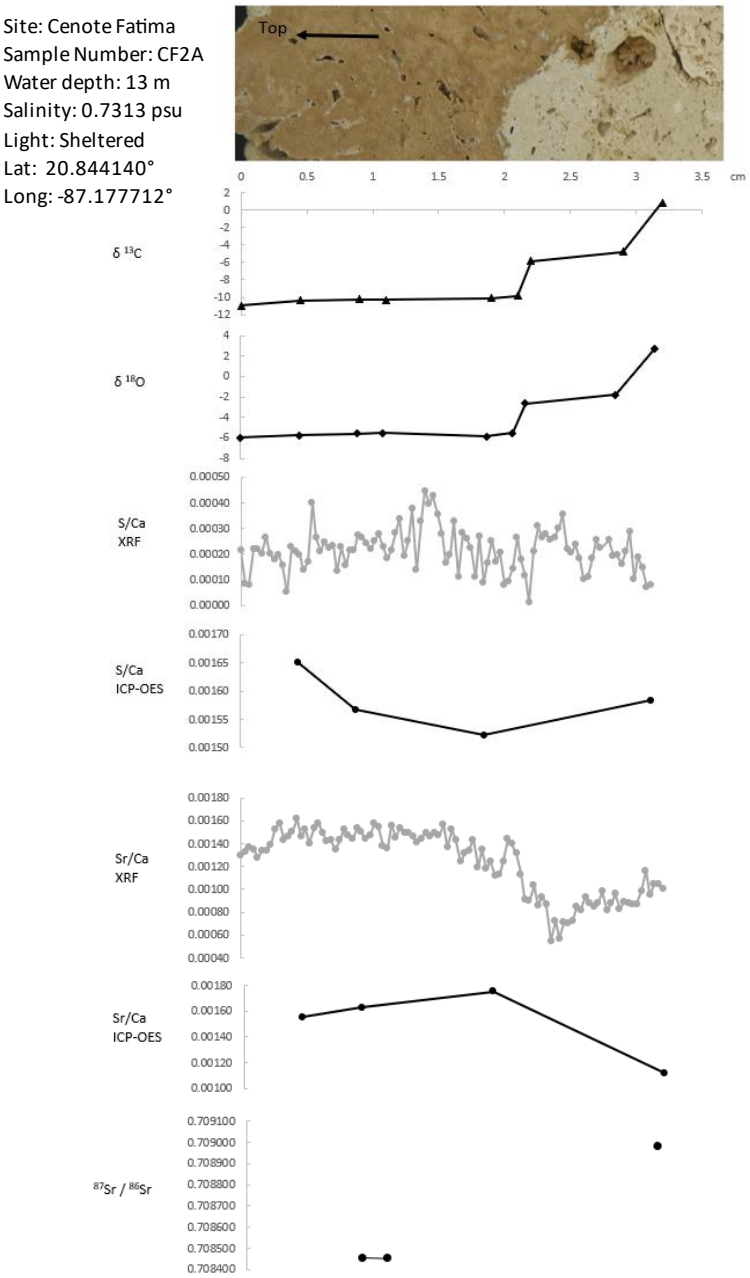

Site: Cenote Fatima
Sample Number: CF3A
Water depth: 27 m
Salinity: 0.81375 psu
Light: Sheltered
Lat: 20.844140°
Long: -87.177712°

Supplementary Figure 5.

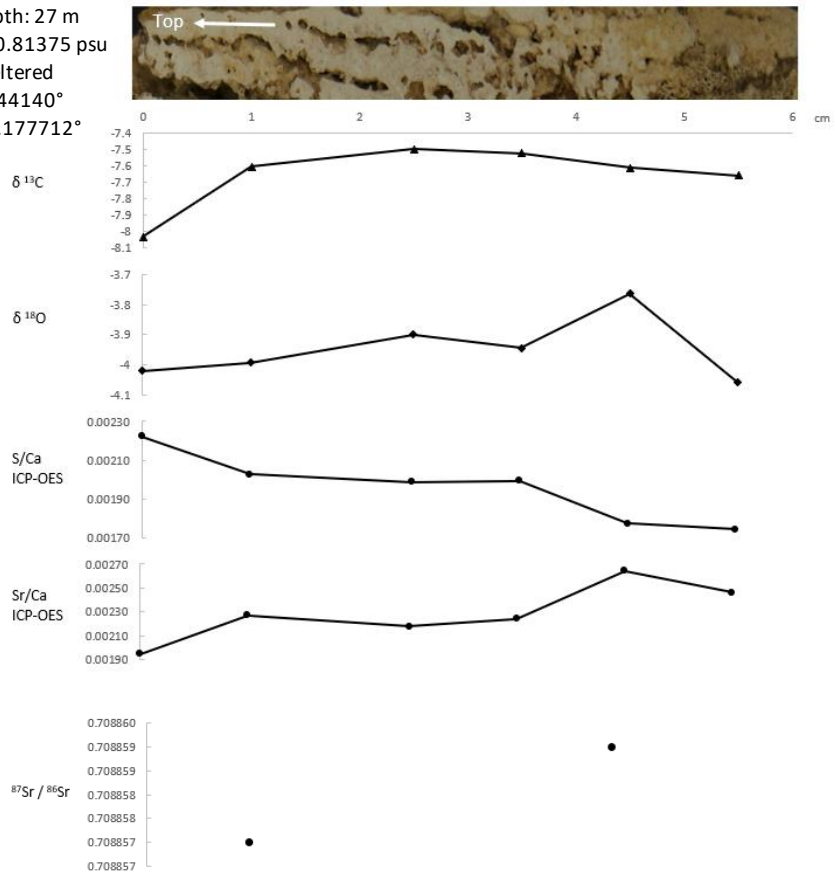

Supplementary Figure 6.

Site: Hoyo Negro
Sample Number: HN1A
Water depth: 18 m
Salinity: 20.18 ppt
Light: None
Lat: 20. 315208° N
Long: -87. 428646° W

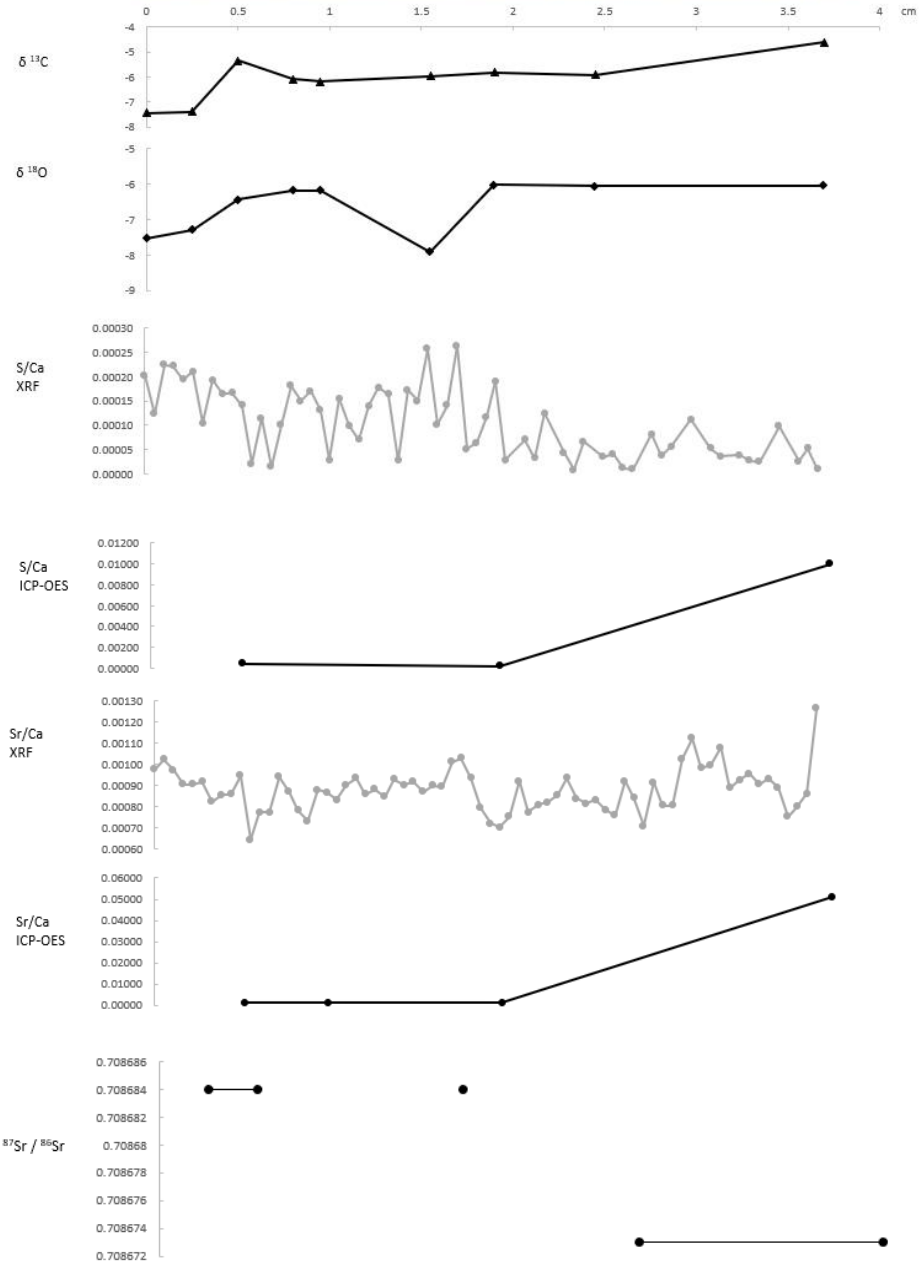

Supplementary Figure 7.

Site: Hoyo Negro
Sample Number: HN2A
Water depth: 45 m
Salinity: 35.124 ppt
Light: None
Lat: 20. 315208° N
Long: -87. 428646° W

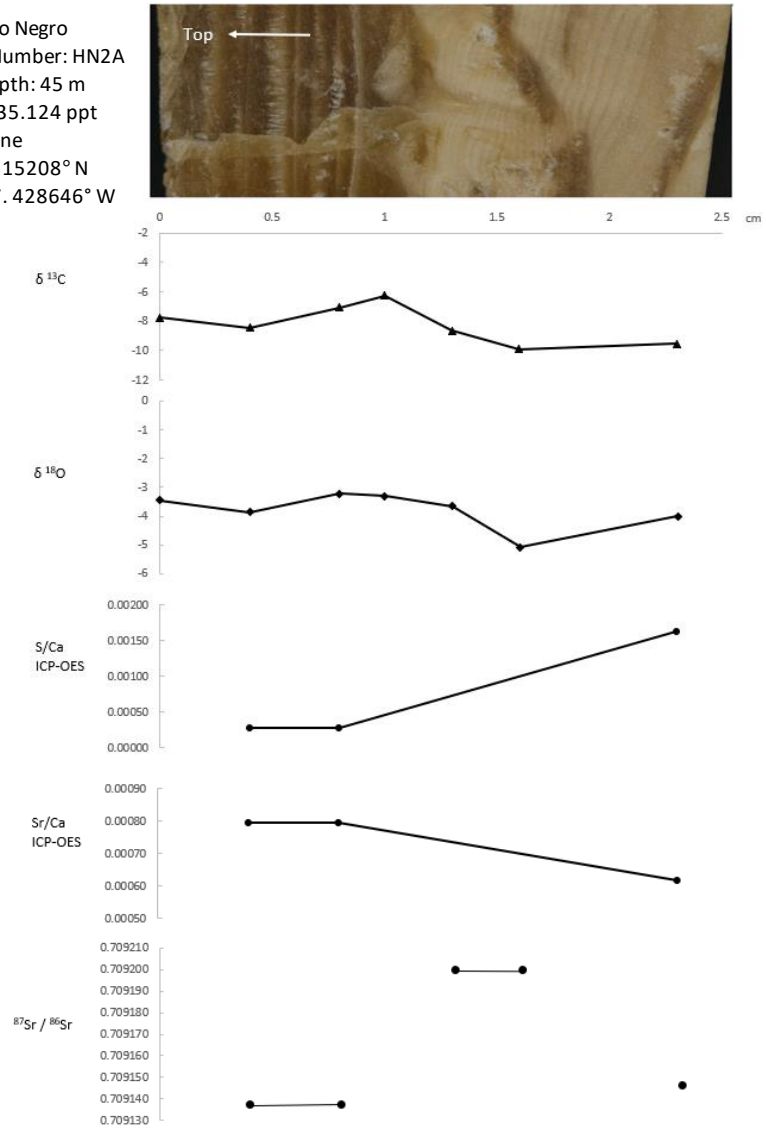

Supplementary Figure 8.

Site: La Concha
Sample Number: LC1A
Water depth:12
Salinity: 35.124 ppt
Light: None
Lat: 20.319939°
Long: -87.426714°

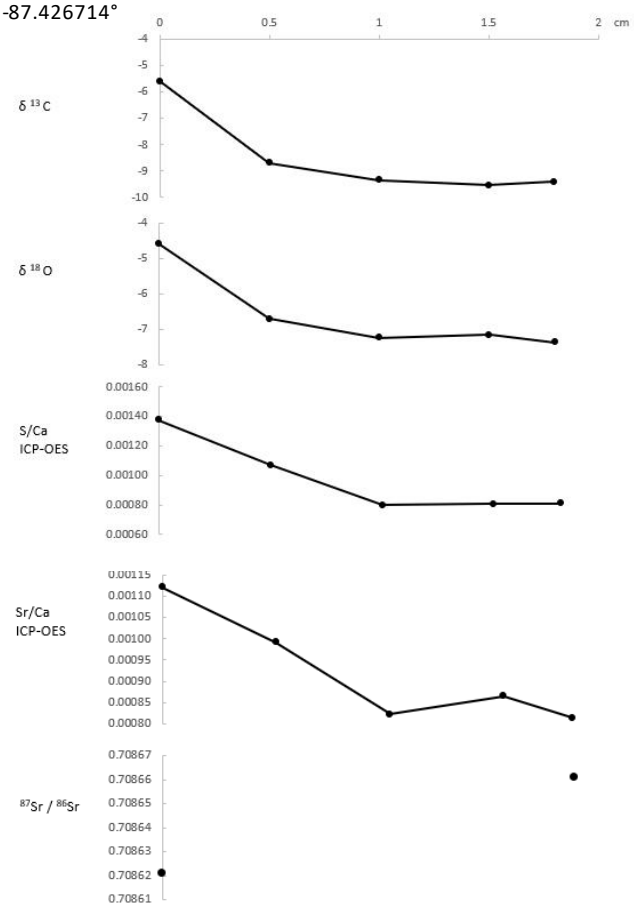

Supplementary Figure 9.

Site: La Concha
Sample Number: LC2A
Water depth:12m
Salinity: 35.124 ppt
Light: None
Lat: 20.319939°
Long: -87.426714°

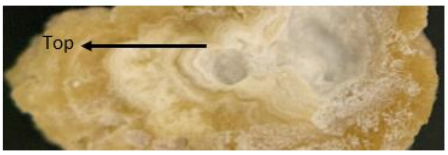

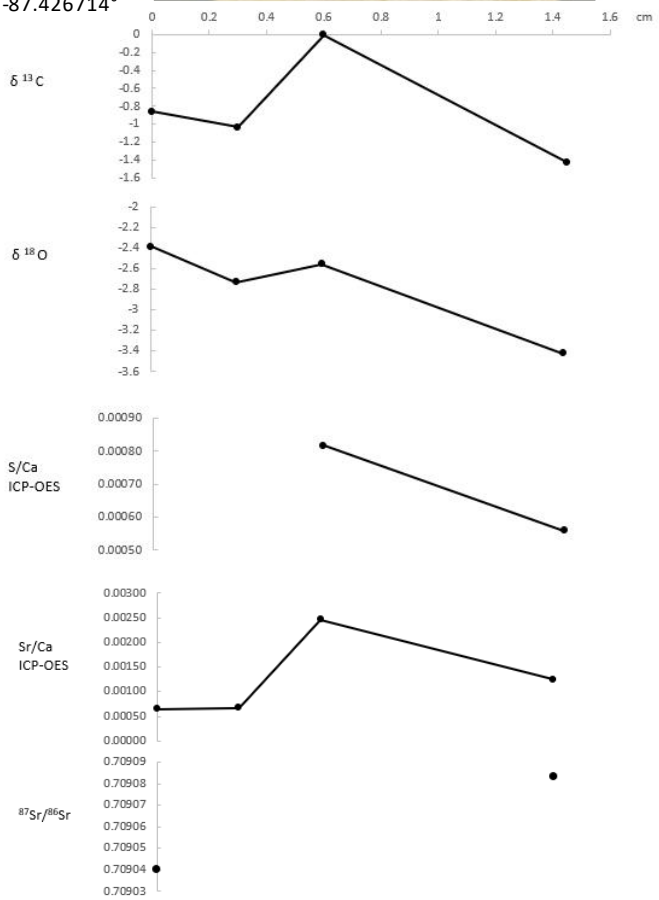

Supplementary Table 2.

Location Sample #	Distance cm	Mid point cm	$\delta^{13}C$ per mil	$\delta^{18}O$ per mil	ICP-OES % Mn	ICP-OES % Al	ICP-OES % Fe	ICP-OES % K	ICP-OES % Mg	ICP-OES % S	ICP-OES % Sr	ICP-OES % Ti	ICP-OES % Ca	XRF Cr Counts Mn	XRF Cr Counts Al	XRF Cr Counts Fe	XRF Cr Counts K	XRF Cr Counts Mg	XRF Cr Counts S	XRF Cr Counts Sr	XRF Cr Counts Ti	XRF Cr Counts Ca	$^{87}Sr/^{86}Sr$	XRD
Hoyo Negro																								
HN 1A 0	0	0	-7.43	-7.54	-	-	-	-	-	-	-	-	-	-	-	-	-	-	-	-	-	-	-	-
HN 1A 1	0.2-0.3	0.25	-7.38	-7.28	-	-	-	-	-	-	-	-	-	-	-	-	-	-	-	-	-	-	0.70868	
HN 1A 2	0.4-0.6	0.5	-5.35	-6.43	< 0.0005	0.01	< 0.01	0.02	0.65	0.02	0.0504	< 0.01	44.4	337	178	70	0	0	139	674	0	709778	0.70868	Calcite
HN 1A 5	0.8	0.8	-6.09	-6.17	-	-	-	-	-	-	-	-	-	556	155	93	0	0	110	611	0	701943	-	-
HN 1A 6	0.9-1.0	0.95	-6.18	-6.17	< 0.0005	< 0.01	< 0.01	0.01	0.66	< 0.01	0.0537	< 0.01	44.3	460	173	108	0	0	50	533	0	682861	-	-
HN 1A 8	1.45-1.65	1.55	-5.97	-7.92	-	-	-	-	-	-	-	-	-	646	166	86	0	0	93	646	41	729531	0.70868	
HN 1A 10	1.8-2	1.9	-5.83	-6.01	< 0.0005	< 0.01	< 0.01	0.02	0.67	0.01	0.0498	< 0.01	48.1	718	143	44	0	0	105	544	0	692464	-	Calcite
HN 1A 12	2.1-2.8	2.45	-5.92	-6.06	-	-	-	-	-	-	-	-	-	1003	167	105	0	0	39	600	0	737070	0.70867	-
HN 1A 15	3.6-3.8	3.7	-4.61	-6.04	< 0.0005	< 0.01	< 0.01	0.02	0.63	0.01	0.0509	< 0.01	46.9	-	-	-	-	-	-	-	-	-	0.70867	-
HN2A 0	0	-	-7.75	-3.45	-	-	-	-	-	-	-	-	-	-	-	-	-	-	-	-	-	-	-	-
HN2A 1	0.4	-	-8.46	-3.86	< 0.0005	< 0.01	< 0.01	< 0.01	0.22	0.01	0.0291	< 0.01	36.6	-	-	-	-	-	-	-	-	-	0.70914	Calcite
HN2A 2	0.8	-	-7.08	-3.23	< 0.0005	< 0.01	< 0.01	< 0.01	0.22	0.01	0.0291	< 0.01	36.6	-	-	-	-	-	-	-	-	-	0.70914	Calcite
HN2A 3	1	-	-6.26	-3.31	-	-	-	-	-	-	-	-	-	-	-	-	-	-	-	-	-	-	-	-
HN2A 4	1.3	-	-8.64	-3.65	< 0.0005	< 0.01	< 0.01	< 0.01	0.1	< 0.01	0.023	< 0.01	37.3	-	-	-	-	-	-	-	-	-	0.70920	Calcite
HN2A 5	1.6	-	-9.90	-5.08	< 0.0005	< 0.01	< 0.01	< 0.01	0.1	< 0.01	0.023	< 0.01	37.3	-	-	-	-	-	-	-	-	-	0.70920	Calcite
HN2A 6	2.3	-	-9.53	-4.00	< 0.0005	< 0.01	< 0.01	< 0.01	0.08	0.03	0.0227	< 0.01	18.5	-	-	-	-	-	-	-	-	-	0.70915	Calcite
Cenote Fatima																								
CF 1A 0	0	0	-9.63	-5.73	-	-	-	-	-	-	-	-	-	-	-	-	-	-	-	-	-	-	-	-
CF 1A 0.2	0.2	0.2	-9.51	-5.09	-	-	-	-	-	-	-	-	-	-	-	-	-	-	-	-	-	-	-	-
CF 1A 0.3	0.4-0.5	0.45	-10.09	-6.63	< 0.0005	0.01	< 0.01	0.02	0.96	0.07	0.0679	< 0.01	44.7	678	160	64	0	0	197	878	0	767174	-	-
CF 1A 0.6	0.6-0.8	0.7	-8.79	-5.61	-	-	-	-	-	-	-	-	-	762	183	160	0	0	168	1013	0	778103	-	Calcite
CF 1A 0.9	0.9-1.1	1	-10.34	-5.98	-	-	-	-	-	-	-	-	-	590	174	104	0	0	213	1115	0	764464	-	-
CF 1A 1.3	1.1-1.45	1.175	-9.35	-5.14	-	-	-	-	-	-	-	-	-	522	177	104	0	0	212	1035	0	744861	-	Calcite
CF 1A 1.5	1.7-2.0	1.85	-1.96	0.43	0	0.02	< 0.01	0.02	6.14	0.05	0.0439	< 0.01	38.3	610	182	189	0	7	271	1140	0	745830	-	-
CF 1A 1.9	2.1-2.3	2.2	0.15	1.93	-	-	-	-	-	-	-	-	-	405	149	247	0	27	178	711	0	555775	-	-
CF 1A 2.1	2.4-2.5	2.45	-2.75	-0.92	0.0082	0.03	0.01	0.02	8.28	0.04	0.0305	< 0.01	34.5	507	149	115	0	55	179	594	0	579702	-	-
CF 1A 2.5	2.5-2.6	2.55	-0.24	1.79	-	-	-	-	-	-	-	-	-	632	142	123	0	41	203	643	0	608530	-	Calcite/Dolomite
CF 1A 3.0	3.4-3.8	3.6	1.11	2.75	0.0074	< 0.01	0.01	< 0.01	10.2	0.04	0.0199	< 0.01	29.2	584	124	110	0	55	79	526	0	464314	-	Calcite/Dolomite
CF 2A 0	0	0	-10.94	-5.99	-	-	-	-	-	-	-	-	-	-	-	-	-	-	-	-	-	-	-	-
CF 2A 0.5	0.4-0.5	0.45	-10.39	-5.72	0.0007	0.01	< 0.01	0.01	1.03	0.07	0.0659	< 0.01	42.4	772	175	64	0	0	116	1039	0	777088	-	Calcite
CF 2A 0.9	0.9	0.9	-10.22	-5.57	0.0006	< 0.01	< 0.01	0.01	0.87	0.06	0.0624	< 0.01	38.3	232	166	49	0	0	125	874	0	571501	0.70845	Calcite
Cf 2A 1.1	1.1	1.1	-10.28	-5.55	-	-	-	-	-	-	-	-	-	611	159	56	0	0	129	1137	0	759093	0.70845	-
CF 2A 1.5	1.8-2.0	1.9	-10.08	-5.85	0.0007	< 0.01	< 0.01	0.01	1.07	0.07	0.0806	< 0.01	46	572	183	50	0	0	196	1143	0	768784	-	-
CF 2A 1.8	2.1	2.1	-9.83	-5.53	-	-	-	-	-	-	-	-	-	547	173	40	0	0	181	1127	0	769388	-	-
CF 2A 1.9	2.2	2.2	-5.86	-2.63	-	-	-	-	-	-	-	-	-	627	174	71	0	0	175	1135	0	766752	-	-
CF 2A 2.1	2.8-3.0	2.9	-4.80	-1.81	-	-	-	-	-	-	-	-	-	440	140	91	0	33	130	773	0	564644	-	Calcite/Dolomite
CF 2A 2.3	3.1-3.3	3.2	0.87	2.73	0.0043	0.02	< 0.01	0.01	6.51	0.06	0.0425	< 0.01	37.9	499	144	126	0	68	103	686	0	535821	0.70898	Calcite/Dolomite
CF3A 0	0	-	-8.03	-4.02	0.0075	0.05	0.13	< 0.01	0.87	0.08	0.07	< 0.01	36	-	-	-	-	-	-	-	-	-	-	-
CF3A 1	1	-	-7.60	-3.99	0.0334	0.1	0.13	< 0.01	0.91	0.07	0.0784	< 0.01	34.5	-	-	-	-	-	-	-	-	-	0.70886	Calcite
CF3A 2	2.5	-	-7.50	-3.90	0.0226	0.09	0.12	< 0.01	0.87	0.07	0.0766	< 0.01	35.2	-	-	-	-	-	-	-	-	-	-	-
CF3A 3	3.5	-	-7.52	-3.94	0.019	0.12	0.14	< 0.01	0.93	0.07	0.0786	< 0.01	35.1	-	-	-	-	-	-	-	-	-	-	Calcite
CF3A 4	4.5	-	-7.61	-3.76	0.0154	0.05	0.08	< 0.02	0.95	0.06	0.0893	< 0.02	33.8	-	-	-	-	-	-	-	-	-	0.70886	-
CF3A 5	5.5	-	-7.66	-4.06	0.0223	0.04	0.11	< 0.01	0.89	0.06	0.0847	< 0.01	34.4	-	-	-	-	-	-	-	-	-	-	Calcite
Xul Ha																								
XH 1A 0	0	-	-2.96	-5.94	-	-	-	-	-	-	-	-	-	-	-	-	-	-	-	-	-	-	-	-
XH 1A 0.3	0.2	-	-2.91	-6.13	< 0.0005	0.03	0.01	0.02	0.35	1.15	0.661	< 0.01	53.9	586	174	110	227	0	2425	4240	0	639462	-	-
XH 1A 0.7	0.6	-	-3.87	-6.40	< 0.0005	0.02	< 0.01	0.02	0.35	1	0.597	< 0.01	52.7	409	146	93	0	0	2156	3640	0	616972	0.70768	Calcite
XH 1A 1.1	2	-	-3.34	-6.45	-	-	-	-	-	-	-	-	-	542	177	83	0	5	2391	4087	0	675166	-	-
XH 1A 1.7	2.3	-	-2.41	-6.22	< 0.0005	0.02	< 0.01	0.02	0.36	1.01	0.615	< 0.01	58.5	480	162	105	0	1	2109	3598	0	638813	0.70763	Calcite
XH 1A 2.0	4	-	-4.48	-6.04	0.001	0.03	0.02	0.02	0.37	0.98	0.563	< 0.01	58.7	484	185	77	0	3	2790	2849	0	630295	-	-
XH 2A 0	0	-	-2.12	-5.98	-	-	-	-	-	-	-	-	-	-	-	-	-	-	-	-	-	-	-	-
XH 2A 3	1.1	-	-1.85	-6.22	< 0.0005	0.03	0.01	0.01	0.34	0.97	0.582	< 0.01	36.9	-	-	-	-	-	-	-	-	-	-	Calcite
XH 2A 5	2	-	-1.73	-6.12	-	-	-	-	-	-	-	-	-	-	-	-	-	-	-	-	-	-	-	-
XH 2A 7	3.5	-	-3.58	-5.89	0.0007	0.02	0.03	0.01	0.34	0.8	0.467	< 0.01	52.3	-	-	-	-	-	-	-	-	-	-	Calcite
XH 2A 10	5.5	-	-3.29	-6.02	0.0007	0.02	0.01	0.01	0.34	0.77	0.438	< 0.01	52.3	-	-	-	-	-	-	-	-	-	-	-
La Concha																								
LC1A 0	0	-	-5.60	-4.59	0.0019	0.04	0.04	< 0.01	0.43	0.05	0.0407	< 0.01	36.3	-	-	-	-	-	-	-	-	-	0.708621	Calcite
LC1A 1	0.5	-	-8.70	-6.71	0.0011	0.01	0.01	< 0.01	0.37	0.04	0.037	< 0.01	37.3	-	-	-	-	-	-	-	-	-	-	-
LC1A 2	1.0	-	-9.34	-7.24	0.0009	0.01	0.01	< 0.01	0.28	0.03	0.0309	< 0.01	37.6	-	-	-	-	-	-	-	-	-	-	-
LC1A 3	1.5	-	-9.54	-7.16	0.0017	0.02	0.02	< 0.01	0.3	0.03	0.0322	< 0.01	37.2	-	-	-	-	-	-	-	-	-	-	-
LC1A 4	1.8	-	-9.40	-7.36	0.0006	0.01	< 0.01	< 0.01	0.24	0.03	0.0301	< 0.01	37	-	-	-	-	-	-	-	-	-	0.708661	Calcite
LC2A 0	0	0	-0.86	-2.39	< 0.00005	< 0.01	< 0.01	< 0.01	0.24	< 0.01	0.0236	< 0.01	36.7	-	-	-	-	-	-	-	-	-	0.70904	-
LC2A 1	0-0.5	0.3	-1.03	-2.73	< 0.00005	< 0.01	< 0.01	< 0.01	0.26	< 0.01	0.0249	< 0.01	37.1	-	-	-	-	-	-	-	-	-	-	Calcite
LC2A 2	0.5-0.7	0.6	-0.01	-2.56	< 0.00010	0.02	0.03	< 0.02	0.65	0.03	0.0902	< 0.02	36.7	-	-	-	-	-	-	-	-	-	-	-
LC2A 3	1.2-1.8	1.45	-1.43	-3.42	< 0.00005	0.02	0.02	< 0.01	0.41	0.02	0.0449	< 0.01	35.8	-	-	-	-	-	-	-	-	-	0.709083	Calcite

Supplementary Figure 10.

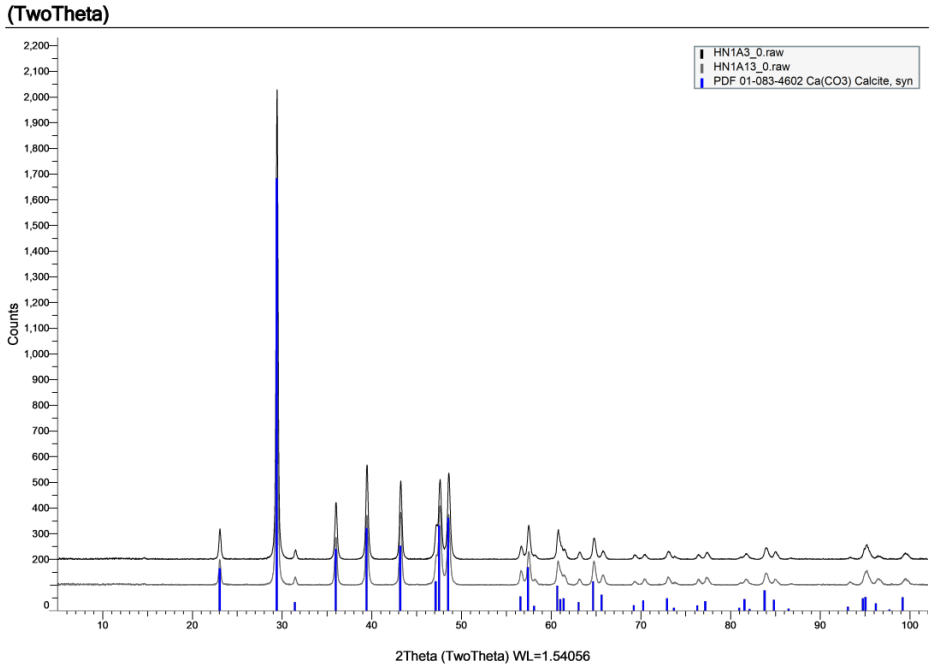

Supplementary Figure 11.

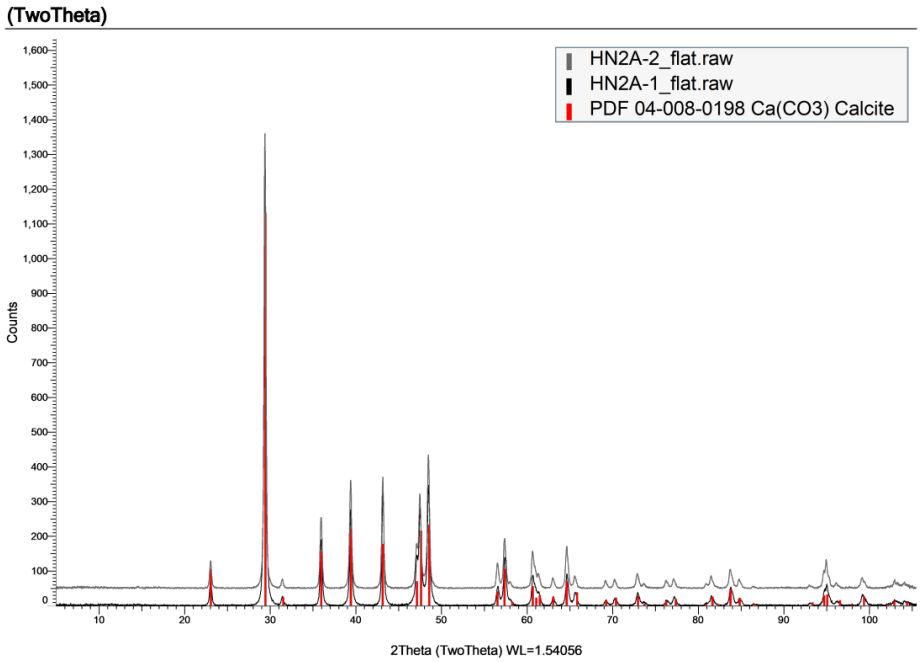

Supplementary Figure 12.

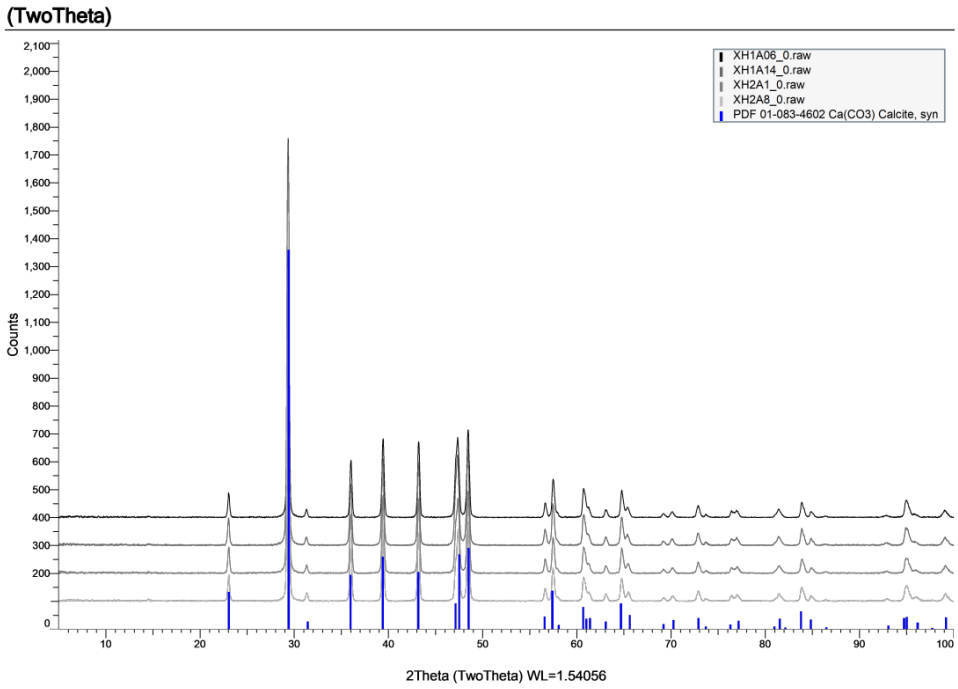

Supplementary Figure 13.

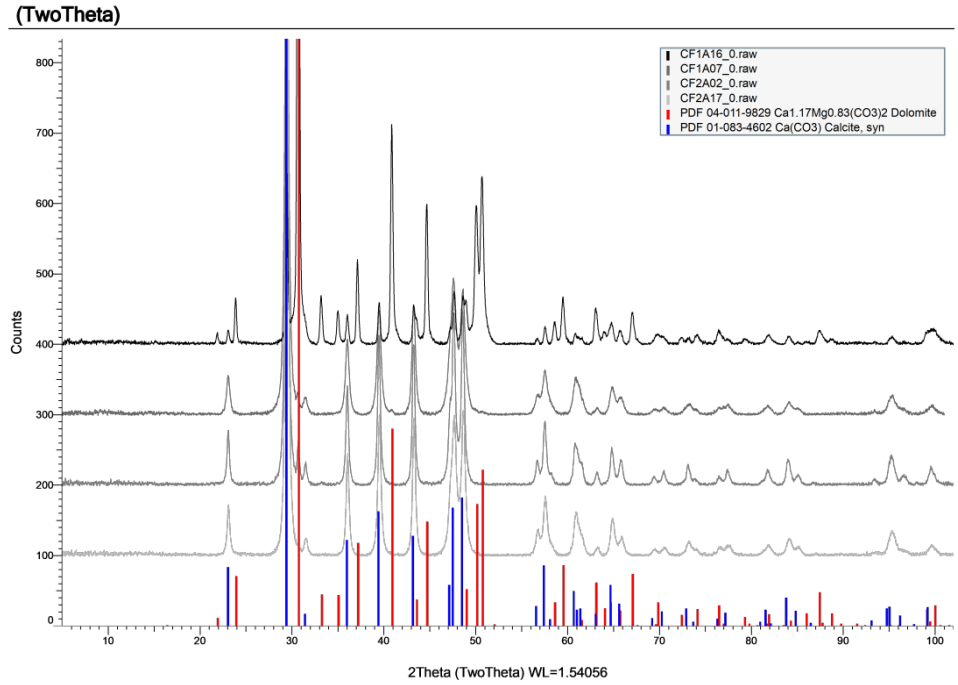

Supplementary Figure 14.

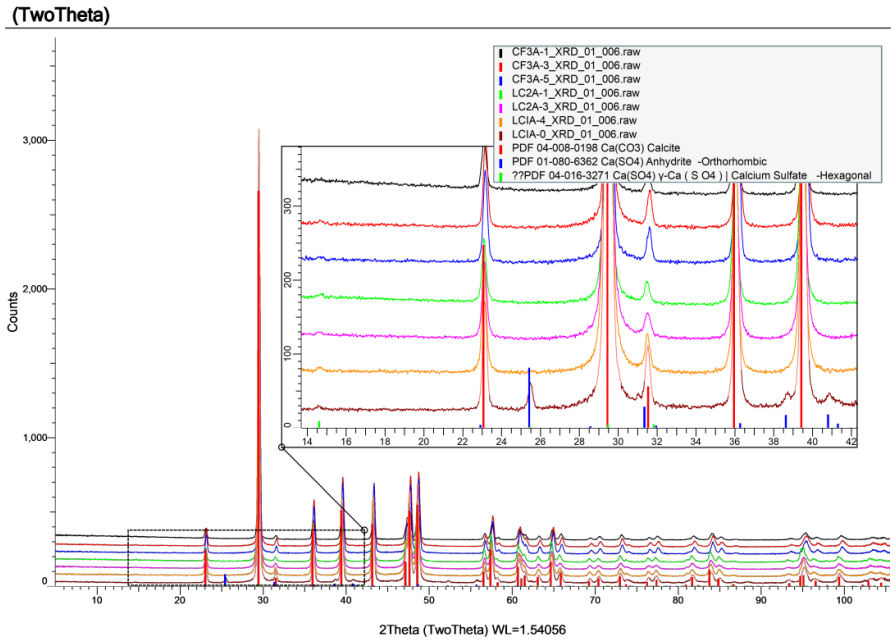

Supplementary Table 3.

Samples	Depth (m)	$\delta^{18}O_{water}$ vs. SMOW
C Fatima 1	0	-4.1
C Fatima 2	5	-4.29
C Fatima 3	10	-4.62
C Fatima 4	15	-4.58
C Fatima 5	20	-4.54
C Fatima 6	25	-4.1
C Fatima 7	30	-4.55